

ALMA MATER STUDIORUM · UNIVERSITÀ DI BOLOGNA

SCUOLA DI SCIENZE

Dipartimento di Chimica Industriale “Toso Montanari”

Corso di Laurea Magistrale in

Chimica Industriale

Classe LM-71 - Scienze e Tecnologie della Chimica Industriale

**Development and Optimization of Fibre-Shaped
Dye-Sensitized Solar Cells employing an
Innovative Fully Organic Sensitizer**

Tesi di laurea sperimentale

CANDIDATO

Simone Casadio

RELATORE

Chiar.ma Prof.ssa Cristina Femoni

CORRELATORE

Dr. Alessandra Sanson

Dr. Nicola Sangiorgi

Anno Accademico 2018-2019

Some things stay the Same
Only by Changing

Table of Contents

<i>Abstract</i>	<i>viii</i>
<i>List of symbols and abbreviations</i>	<i>xi</i>
Chapter 1: Introduction	
1.1. Energy demand and energy consumption.....	1
1.2. Renewable energy.....	2
1.2.1. Solar Energy	5
<i>References</i>	7
Chapter 2: Photovoltaic Solar Cells	
2.1. Solar Radiation	9
2.2. Photovoltaic Technologies.....	11
2.2.1. Solar Cells Terminologies	14
2.2.1.1. Open-Circuit Voltage	14
2.2.1.2. Short-Circuit Current.....	14
2.2.1.3. Fill Factor	15
2.2.1.4. Power Conversion Efficiency.....	15
2.2.2. Photovoltaic Generations.....	15
2.2.2.1. First-generation PVCs	15
2.2.2.2. Second-generation PVCs.....	16
2.2.2.3. The Shockley-Queisser limit	17
2.2.2.4. Third-generation PVCs.....	18
<i>References</i>	21

Chapter 3: Dye-Sensitized Solar Cells

3.1. Introduction do Dye Sensitized Solar Cells	23
3.2. Structure and Operating Principle	24
3.3. Components.....	28
3.3.1. Nanostructured Metal Oxides Electrodes.....	29
3.3.1.1. TiO ₂	30
3.3.1.2. ZnO	31
3.3.1.2. SnO ₂	32
3.3.2. Dyes.....	32
3.3.2.1. Metal Complexes	33
3.3.2.2. Organic Dyes	34
3.3.2.2. Anchoring of the dye on the oxide surface	36
3.3.3. Electrolytes.....	37
3.3.3.1. Liquid redox electrolytes	38
3.3.2.2. Quasi-solid electrolytes.....	39
3.3.3. Counter Electrode.....	49
<i>References</i>	41

Chapter 4: Fibre-Shaped Dye-Sensitized Solar Cells

4.1. Introduction to Fibre-Shaped Dye Sensitized Solar Cells.....	44
4.2. FDSSC structures	45
4.2.1. Twisting structured FDSSCs.....	45
4.2.2. Coaxial structured FDSSCs.....	47
4.2.3. Parallel structured FDSSCs.....	48
4.3. FDSSCs performances	49
4.4. Properties deriving from fibre shape	50
4.5. Substrates for FDSSCs	51

4.5.1. Metal fibres.....	51
4.5.2. Carbon-based fibres.....	52
4.5.3. Polymer fibres.....	52
4.5.4. Optical fibres	52
<i>References</i>	54

Chapter 5: Experimental Section

5.1. Introduction.....	56
5.2. Photoanodes.....	56
5.2.1. Titanium-based Photoanodes.....	56
5.2.1.1. Cleaning process of Ti-wire substrates	56
5.2.1.2. TiO ₂ blocking layer	57
5.2.1.3. Deposition of the TiO ₂ absorption layer by dip-coating	58
5.2.1.4. Deposition of the pure TiO ₂ ultrathin overcoating	59
5.2.1.4.1. Preparation of the TiCl ₄ solution	59
5.2.1.4.2. TiCl ₄ treatment.....	60
5.2.2. Kevlar-PPy coated-based photoanodes	60
5.3. Sensitization of photoanodes	60
5.4. Electrolytes	61
5.5.1. Liquid electrolytes	61
5.5.2. Gel-state electrolytes	61
5.5. Counter electrodes	62
5.5.1. Pt counter electrodes.....	62
5.5.2. Kevlar-PPy coated-based counter electrodes	62
5.6. Cells assembly	62
5.7. Components Characterization.....	63
5.7.1. Titanium-wire based photoanodes characterization	63

5.7.1.1. Mass determination of TiO ₂ coating	63
5.7.1.2. Thickness determination of TiO ₂ coating	63
5.7.1.3. Electrochemical characterization of TiO ₂ coating	64
5.7.1.4. Spectrophotometric determination of the amount of adsorbed dye ...	64
5.7.1.4.1. Calibration Curves	65
5.7.1.4.2. Extraction of the adsorbed dyes	65
5.7.2. Kevlar-PPy coated-based photoanodes characterization	66
5.7.3. Optical characterization of electrolytes	66
5.7.4. Kevlar-PPy coated-based counter electrodes characterization	66
5.8. FDSSCs characterization	67
5.9. Characterization techniques	67
5.9.1. Scanning Electron Microscopy	67
5.9.2. Cyclic Voltammetry	68
5.9.3. UV-Visible spectroscopy	70
5.9.4. Current-Voltage measurements	70
5.9.5. Electrochemical Impedance Spectroscopy	72
<i>References</i>	75

Chapter 6: Results and Discussions

6.1. Physicochemical characterization of TiO ₂ photoanodes	77
6.1.1. Semiconductor mass and thickness	77
6.1.2. Electrochemical characterization	80
6.2. Comparison between commercially available Ru-based dyes and thiazolo[5,4-d] thiazole-based organic sensitizers	82
6.2.1. Spectrophotometric determination of the amount of adsorbed dye on TiO ₂ surface	83
6.2.1.1. Calibration curves	84
6.2.1.2. Amount of loaded dye	85

6.2.2. Photovoltaic Performances	86
6.3. Influence of TiO ₂ thickness on the photovoltaic performances of TTZ5 – based fibre DSSCs.....	88
6.4. Influence of the electrolyte on the photovoltaic performances of TTZ5 – based fibre DSSCs.....	99
6.4.1. Comparison between I ⁻ /I ₃ ⁻ and [Co(bpy) ₃] ^{3+/2+} – based electrolytes	99
6.4.2. Quasi-solid TTZ5/(I ⁻ /I ₃ ⁻) – based fibre DSSCs.....	102
6.5. Long fibre DSSCs.....	105
6.5.1. Liquid TTZ5/(I ⁻ /I ₃ ⁻) – based long fibre DSSCs	105
6.5.2. Quasi-solid TTZ5/(I ⁻ /I ₃ ⁻) – based long fibre DSSCs	107
6.6. Towards metal free fibre DSSCs	109
6.6.1. Pt free TTZ5-based fibre DSSCs	109
6.6.1.1. Electrochemical characterization	111
6.6.1.2. Short length Pt-free fibre DSSCs	112
6.6.1.3. Liquid (I ⁻ /I ₃ ⁻)-EL-HPE electrolyte.....	113
6.6.1.4. Gel (I ⁻ /I ₃ ⁻) EL-HPE electrolyte	116
6.6.1.5. Long Pt-free fibre DSSCs.....	117
6.6.2. Metal free-based photoanodes	120
<i>References</i>	123
Chapter 7: Conclusion	127

Abstract

The quality of human life depends to a large degree on the availability of energy. In recent years, photovoltaic technology has been growing extraordinarily as a suitable source of energy, as a consequence of the increasing concern over the impact of fossil fuels on climate change. Developing affordable and highly efficiently photovoltaic technologies is the ultimate goal in this direction.

Dye-sensitized solar cells (DSSCs) offer an efficient and easily implementing technology for future energy supply. Compared to conventional silicon solar cells, they provide comparable power conversion efficiency at low material and manufacturing costs. In addition, DSSCs are able to harvest low-intensity light in diffuse illumination conditions and then represent one of the most promising alternatives to the traditional photovoltaic technology, even more when trying to move towards flexible and transparent portable devices. Among these, considering the increasing demand of modern electronics for small, portable and wearable integrated optoelectronic devices, Fibre Dye-Sensitized Solar Cells (FDSSCs) have gained increasing interest as suitable energy provision systems for the development of the next-generation of smart products, namely “electronic textiles” or “e-textiles”.

In this thesis, several key parameters towards the optimization of FDSSCs based on inexpensive and abundant TiO_2 as photoanode and a new innovative fully organic sensitizer were studied. In particular, the effect of various FDSSCs components on the device properties pertaining to the cell architecture in terms of photoanode oxide layer thickness, electrolytic system, cell length and electrodes substrates were examined. The as obtained FDSSCs were fully characterized in terms of chemical and physical properties, as well as from the electrochemical and photovoltaic point of view. Finally, the metal part of the devices (wire substrate) was substituted with substrates suitable for the textile industry as a fundamental step towards commercial exploitation.

List of Symbol and Abbreviations

AM	Air Mass
ACN	Acetonitrile
ACN	Acetonitrile
bpy	2,2'-Bipyridine
C	Electric capacitance
CB	Conductive Band
CE	Counter electrode
CF	Carbon Fibre
CIGS	Cu(In,Ga)Se ₂
CNT	Carbon Nanotube
CPE	Constant phase element
C_s	Specific Capacitance
CV	Cyclic Voltammetry
Diam.	Diameter
DSSC	Dye-Sensitized Solar Cell
D-π-A	Donor- π bridge-Acceptor
EDS	Energy Dispersive X-ray Spectrometry
E_g	Band gap energy

EIS	Electrochemical Impedance Spectroscopy
EtOH	Ethanol
eV	Electron Volt
FDSSC	Fibre-shaped Dye-Sensitized Solar Cell
FF	Fill Factor
FTO	Fluorine-doped Tin Oxide
Gt	Gigatonnes
HOMO	Highest Occupied Molecular Orbital
ITO	Indium-doped Tin Oxide
Jsc	Short Circuit Current Density
M	mol/L
MeOH	Methanol
MLCT	Metal to Ligand Charge Transfer
MO	Molecular Orbital
MPN	3-Methoxypropionitrile
N719	<i>cis</i> -diisothiocyanato-bis(2,2'-bipyridyl-4,4'-dicarboxylato) ruthenium(II) bis(tetrabutylammonium)
N749	triisothiocyanato-(2,2':6',6''-terpyridyl-4,4',4''-tricarboxylato) ruthenium(II)tris(tetra-butylammonium)
PBT	Polybutylene Terephthalate
PEC	Photoelectrochemical Cell
PEDOT	Poly(3,4-ethylendioxythiophene)

PEN	Polyethylene Naphthalate
PET	Polyethylene terephthalate
PMMA	Polymethyl Methacrylate
PP	Polypropylene
PPy	Polypyrrole
PSS	Polyphenylene Sulphide
PV	Photovoltaic
PVC	Photovoltaic Cell
SCE	Saturated Calomel Electrode
SD	Standard Deviation
SEM	Scanning Electron Microscopy
TBA	Tetrabutylammonium ion
TBT	4-tert-butylpyridine
THF	Tetrahydrofuran
UV-Vis	Ultraviolet-Visible
Voc	Open Circuit Voltage
Z	Impedance
Z'	Real part of Impedance
Z''	Imaginary part of Impedance
ϵ	Molar absorptivity
η	Power conversion efficiency

ρ_L

Linear resistivity

Chapter 1. Introduction

1.1. Energy demand and energy consumption

In the modern world of technological advancement, energy has become one of the basic needs for life. Along with that, the environmental correlated issues, represent one of the most prominent problems in modern society [1].

The world's population continues to grow at a high rate, such that today's population is twice that of 1960, and it is projected to increase further to 9 billion by 2050 [2]. In the early 1990s, cities consumed less than half of the total energy produced, while they currently use two third of the worldwide energy [3], with a globally energy demand rose by 2.3 % in 2018, its fastest pace in the last decade. This exceptional performance, which has been driven by a robust global economy and stronger heating and cooling needs in some regions, lead to an increased demand for all fuels, with fossil fuels meeting nearly 70% of the growth for the second year running [4]. In this scenario, the worldwide power consumption is expected to double in the next three decades [5], and the limited supply of fossil fuels is hardly expected to cope with this, not to mention the direct consequences on the environment; over the last 150 years, burning fossil fuels has resulted in more than 25 % increase in the amount of carbon dioxide in our atmosphere [6], with a global energy-related CO₂ emissions rose by 1.7% to 33 Gt in 2018 [4] as shown in *Figure 1.1*.

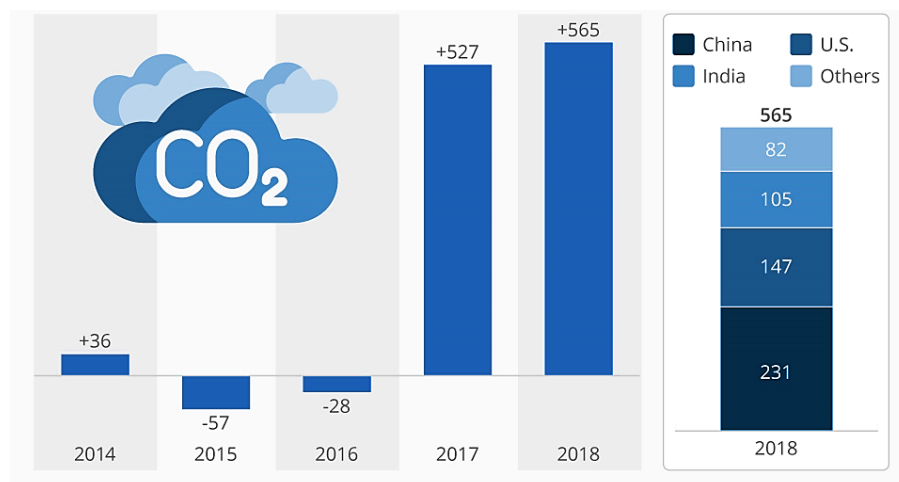


Figure 1.1. Global annual CO₂ emission in million tonnes from 2014 to 2018 showing a grow of emitted carbon dioxide for the second year in a row (source: IEA). Reproduced from Statista.

On the other hand, nuclear power, though capable of providing large scale power generation, is been proven to be guilty in safety and waste management issues, irreversibly signing its credibility as a possible solution to the future energy demand.

1.2. Renewable energy

The abovementioned situation points out the compelling necessity of our society to increasingly dissociate itself from fossil fuels and move towards renewables sources of energy, which literally comprehend any resources that can be immediately regenerated after their utilization [7] and that generally cause a considerably lower environmental impact. The most widespread renewable energies are, nowadays, wind, solar, hydro, tidal, geothermal, and biomass.

The urgent need to turn to renewables brought Europe, in December 2008, to approve the Climate and Energy Package which established an overall policy for the production and promotion of energy from renewable sources and comprehending the so-called 20-20-20 goal: the fulfilling of the 20% increase in energy efficiency, the 20% reduction of CO₂ emissions, and the 20% renewables to be achieved to the attainment of individual national targets by 2020. In December 2018, the revised renewable energy directive entered into force, as part of the Clean energy for all Europeans package, aimed at keeping the EU a global leader in renewables and, more broadly, helping the EU to meet its emissions reduction commitments under the Paris Agreement. The new directive establishes a new binding renewable energy target for the EU for 2030 of at least 32%, with a clause for a possible upwards revision by 2023 [8].

After 2008, the investments in renewables have experienced a substantial increase, with a 32% rise already in 2010 on respect of 2009, contributing up to the 16% to the global energy production [7]. This trend has been maintained so far, as shown in *Figure 1.2*, with Clean Energy investments exceeded \$300 billion once again in 2018, the fifth in a row, according to authoritative figures from research company BloombergNEF (BNEF). Last was a relatively stable year for the market of renewable energy technologies. Total renewable power capacity grew at a consistent pace compared to 2017, and the number of countries integrating high shares of variable renewable energy (VRE) continued to rise. Corporate sourcing of renewables more than doubled compared to 2017, and renewables have spread in significant amounts all around the world [9].

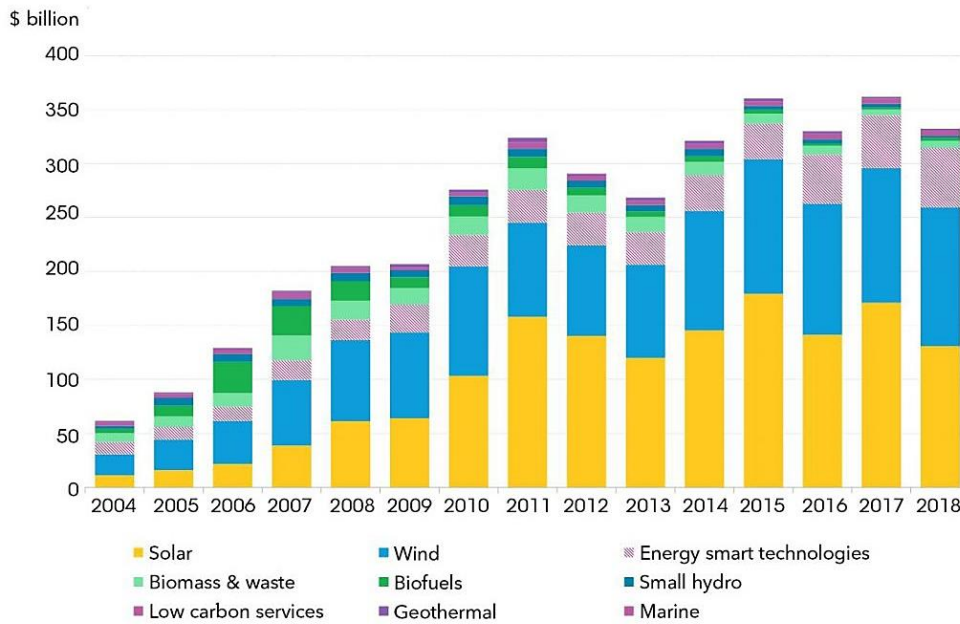


Figure 1.2. Global new investments in clean energy from 2004 to 2018 distinguished by different sectors.
 Reproduced from BloombergNEF.

Renewable energy has been established globally as a mainstream source of electricity generation for several years [10]. The estimated share of renewables in global electricity generation was more than 26% by the end of 2018, as shown by *Figure 1.3*.

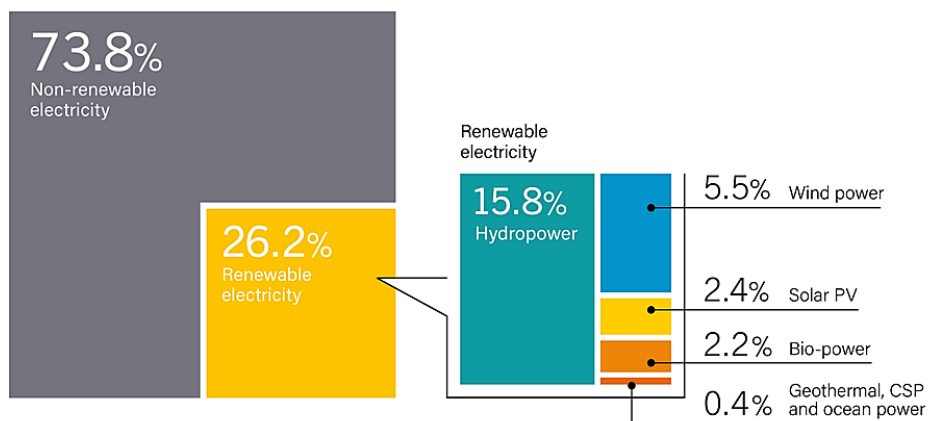


Figure 1.3. Estimated Renewable Energy Share of Global Production at the end of 2018 [11].

Net capacity additions for renewable power were higher than for fossil fuels and nuclear combined for a fourth consecutive year, and renewables now make up more than one-third of global installed power capacity, with solar PV exceeded 20% for the first time

(Figure 1.4). This is due in part to stable policy initiatives and targets that send positive signals to the industry, along with decreasing costs and technological advancements.

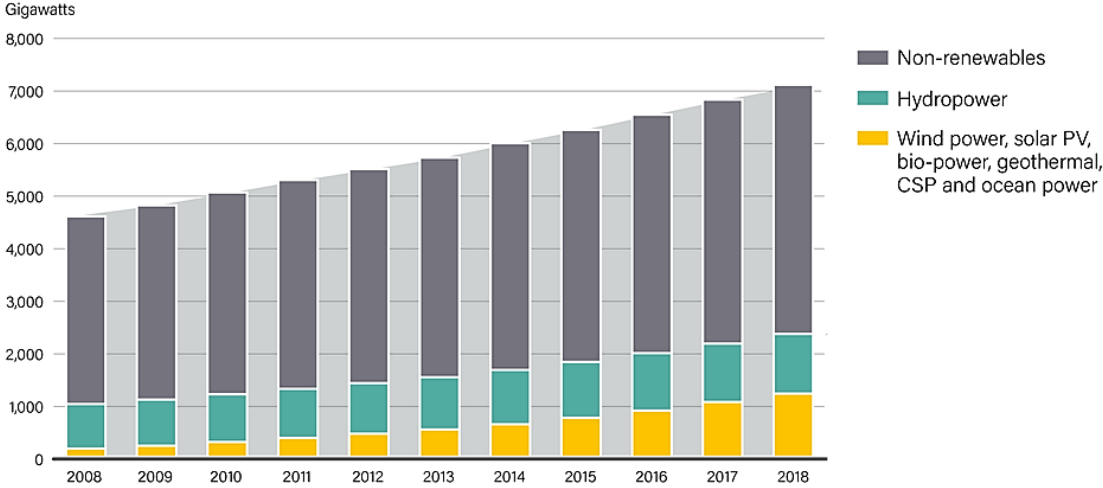


Figure 1.4. Global Power Generating Capacity by Source (2008-2018) [11].

An estimated 181 GW was installed worldwide, slightly above 2017 additions, and total installed capacity grew more than 8%. With around 100 GW added, solar PV was once again the frontrunner for installed renewable power capacity. Additions from solar PV accounted for 55% of new renewable capacity, followed by wind power (28%) and hydropower (11%) [11] (Figure 1.5).

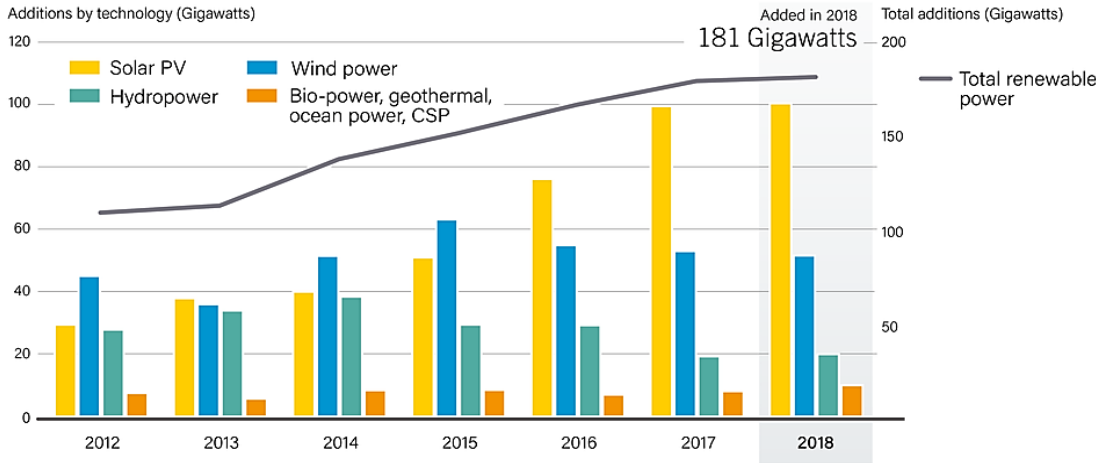


Figure 1.5. Annual Addition of Renewable Power Capacity, by Technology and Total (2012-2018) [11].

Data as the ones just reported, testify an increase attention towards the energetic-climatic situation in the last decade, in particularly motivated by the most accredited climate models, which all agreed in a gradual global warming with subsequent dramatic scenarios for the imminent future.

The transition to a more sustainable progression is happening and the key factor for its realization is the imperative relation between performances and the costs of the relative renewable technologies.

From this point of view, among all other abundant and non-polluting renewable energy sources available in our planet, at the moment solar energy represents the best option.

1.2.1. Solar Energy

Solar energy has the highest potential to satisfy the global need for renewable energy sources. Each year $1.7 \cdot 10^5$ TW strike the earth's surfaces in the form of sunlight [12] which is nearly 10^4 times more than the world's energy consumption [13]. In other words, sun provides us with more energy in an hour than the world human population consumes in a year [14], which is way greater than any other renewable option, as graphically demonstrated by *Figure 1.6*.

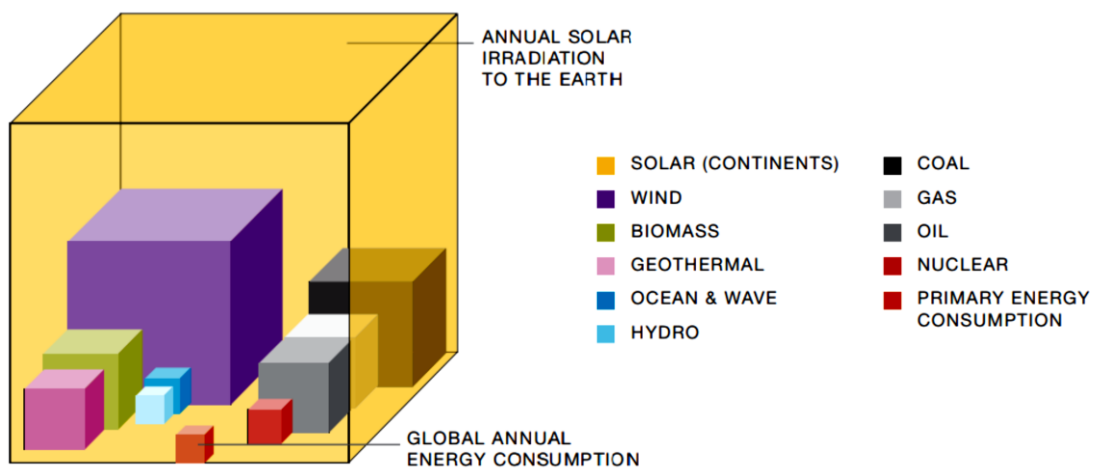


Figure 1.6. Graphic representation of the solar irradiation on versus established global energy resources. Fossil fuels are expressed with regard to their total reserves while renewable energies to their yearly potential [15].

The abundance of this energy reaching earth can be fruitfully utilized in various ways namely Solar Fuel, Solar Electricity (photovoltaics) and Solar Thermal. Among these, photovoltaic devices are the primary solar energy conversion systems to harvest the solar energy as well as one of the most excellent ways used right now, as seen before, to produce electric energy from renewables.

From this point of view an important contribution could be given from the development and improvement of the so-called third generation photovoltaics. Being based on different conversion energy mechanisms on respect to the more traditional Si-based and thin film devices, they are theoretically able to overcome the Shockley–Queisser limit of 31-41% power efficiency for single bandgap solar cell (see Chapter 2). In this category Dye-Sensitized solar cell are located, on the development of which, this thesis is based.

References

- [1] M. Peng and D. Zou, "Flexible fiber/wire-shaped solar cells in progress: Properties, materials, and designs," *J. Mater. Chem. A*, vol. 3, no. 41, pp. 20435–20458, 2015.
- [2] B. G. Desai, "CO₂ emission – Drivers across time and countries," *Curr. Sci.*, 115, pp. 386-387, 2018.
- [3] International Renewable Energy Agency (IRENA) 2016.
- [4] International Energy Association (IEA), 2018.
- [5] Md. I. Khan, "A study on the Optimization of Dye-Sensitized Solar cells", "*Graduate Theses and Dissertation*"(University of South Florida), 2013 .
- [6] Harvard School of Public Health (<http://chge.med.harvard.edu/category/nature-health-built-environment>). .
- [7] "Renewables 2011 – Global Status Report", *REN21 – Renewable Energy Policy Network for the 21st Century*, 2011.
- [8] European Commission (<https://ec.europa.eu/energy/en/topics/renewable-energy>).
- [9] "Corporate clean energy buying surged to new record in 2018", *BloombergNEF (BNEF)*, press release 2019
- [10] M. Motyka, A. Slaughter, C. Amon, "Global renewable energy trends: Solar and wind move from mainstream to preferred", *Deloitte Insights*, 2018.
- [11] "Renewables 2019 – Global Status Report", *REN21 – Renewable Energy Policy Network for the 21st Century*, 2019.
- [12] A. Hagfeldt, G. Boschloo, L. Sun, L. Kloo, H. Pettersson, "Dye-sensitized solar cells," *Chem. Rev.*, 110 pp. 6595-6663, 2010.
- [13] Global Energy Statistical Year Book 2018

- [14] N.S. Lewis, "Towards cost-effective solar energy use", *Science*, 315(5813), pp. 798-801, 2007.
- [15] "Solar Generation 6", EPIA-European Photovoltaic Industry Association, 2011.

Chapter 2. Photovoltaic solar cells

2.1. Solar radiation

Solar radiation is emitted from sun photosphere at about 5800 K [1] with a range of wavelength from the ultraviolet and visible to the infrared with a spectral distribution in the visible region close to that of a black body [2]. It is, however, influenced by atmospheric absorption and by the position of the sun itself.

Ultraviolet light is filtered out by ozone, and water and CO₂ absorb mainly in the infrared making dips in the solar spectrum at 900, 1100, 1400 and 1900 nm (H₂O) and at 1800 and 2600 nm (CO₂) [3], as shown in *Figure 2.1*.

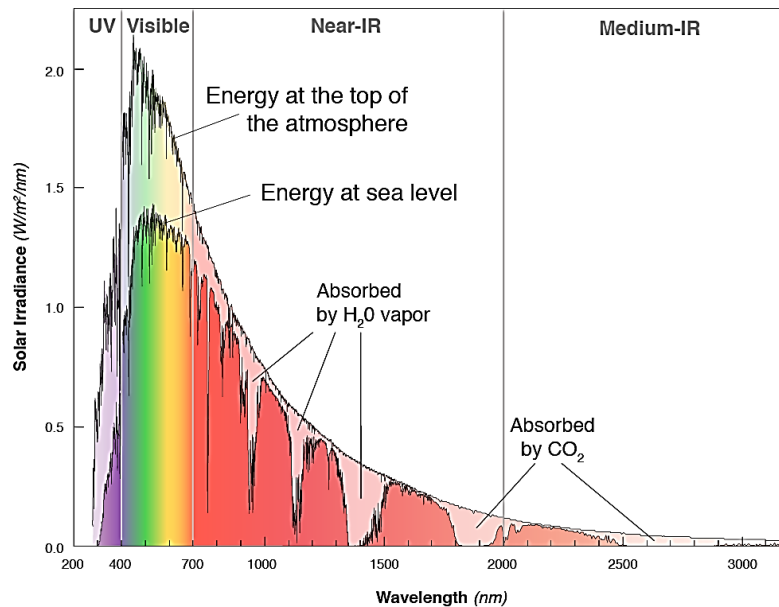


Figure 2.1. Intensity as a function of the wavelength for Solar radiation at the top of the earth's atmosphere and at the surface (sea level).

In addition to the atmosphere composition, the amount of radiation reaching the surface is influenced by climatic conditions (scattering of the light caused by pollution, presence of clouds [3]) and by the position of the sun with respect of the earth, so that in the end, the amount of removed incident energy is approximately 10-45 %. It is easy to comprehend why, when skies are clear, the maximum radiation strikes the terrestrial surface when the sun is directly overhead, having the shortest path length through the

atmosphere. In other words, the attenuation of solar light throughout the atmosphere is a function of the optical path. This coefficient, usually indicated as Optical Air Mass or simply Air Mass (AM), for a path length L through the atmosphere, and solar radiation incident at angle z relative to the normal to the Earth's surface, is [4]:

$$AM = \frac{L}{L_0}$$

where L_0 is the path length at zenith (z) and at sea level. The air mass number is thus dependent on the Sun's elevation path through the sky and therefore varies during the day, with the passing seasons of the year, and with the latitude of the observer. For these reasons, the performances related to a given photovoltaic module are strictly correlated to the location of the module itself. A first-order approximation for the AM is given by:

$$AM = 1/\cos \varphi$$

where φ is the angle of elevation of the sun. Thus, when the sun is at its zenith ($\varphi = 90^\circ$), the AM value is unitary. The above approximation overlooks the atmosphere's finite height, and predicts an infinite air mass at the horizon. However, it is reasonably accurate for values of φ up to 75° .

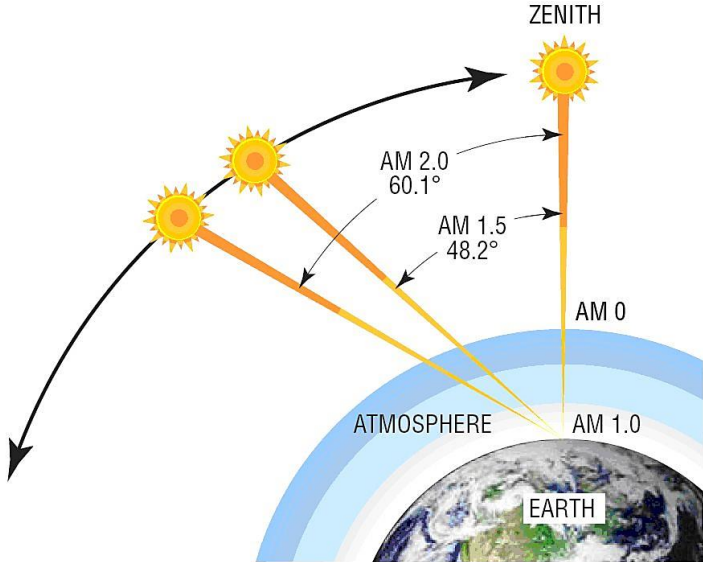


Figure 2.2. Representation of different AM values.

Figure 2.2. illustrates different sun's configurations with their relative AM values associated. AM0 ("zero atmosphere") is the value used for application of solar panels

outside the earth atmosphere (“Energy at the top of the atmosphere” – *Figure 2.1*), instead AM1.5 is the standard value used for the calibration and measurement of terrestrial power-generation panels (“Energy at sea level” – *Figure 2.1*). It was selected in the 1970s for standardization purposes (ASTM G-173), based on an analysis of solar irradiance data in the conterminous United States [5]. It originates from a φ of about 48° ($48^\circ 12' 0''$). While the summertime AM number for mid-latitudes (most-common area of installation) during the middle parts of the day is less than 1.5, higher figures apply in the morning and evening and at other times of the year. Therefore, AM1.5 is a good representation of the overall yearly average sun illumination. The corresponding spectrum is normalized so that the integrated irradiance, which is the amount of radiant energy received from the sun per unit area and unit time, is 1000 W/m^2 .

2.2. Photovoltaic Technologies

Photovoltaics (PV) is the collective name for devices converting the energy of the sun, photons, into electricity, and represent the primary solar energy conversion systems to harvest the solar energy. First report on photovoltaic concept dates back to the end of the XIX century with two major contributions: one from the French physicist Alexandre-Edmond Becquerel in 1839, describing the generation of a photocurrent (photovoltaic effect) [6], and the first real reports on photoconductivity made by Smith and Adams in 1873 and 1876, respectively, working on selenium [7][8].

The PV effect is found in a semiconductor material, characterized by an intermediate behaviour of electron conduction between the one of a conductor, and that of an insulator [9]. When the incident radiation in the form of photons reaches the material, these are captured by electrons, resulting in higher energy content, and if a threshold value is exceeded (the band gap), they can break their nucleus links and circulate through the material. This electron flow generates a difference of potential between the terminals, and upon application of an electric field on the semiconductor, electrons move in the direction of the field, generating an electrical current [10]. Photovoltaic Cells (PVCs) present an architecture based on joining two semiconductor regions with different electron concentrations (*Figure 2.3*). These materials can be type n - semiconductor with excess of electrons as a result of the incorporation with electron donor elements - or type p - semiconductors with an excess of positive charge, called holes, promoted by doping

the materials with acceptor elements, so that an electronically neutral system is obtained. When both p and n regions are in contact, photogenerated holes flow from the p region and photogenerated electrons from the n region through the p-n junction, generating a diffusion current. In addition, the fixed ions near the junction generate an electron field in the opposite direction to the diffusion, which leads to a drift current. At equilibrium, the diffusion current is balanced with the drift current, so that the net current is zero. In this condition, a potential barrier is established at the p-n junction, called built-in potential.

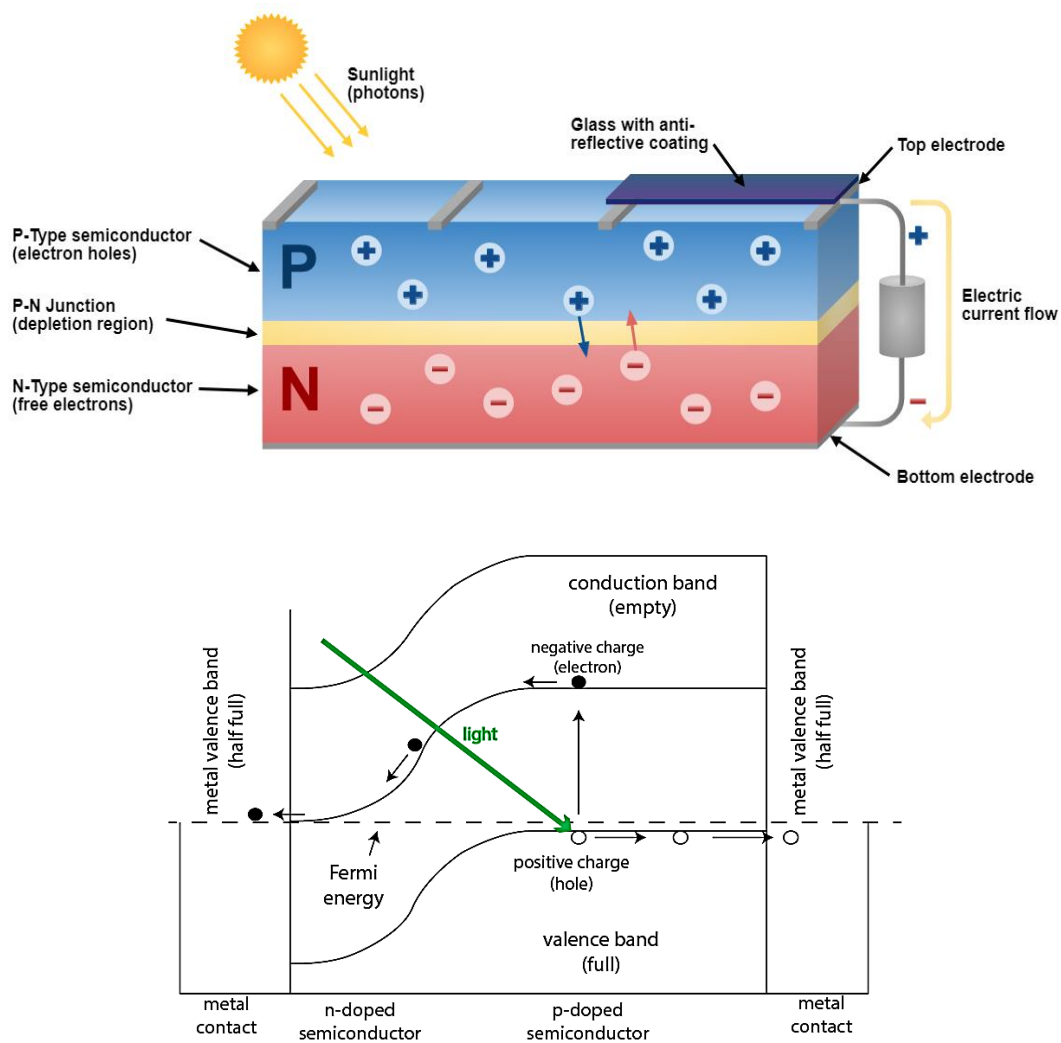


Figure 2.3. Representation of a p-n junction solar cell (top) and schematic representation of working mechanism (down).

PVCs are usually classified into three major categories called generations [9] (Figure 2.4):

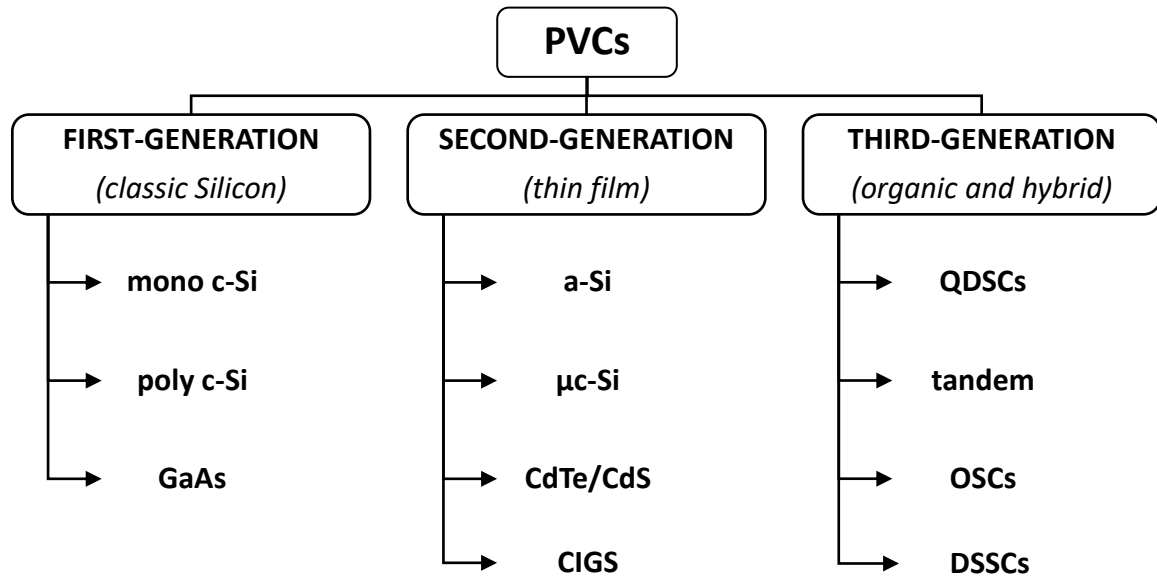


Figure 2.4. Classification of Photovoltaic technologies.

- *First-generation*: it is based on crystalline silicon technologies, both monocrystalline (mono c-Si) and polycrystalline (poly c-Si), and on gallium arsenide (GaAs).
- *Second-generation*: it includes amorphous silicon (a-Si) and microcrystalline silicon (μ c-Si) thin films solar cells, cadmium telluride/cadmium sulphide (CdTe/CdS) and copper indium gallium selenide (CIGS) solar cells.
- *Third-generation*: it involves technologies based on newer compounds including active quantum dots (QDSCs), tandem or stacked multilayers of inorganics based on III–V materials, such as GaAs/GaInP, organic (polymer)-based solar cells (OSCs) and Dye-Sensitized solar cells (DSSCs).

Another generation, called fourth-generation, also known as “inorganics-in-organics” is sometimes added. It combines the low cost/flexibility of polymer thin films with the stability of novel inorganic nanostructures such as metal nanoparticles and metal oxides or organic-based nanomaterials like carbon nanotubes, graphene and its derivatives. Nevertheless, there is a controversy concerning the existence of this generation, since some authors include it in the forefront of the third one while other believe that it is a different one [9].

2.2.1. Solar Cells Terminologies

An in-depth analysis of solar cells requires to firstly introduce some parameters that helps describing unequivocally the device performances so that a comparison between generations can be carried out. In this section a general introduction to characteristic parameters of solar cell will be given [3][11][12]. A thorough discussion of these terms can be found in Chapter 3 and 5.

2.2.1.1. Open-Circuit Voltage

Open-circuit voltage (V_{OC}) is the maximum possible voltage [V] across a photovoltaic device, which is obtained when no current is flowing through the solar cell under solar illumination, *i.e.* when a load with infinity resistance is attached to its terminals. A solar cell can thus operate in a voltage range equal to 0- V_{OC} . Outside these limit values, the energy is no longer generated but need to be provided

2.2.1.2. Short-Circuit Current

Short-circuit current (I_{SC}) [mA] is defined as the current that flows through an illuminated solar cell when there is no external resistance, *i.e.* when the electrodes are simply connected, and cell is short-circuited. I_{SC} is the maximum current that a photovoltaic device is able to produce; under an external load the current will always be less than this value.

The short circuit current depends on a number of factors, such as the illuminated area (A) of the solar cell. To remove the dependence of the solar cell area it is common to list I_{SC} as Short-circuit current density (J_{SC}) [mA/cm²]:

$$J_{SC} = \frac{I_{SC}}{A}$$

In this way it is possible to compare performances of different size devices.

2.2.1.3. *Fill Factor*

Fill Factor (FF) represents how “difficult” or how “easy” the photogenerated charge can be extracted out of a photovoltaic device. It is, in other words, a measure of the ideal behaviour of the solar cells (unitary FF) being defined as the ratio of the actual maximum power output (P_{\max}) to its theoretical power output, if current and voltage would be at their maxima, *i.e.* I_{SC} and V_{OC} respectively. FF can be written down as follow:

$$\text{FF} = \frac{P_{\max}}{I_{\text{SC}} \cdot V_{\text{OC}}} = \frac{I_{\max} \cdot V_{\max}}{I_{\text{SC}} \cdot V_{\text{OC}}}$$

where I_{\max} and V_{\max} are respectively the current and the potential at the maximum power.

2.2.1.4. *Power Conversion Efficiency*

The Power Conversion Efficiency (PCE) also indicated as η , is the ratio of maximum electrical energy output (P_{OUT}) to the energy input (P_{IN}), *i.e.* the fraction of incident power converted to electricity. PCE measures the amount of power produced by a photovoltaic device relative to the power available in the incident solar radiation. The energy input has thus the standard value of 1000 W/m^2 , which is, how previously described, the internationally recognized standard condition for the efficiency measurement of solar cell (A.M 1.5) as previously described. It is the most commonly used parameter to compare the performance of one solar cell with another. PCE is generally expressed in percentage and can be written, on the basis of what has been formerly said, as:

$$\eta = \frac{P_{\max}}{P_{\text{in}}} = \frac{\text{FF} \cdot V_{\text{OC}} \cdot I_{\text{SC}}}{1000[\text{W} \cdot \text{m}^{-2}]}$$

2.2.2. *Photovoltaic generations*

2.2.2.1. *First-generation PVCs*

The first-generation comprises photovoltaic technology based on thick crystalline silicon films, which is the most widely used semiconductor material for commercial solar cells (90% ca. of the current PVC market [9]), and cells based on GaAs, the most commonly

applied for solar panels manufacturing. These are the oldest and the most used cells due to their reasonably high efficiencies, albeit their cost of production is relatively high.

Silicon-based cells may be monocrystalline or polycrystalline with large grain size [12]. The first ones (m-Si), obtained by the Czochralski process, are made of p-n silicon junctions and have been able to achieve an efficiency of the order of 24.4% [9]. However, the manufacturing process involves high production cost. The polycrystalline cells (p-Si), on the contrary, are manufactured by melting the silicon and solidifying it to orient crystals in a fixed direction and produce multi-crystalline Si, which is then sliced into thin wafers. The efficiency of the polycrystalline cell is approximately 20.4%, lower than the m-Si, but it is compensated by their lower production costs and the reduced number of defects in the crystal structure [13]. The main reason for the smaller efficiency is the lower material quality due to grain boundaries and the higher concentration of impurities. Therefore, the influence of recombination in p-Si cells is higher than in m-Si ones, which leads to slightly lower voltage. Current is also lower due to incomplete carrier collection in these devices [9].

Although the use of Si has some advantages [14], GaAs is able to reach efficiencies in the range of 18.4-28.8% in the laboratory, depending on whether they have a crystalline structure or they consist of a thin layer. One of the main advantages of GaAs is that it offers a wide range of potential design options. GaAs-based cells can have several layers with a slightly different composition that allow a more accurate control of the generation and collection of electrons and holes than silicon cells, which are limited to changes in the level of doping to achieve the same results. This higher degree of control allows to achieve efficiencies closer to the theoretical limit. Further, GaAs is frequently used in multi-junction solar cells, where each p-n junction produces an electric current in response to different wavelengths of light. The use of multiple semiconducting materials allows the absorption of a broader range of wavelengths, thus improving the energy conversion efficiency of the cell [9].

2.2.2.2. *Second-generation PVCs*

Thin-film cells are considered as the second-generation PV cells. They have lower costs than the first-generation ones, yet they have a smaller share of the market because of

their lower efficiency (*Table 2.1*) [13], the best being 22.3% for CIGS in the laboratory [9].

Table 2.1. Laboratory record efficiency for different type of second-generation PVCs [9].

type of II generation PVCs	record efficiency
a-Si	10.2% (single junction)
	12.7% (multi junction)
CdTe	21.0%
CIGS	22.3%

The aim of reducing the high costs associated with the first-generation is achieved by using lower amount of material and of poorer quality, deposited on cheap substrates [9] (glass or polymeric). The principal materials used are a-Si, Cu(In,Ga)Se₂ (CIGS) and CdTe. Their electronic structures, which differ from crystalline Si, enable these materials to absorb sunlight throughout layers way thinner than the ones needed for first generation solar cells, sometimes only one micrometer thick, because of their high absorption coefficient. However, they also present some drawbacks besides the lower efficiencies, like the light-induced degradation in first stages of outdoor usage and the higher degradation in outdoor uses. The semiconductor deposited onto glass can generate a flow of ions in the glass or other substrate, causing a decrease in layer thickness over time, which means that thicker layers would be required to ensure long-term operation [9]. Moreover, most second-generation PVCs make use of rare metals, like indium, or toxic metals especially in environmental contexts, like cadmium.

2.2.2.3. *The Shockley-Queisser limit*

A common disadvantage of the first two generations of photovoltaic cells is that they are limited by the Shockley-Queisser theoretical limit for a single p-n junction. It was first calculated by William Shockley and Hans-Joachim Queisser in 1961, giving a maximum efficiency of 30% at 1.1 eV [15]. This calculation, however, used a simplified model of the solar spectrum, and more recent calculations give a maximum efficiency of 33.7% at 1.34 eV [16]. There are several processes limiting the efficiency of a PV device (*Figure*

2.5), one of the most important is the limitation in absorption of photons, which derives from the value of the band gap of the material used for the solar cells. As a consequence, the photon from the sun with less energy cannot contribute to the efficiency of the PV system.

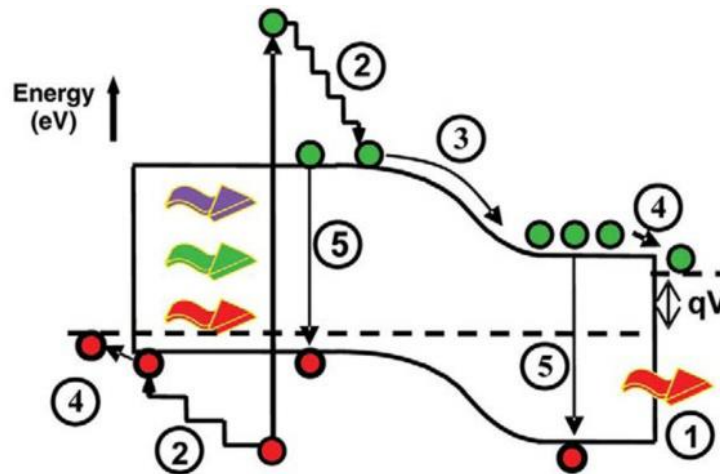


Figure 2.5. Loss processes in standard solar cell: non-absorption of below-bandgap photons (1), lattice thermalization loss (2), junction and contact voltage losses (3,4), recombination loss (5) – radiative recombination is unavoidable [17].

Another limitation is represented by photons having more energy than the band gap, exciting electrons to higher energy levels and holes to lower levels in the atoms/molecules. Before the transport in the semiconductor the electrons relax down to the lowest energy level (bottom) of the conduction band and the holes move up to the ground-state level of the valence band of the semiconductor. This process, known as thermalization of photon energies exceeding the band gap, cannot contribute to the efficiency of the solar cell because the energy difference is lost [18].

2.2.2.4. Third-generation PVCs

Third-generation photovoltaic solar cells arise from the idea of increasing device efficiency and reducing the distance to the Carnot limit, which is about 62% above the Stockley-Queisser limit of 33% [19], while achieving higher environmental friendliness through the use of non-toxic and very abundant materials.

The main attraction of these cells is their low cost. They aim at reducing power costs to about 50% to 80% as compared with the second-generation cells.

These devices use the unique flexibility of quantum-well and quantum-dot nanostructures to optimize absorption, carrier generation, and separation. Quantum dots can be mixed with solutions and applied on the film using spin coating technology.

Organic solar cells (OSCs) and dye-sensitized solar cells (DSSCs) are the most important third-generation cells. In OSCs, an organic absorbing layer is placed between two different electrodes. One of the electrodes is transparent or semi-transparent and often made up of Indium tin oxide (ITO). The other electrode is commonly made up of aluminium; however, sometimes other materials like magnesium and gold are also used. The organic light absorbing layer consists of a mixture of light-sensitive conjugated polymers (such as phthalocyanine) or small molecules and fullerene-like compounds to absorb light and set their electricity generating events in motion [13].

The efficiency reported for OSCs are between 9.7-11.2% with the best laboratory performance equal to 22.4 % attained with P3HT as donor material [9].

The DSSCs have a reverse concept to light emitting diodes (LEDs) and their working mechanism mimics the natural photosynthetic process. These cells, unlike the previous systems based on solid-state p-n junction materials, are photoelectrochemical devices where the phase in contact with the semiconductor is an electrolyte (liquid, gel or solid). The light is absorbed by a sensitizer (a dye molecule), which is fixed to the surface of a wide-band semiconductor. At the interface, charge separation is promoted through the injection of photo-induced electrons from the dye into the conduction band of the solid (TiO_2). Electrons then diffuse in the conduction band as a result of electron concentration gradient to the charge collector or anode. These cells are reported to have a solar-to-electric conversion efficiency over 10% [13], which is strictly correlated to the nature of the employed dye, to the electrolytic system used and to the structure of the semiconductor as well but that do not change drastically with a change in temperature as happens for the other PV systems [20].

For each photovoltaics technologies developed up to now, an efficiency chart related to laboratory prototypes is reported in *Figure 2.6*.

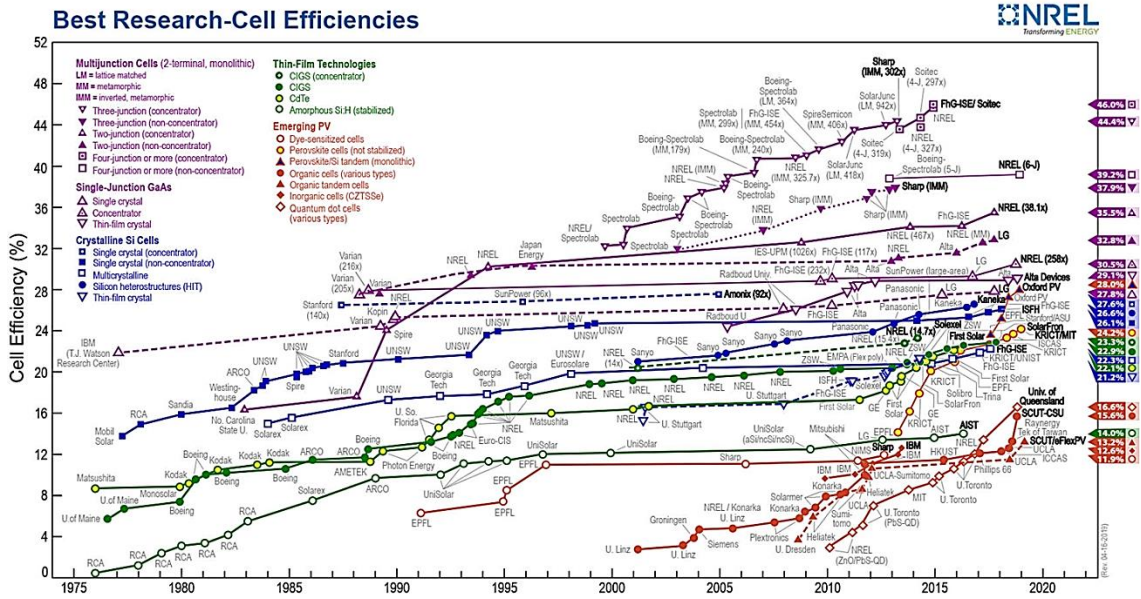


Figure 2.6. Best Research-cell efficiency for each photovoltaics technologies developed till 2019 [21].

References

- [1] "Sun: Facts & Figures", NASA Solar System Exploration (<http://solarsystem.nasa.gov/planets/profile.cfm?Object=Sun&Display=Facts>).
- [2] "Black Body and Black Body Radiation" in *Encyclopedia of Color Science and Technology*, pp.1-5, 2015.
- [3] A. Hagfeldt, G. Boschloo, L. Sun, L. Kloo, H. Pettersson, "Dye-sensitized solar cells," *Chem. Rev.*, 110 pp. 6595-6663, 2010.
- [4] P. Würfel "The Physics of Solar Cells", Weinheim: Wiley-VCH, 2005.
- [5] C. Gueymard,, D. Myers, K. Emery, "Proposed reference irradiance spectra for solar energy systems testing", *Solar Energy*. 73 (6), pp.443–467, 2002.
- [6] A. E. Becquerel, "Memoire sur les Effects d'Electriques Produits Sous l'Influence des Rayons Solaires," *Compt. Rend. de Acad. Sci.*, Vol. 9, pp. 561-567, 1839.
- [7] W. Smith, "Effect of Light on Selenium During the Passage of An Electric Current", *Nature*, 7, pp. 303, 1873.
- [8] W. G. Adams, R. E. Day, "The Action of Light on Selenium", *Proc. R. Soc. London*, Vol. 25, pp. 113-117, 1876.
- [9] J. A. Luceño-Sánchez, A. M. Díez-Pascual , and Rafael Peña Capilla, "Materials for Photovoltaics: State of Art and Recent Developments", *Int. J. Mol. Sci.*, 20, pp.976-1017, 2019.
- [10] B. Zaidi B. "Introduction to Photovoltaic Effect" in *Solar Panels and Photovoltaic Materials*, InTech Open: London, pp-1-8, 2018.
- [11] H. Peng, "Fiber-Shaped Dye-Sensitized Solar Cell" in *Fiber-Shaped Energy Harvesting and Storage Devices*, Nanostructure Science and Technology, Springer-Verlag Berlin Heidelberg, pp.39-60, 2015.

- [12] M. Pazoki, U.B. Cappel, E. M. J. Johansson, A. Hagfeldt, G. Boschloo, "Characterization techniques for dye-sensitized solar cells", *Energy Environ. Sci.*, 10 (3), pp. 672-709, 2017.
- [13] M. B. Hayat, D. Ali, K. C. Monyake, L. Alagha, N. Ahmed, "Solar energy – A look into power generation, challenges, and a solar-powered future", *Int. J. Energy Res.*, 43, pp. 1049-1067, 2019.
- [14] A. M. Kuhlmann, "The Second Most Abundant Element in the Earth's Crust", *JOM*, 15, pp. 502-505, 1963.
- [15] W. Shockley, H. J. Queisser, "Detailed Balance Limit of Efficiency of p-n Junction Solar Cells", *J. Appl. Phys.*, 32, pp- 510-519, 1961.
- [16] S. Rühle, "Tabulated values of the Shockley–Queisser limit for single junction solar cells", *Solar Energy*, 130, pp. 139-147, 2016.
- [17] G. Coniber, "Third-generation photovoltaics", *Mater. Today*, 10, pp. 42-45, 2007.
- [18] H. Ellis, "Characterization of dye-sensitized solar cells: components for environmentally friendly photovoltaics", *Dissertation for the Licentiate of Philosophy in Physical Chemistry*, Uppsala University, 2014.
- [19] M. A. Green, "Third generation photovoltaics: Ultra-high conversion efficiency at low cost", *Prog. Photovolt.*, 9, pp.123-135, 2001.
- [20] A. Hagfeldt, G. Boschloo, L. Sun, L. Kloo, H. Pettersson, "Dye-sensitized solar cells," *Chem. Rev.*, 110 pp. 6595-6663, 2010.
- [21] "Research Cell Efficiency Records", National Renewable Energy Laboratory (NREL), 2019.

Chapter 3. Dye-sensitized Solar Cells

3.1. *Dye-Sensitized Solar Cells*

Although the electricity generation capability of organic dyes has been known since late 1960s, the first attempt to generate electric energy from a dye sensitized semiconductor film dates back to 1972 [1] when ZnO was sensitized with Chlorophylls creating the first example of “Artificial Photosynthesis”. This opened the door to basic research on Dye-Sensitized Solar Cells (DSSCs) during the 1970-80 [2][3][4], but it was not until the fundamental work of Grätzel and O’Regan in 1991 [5], introducing the semiconductor mesoporous structure (efficiency $\sim 7\%$) instead of the so far employed compact layers (efficiency $\sim 1\%$), that the feasibility of DSSCs as alternative energy source was proven. As underlined by the first article, the idea behind the mechanism of a Dye-Sensitized Solar Cell is that of an “Artificial Photosynthesis”. In natural photosynthesis, through the presence of chlorophyll, plants absorb light producing electrons that are transferred to the reaction centres of the plants for the production of glucose and oxygen. Likewise, DSSCs, through the use of a dye molecule which absorbs light, produce electrons (see section 3.2)

They represent an emblematic example of the so-called photoelectrochemical cells (PEC) [6]. As already previously mentioned (*chapter 2*), these photocurrent generating devices differ from the first and second PV generations which were based on solid-state junction system, being composed by a semiconductor in contact with an electrolyte, usually a liquid system. The most striking difference between DSSCs and the conventional Si-based PVs is thus that the former contain two interfaces at which charge transport has to switch from electronic to ionic and vice versa. Moreover, while in previous technologies the photoactive material is responsible for both light absorption and charge separation, in the latter this does not happen. As electrochemical photovoltaic cells, DSSCs have the advantages, comparing with the solid photovoltaic, of not being sensitive to the defects in semiconductors, and of being based on a solid-liquid junction which is easier to form. In addition, in the normal operating temperature of 25-65°C, DSSCs efficiency is nearly temperature-independent and they work better in diffuse light or in cloudy conditions (*i.e.* real outdoor conditions). These unique features, along with their lower production costs related to the inexpensive materials and simple fabrication process, their lower

investment costs compared to conventional PV, their design opportunities (transparency and multicolour options) , their light weight and their potential for indoor applications [7], paved the way for intensive research interest, which had reflected a tremendous increase in the number of publications in the last decade [8].

3.2. Structure and Operating Principle

The mechanism of DSSCs involves the use of a dye as a photosensitizer in order to adsorb the sunlight, as reported by the schematic representation of a standard liquid DSSC in *Figure 3.1*.

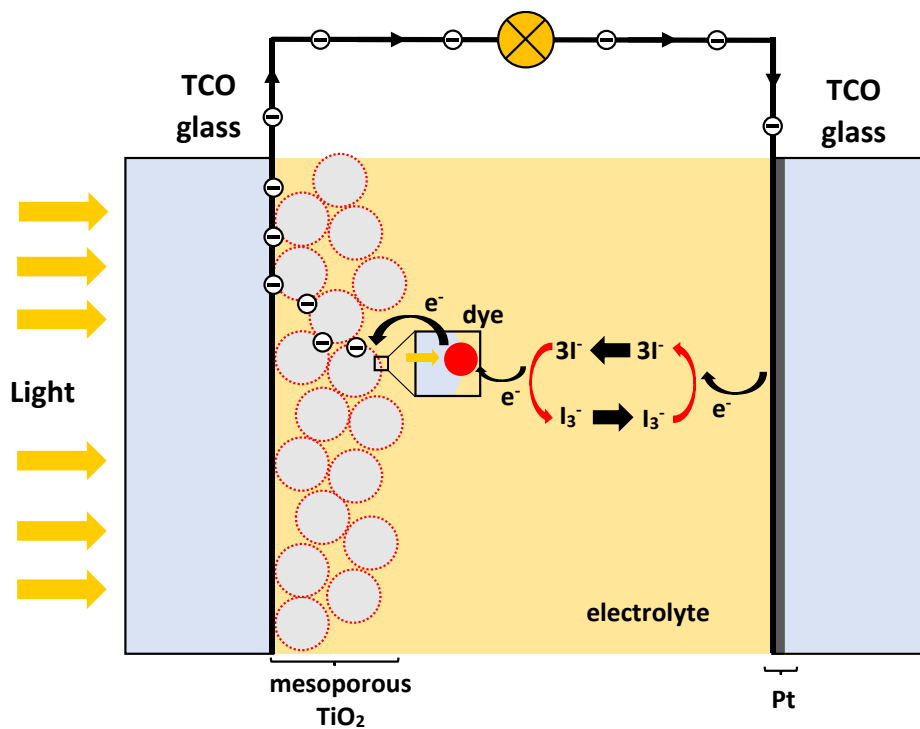


Figure 3.1. Schematic representation of a DSSC.

The system is composed of four main components [7][8]:

- (i) a photoanode made up of a transparent glass sheet covered with a conductive layer (indium-doped tin oxide – ITO – or fluorine-doped tin oxide – FTO), which acts as a substrate allowing light to pass through, on top of which a mesoporous

semiconductor layer (typically TiO_2 , ZnO , SnO_2) is deposited, with the function of transferring electrons.

- (ii) a monomolecular layer of dye sensitizer (typically Ru complexes) absorbed on the surface of the mesoporous oxide layer to harvest incident sunlight and generate photon-excited electrons.
- (iii) an electrolyte (usually an organic solvent) which allows the ionic contact between the photoanode and the counter electrode (iv) containing a redox mediator (usually the couple I^-/I_3^-) to collect electrons at the counter electrode and promote dye regeneration
- (iv) a counter electrode (cathode) made of an ITO or FTO conductive layer deposited on a glass sheet coated with a catalyst (typically platinum) to catalyse the redox couple regeneration reaction and collect electrons from the external circuit.

When the sunlight strikes the DSSC, dye sensitizers on the surface of TiO_2 film get excited and in turn the electrons get injected into the conduction band of TiO_2 . Within the TiO_2 film the injected electrons diffuse all the way through the mesoporous film of the photoanode, they are extracted on the backside of the electrode and utilized to do useful work at the external load. Finally, to complete the cycle, these electrons are collected by the electrolyte at the counter electrode where they reduce the oxidized species of the redox couple in the electrolyte. At this point the reduced species in the electrolyte diffuses to the oxidized dye and regenerates it by reduction.

Therefore, as indicated by Grätzel [9], the dye in DSSCs acts as a molecular electron pump. The dye absorbs visible light, pumps an electron into the semiconductor, accepts an electron from the reduced state of the redox couple in solution and then repeats the cycle.

Figure 3.2 shows a thermodynamic diagram of a dye-sensitized solar cell with the basic electron transport processes indicated by numbers (1-6) to help understanding the whole complex working mechanism behind a DSSC. The reactions are numbered in accordance to the kinetic of the processes. The sensitizer molecule (S) harvests photons that excite an electron from its highest occupied molecular orbital (HOMO) to the lowest unoccupied molecular orbital (LUMO), taking the sensitizer to its excited state (S^*) (reaction 1). To dissipate the excess of energy acquired, the sensitizer (S^*) injects an electron in the

conduction band of the mesoporous semiconductor (reaction 2) to form the oxidized sensitizer (S^+). The electron, thanks to the electronic conduction of the sintered semiconductor nanoparticles, is transferred through the TiO_2 film to the conductive glass. The oxidized dye (S^+) receives electrons (reaction 3) from the reduced component of the redox couple (I^-) in the electrolyte (simply indicated as RE), which regenerates the dye (S) while reducing RE to its oxidized form (I_3^- - simply indicated as OX). The OX migrates to the cathode, and the circuit is completed by the immigration of an electron that has travelled to the external circuit, which regenerates the reduced form of the redox couple (reaction 4) [10].

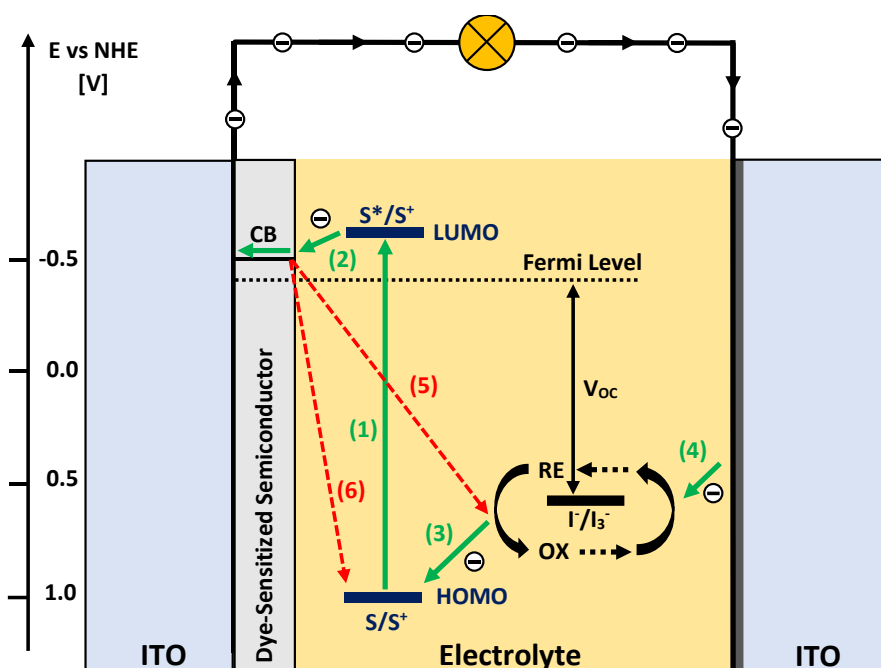
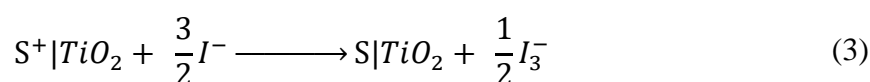
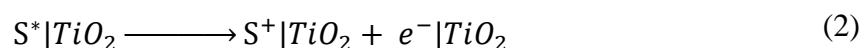


Figure 3.2. Basic energy level diagram for a DSSC. The basic electron transfer processes are indicated by numbers (1-6). Reactions in green (1-4) are required for the light-to-electric conversion. Reactions in red (5-6) are responsible for the loss in efficiency of the device.

For a DSSC to function, it is clear that the injection process (reaction 2) needs be faster than the decay of the excited state of the dye (S^*) to its ground state (dye relaxation), *i.e.* the time scale of reaction 2 has to be shorter than the excited state lifetime of the dye.

Besides the desired pathway of the electron transfer processes described by the abovementioned reactions, which are required and advantageous for completing the light-to-electric conversion, there are two competitive reactions, usually referred as “Dark Reactions”, related to the charge carrier recombination, which are disadvantageous for the efficiency of DSSCs because of the related subtraction of electrons to the whole process. The first one (reaction 5) consists in the recombination of electrons within the semiconductor layer with the oxidized form of the redox couple (OX) to form the reduced form RE. In principle, electron transfer can occur either at the interface between the nanocrystalline oxide and the electrolyte or at areas of the substrate (FTO or ITO) that are exposed to the electrolyte. In practice, the second route can be suppressed by using a compact layer of the oxide metal deposited onto photoanode substrate named “blocking layer” (see section 3.3.1.1.) [7]. The other (reaction 6) is the electron recombination with the oxidized dye (S^+) to give the sensitizer in its reduced state (S).



Fortunately, these two reactions do not play a remarkable negative effect owing to their slower reaction speed compared to that of the forward reactions (1-4) [10] as shown by *Figure 3.3*.

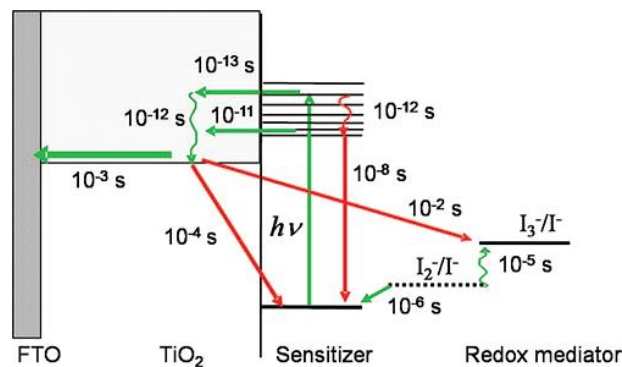


Figure 3.3. Typical time constant for the forward reactions (green) and dark reactions (red) in a Ru-dye-sensitized solar cell with iodide/triiodide electrolyte. Reproduced with permission from [7].

As underlined by the image, besides the above-mentioned reactions, the diffusion of electrons in the semiconductor layer and the diffusion of the redox couple within the electrolyte film ought to be considered to understand the overall performance of DSSCs.

What was in fact outstanding when Grätzel and O'Regan published their fundamental work introducing mesoporous structure in 1991 [5] was the highly efficient transport through the nanocrystalline TiO₂ layer, which was responsible for the significant energy conversion improvement (7.9 %) with respect to the previous compact layer-based devices (1%). The highly porous photoanode is rather different compared with the compact analogue: it can be seen as an ensemble of individual particles through which electrons can percolate by hopping from one crystallite to the next [7].

If we refer again to *Figure 3.2*, it is clear that a fundamental aspect for the function of DSSCs is represented by the difference in energy, upon illumination of the photoanode, between the electrochemical potential proper of electrons in the semiconductor, *i.e.* *quasi*-Fermi level, and the redox potential of the redox couple in the electrolyte. This energy difference is in fact the driving force which pushes electrons from the semiconductor to the hole carrier in the electrolyte and it is responsible for the relative generated photovoltage. At equilibrium the practical maximum photovoltage, *i.e.* the V_{OC} , is thus reachable, which is given by the difference between the energy of the semiconductor conduction band, the Fermi level, and the electrolyte redox potential [11][12].

3.3. *Components*

From what described so far, it should be quite clear that a proper functioning of DSSCs can only derive from an optimization of materials composing the devices which are strictly correlated to the main PV parameters, namely V_{OC} , J_{SC} and FF. Therefore, it becomes crucial the thorough knowledge of each single cell component so that a maximized efficiency and optimized performances can be attained. For this reason, in this section, the main components of a Dye-Sensitized Solar Cell will be shortly considered individually.

3.3.1. Nanostructured Metal Oxide Electrodes

In the early studies of photoelectrochemical systems a monolayer of semiconductors was used, leading to an intrinsic limitation as the monolayer only could absorb a limited amount of light, and only the monolayer of dye bound to the surface could inject electrons into the semiconductor. The key to the breakthrough for DSSCs in 1991 was, as already stated before, the use of a mesoporous electrode with a consequently higher internal surface area, to support the monolayer of the sensitizer. Typically, the increase of surface area by using mesoporous electrodes is about of a factor 1000 for these systems [7] which directly reflects on the amount of absorbable sensitizer onto the surface and thus to the photocurrent generated.

In the early history of the development of DSSCs, many different semiconductors were used for the photoanodes. In *Figure 3.4* a collection of different semiconductors is illustrated. Among these the most used metal oxide for DSSCs application is TiO_2 , followed by ZnO , and SnO_2 because of their wide-bandgap and availability.

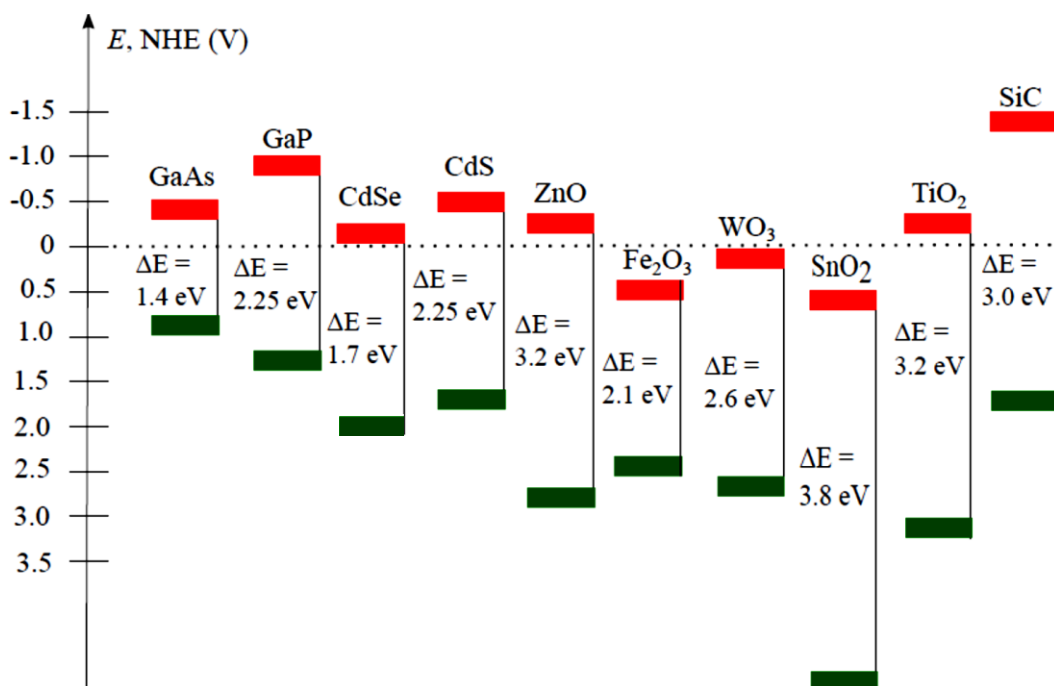


Figure 3.4. The band positions of several semiconductor in contact with aqueous electrolyte at pH 1. The conduction band edge is represented in red while the valence band in green. Adapted from [13].

3.3.1.1. TiO_2

TiO_2 is a stable, nontoxic and cheap oxide which has been mostly used since the initial works on DSSCs in form of anatase, because of a larger bandgap on respect of the other polymorph forms (3.2 vs 3.0 eV for rutile) and a higher conduction band edge energy (CB). This leads to a consequently higher Fermi level and thus to a higher V_{OC} in DSSCs applications [7]. A more accurate description of synthesis with an extensive overlook of the different kinds of TiO_2 hierarchical structures, such as nanorods, nanowires, nanobowls, nanotube *etc.* employed to boost the charge transfer in the semiconductor (i.e. short photoelectron transport and an increased electron transport rate) and to enhance the surface area (*i.e.* amount of loaded dye) can be found in references [7][8][14][15].

Usually, the produced nanoparticles (average diam. 20 nm [12]) are formulated in a paste with polymeric additives and deposited onto a conductive glass substrate by doctor blading or screen-printing. Finally, the film is sintered at 450 °C in air to remove organic components and to generate electrical connection between nanoparticles. The porosity of the resulting mesoporous film can be controlled by changing the amount of polymer in the paste and it is ideally about 50-60% [7]. Higher porosity causes a decrease in charge collection efficiency due to the reduction in the interconnection between nanoparticles [16]. The usually employed architecture of high-efficient mesoporous TiO_2 electrode is the following [7]:

- (i) A TiO_2 blocking layer (thickness ~ 50 nm), coated on the conductive glass (*Figure 3.5*) to prevent contact between the redox mediator in the electrolyte and the FTO or ITO reducing charge carrier recombination with the oxidized form of the redox couple (OX). The thickness of this layer is such as to preserve photoanode transparency.
- (ii) A light absorption layer (thickness ~ 10 μm) consisting of mesoporous TiO_2 obtained by sintering of Titania nanoparticles (diam. 20 nm), which provides a large surface area for sensitizer absorption and good electron transport to the substrate.
- (iii) A light scattering layer (thickness ~ 3 μm) on top of the mesoporous film containing TiO_2 particles (diam. 400 nm) with the aim of increasing the average

optical path length of the light within the TiO₂ film through scattering resulting in an increased photocurrent produced.

- (iv) An ultrathin overcoating of pure TiO₂ (thickness ~ 1 nm) on the whole structure which can contain impurities or have carbon residues at the surface, deposited by means of chemical bath deposition (using aqueous TiCl₄), followed by heat treatment to obtain a sintered anatase-based layer. This last layer allows an increased dye adsorption due to the resulting increased roughness and it is responsible for a lowering of the acceptor levels in energy in the TiO₂ (more negative in value) which can improve the electron injection efficiency due to the smaller energy difference between the sensitizer LUMO and the CB of TiO₂ (*Figure 3.2*).

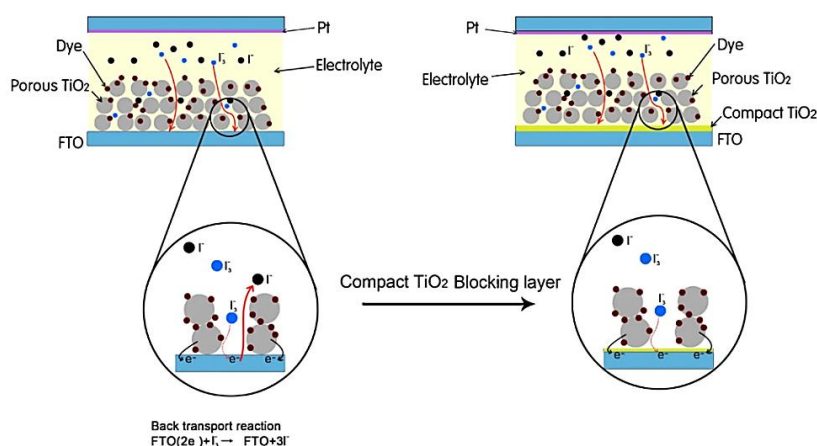


Figure 3.5. Schematic representation and mechanism of applying transparent TiO₂ efficient blocking layer to prevent the back-transport reaction of electrons [17].

3.3.1.2. ZnO

As reported in the first paragraph, ZnO was one of the first semiconductor used in DSSCs. It is very similar to TiO₂ Anatase considering valence and conductive bands (*Figure 3.4*) but having a higher electron mobility on respect of TiO₂, it should favour electron transport. The limitation on the use of this metal oxide derives from its poor chemical stability if compared with TiO₂, as it can be dissolved both in basic and acid conditions. On the contrary its relative ease of sintering in the highly crystalline form

(wurtzite structure) with different morphologies (nanoparticles, nanorods, nanotubes *etc.*) has recently led to an increased number of researches on ZnO [7] even if the reachable efficiencies are still low ($\eta \sim 5-5.5\%$)[18][19] if compared with TiO₂ based devices ($\eta > 10\%$)[20]. This is because the electron transport, which is enhanced in ZnO, is not however a limiting factor for DSSCs under operational conditions [20].

3.3.1.3. SnO₂

Tin oxide is a chemically stable compound that, as shown in *Figure 3.4*, has a conduction band edge about 0.5 eV lower than that of TiO₂ (anatase) and it is therefore used with dyes characterized by low-in-energy LUMOs which would cause a poorly electron injection efficiency in TiO₂, such as perylene sensitizers [7]. At the same time, however, the position of its CB limits the performances ($\eta \sim 2-2.4\%$ [21]) due to the low values of V_{OC} . By covering SnO₂ with another ultrathin metal oxide layer (i.e. ZnO, MgO or Al₂O₃) much improved voltage and efficiencies ($\eta \sim 5.5-6\%$ [21]) can be obtained [20].

3.3.2. Dyes

In a DSSC a dye sensitizer plays a very important role in generating the photo-induced electrons and injecting them into the conduction band of the TiO₂ semiconductor. The task of the dye is to harvest as many photons as possible and inject electron in the semiconductor. In other words, the power conversion efficiency η is strongly dependent on the sensitizer.

The reason why a DSSC is dye sensitized is because the band-gap of the semiconductor is so wide that it would only absorb light in the UV region. For TiO₂ (anatase), as shown in *Figure 3.4*, the band gap of 3.2 eV corresponds to an absorption threshold approximately below 400 nm. In this way a great deal of photons would be lost and efficiency would never be high under standard sun illumination. An ideal sensitizer for DSSCs should fulfil some essential characteristics [7][13][22]:

- (i) The absorption spectrum should cover the whole visible region and even the part of the near-infrared (NIR), *i.e.* below a threshold wavelength of ~ 920 nm

- (ii) It should have anchoring groups (-COOH, -H₂PO₃, -SO₃H) which allow a strong grafting onto the semiconductor surfaces
- (iii) Its excited state level (S*/S⁺) should be higher in energy than the conduction band edge of the semiconductor (for n-type DSSCs, *e.g.* TiO₂) so that an efficient electron transfer between the excited dye and the CB of the semiconductor can take place
- (iv) It should have a suitable redox potential that allows a rapid regeneration through the redox couple in the electrolyte, *i.e.* an oxidized state level (S⁺) more positive than the redox potential of the electrolyte
- (v) Unfavourable dye-dye aggregations (*i.e.* H and J aggregates) on the semiconductor surface should be avoided by an optimization of the molecular structure through the addition of coadsorbers, molecules that do not have a photoactive role in the process but that have the only role of preventing aggregations.
- (vi) The photosensitizer should be photostable; electrochemical and thermal stability are also required.

According to these criteria, efficient dye sensitizers can be simply classified, based on their chemical structure, under two major categories: metal-complexes dyes and metal-free organic dyes.

3.3.2.1. Metal Complexes

Metal complexes, and in particular Ru(II)-based complexes, have been employed and intensively investigated for DSSCs applications. They present several favourable properties such as broad absorption spectra, suitable energy levels, relative long excited-state lifetime and good electrochemical stability [7]. Their ability of light absorption in the visible part of the solar spectrum is due to Metal-to-Ligand Charge Transfer processes (MLCT) consisting in an electron transfer from a molecular orbital (MO) with metal-like character to those with ligand-like character which are common for ligand with low-lying π^* orbitals, *i.e.* extensive conjugation systems and aromatic ligands.

Two of the most commonly employed and efficient Ru(II)-based sensitizers are the so called **N719** – (*cis* – diisothiocyanato – bis (2 , 2' – bipyridyl -4 ,4'-) ruthenium (II) bis (tetrabutylammonium) – and **N749** – (triisothiocyanato-(2,2':6',6''-terpyridyl-4,4',4''-tricarboxylato) ruthenium (II)tris (tetra - butylammonium)) – also known as “Black Dye”. Because of their massive use for DSSCs application, these dyes, whose chemical structures are reported in *Figure 3.6*, are commercially available sensitizers.

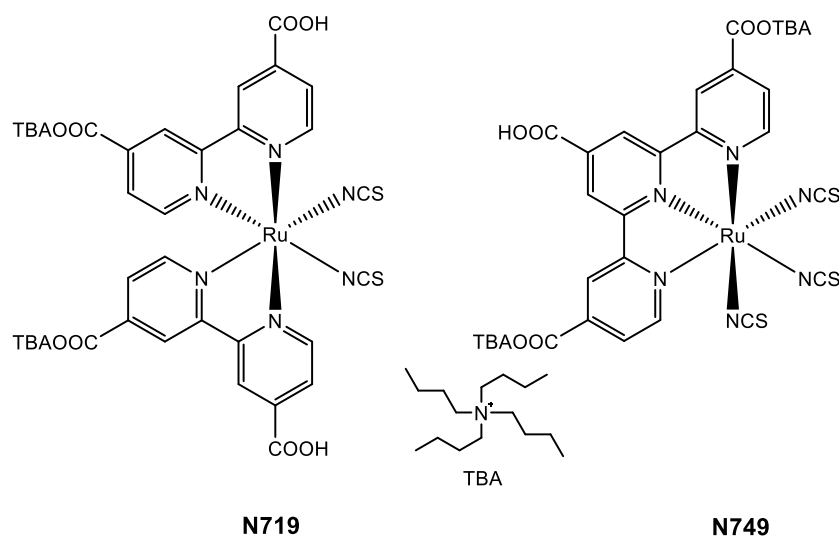


Figure 3.7. Chemical Structure of two most employed Ru(II)-based dye sensitizers.

Being based on metal-centred transition the central metal ion is therefore a crucial part of the overall properties of the complexes. On the other hand, though, that constitutes at the same times one of the mayor drawback of these classes of sensitizers. Ru is, in fact, not only a very expensive noble metal, but it is also very toxic. For this reason, research in the field of metal-based sensitizers has moved towards the use of organic-based ones, porphyrin-based dye [7][23], and inorganic lead perovskites [7][24]. Among them, the most efficient and sustainable sensitizers are based on organic molecules which are discussed below.

3.3.2.2. *Organic Dyes*

Fully organic sensitizers as an alternative to Ru(II)-based dyes offers in DSSC applications some potential advantages, first of all, the possibility of avoiding the use of

expensive and/or hazardous metals. Moreover, they can be easily synthesized in different structure which lead to the possibility of tuning the major optical properties. In addition, they usually exhibit higher molar extinction coefficient on respect of the metal-organic sensitizers, which makes them attractive for thin film and solid state DSSCs [7][22][25][26].

Organic sensitizers with visible light absorption commonly possess a donor- π -acceptor configuration (D- π -A) consisting with an electron donor and an electron acceptor which are linked covalently through a π conjugated bridges also referred as “spacer” [27]. Due to this basic arrangement it is easy to design new dyes structure, extend the absorption spectra, adjust the HOMO and LUMO levels and complete the intramolecular charge separation [7]. The set of thiazolo[5,4-*d*] thiazole-based sensitizers employed in this research work, whose chemical structure is reported below (*Figure 3.7*), is an example of D- π -A sensitizers.

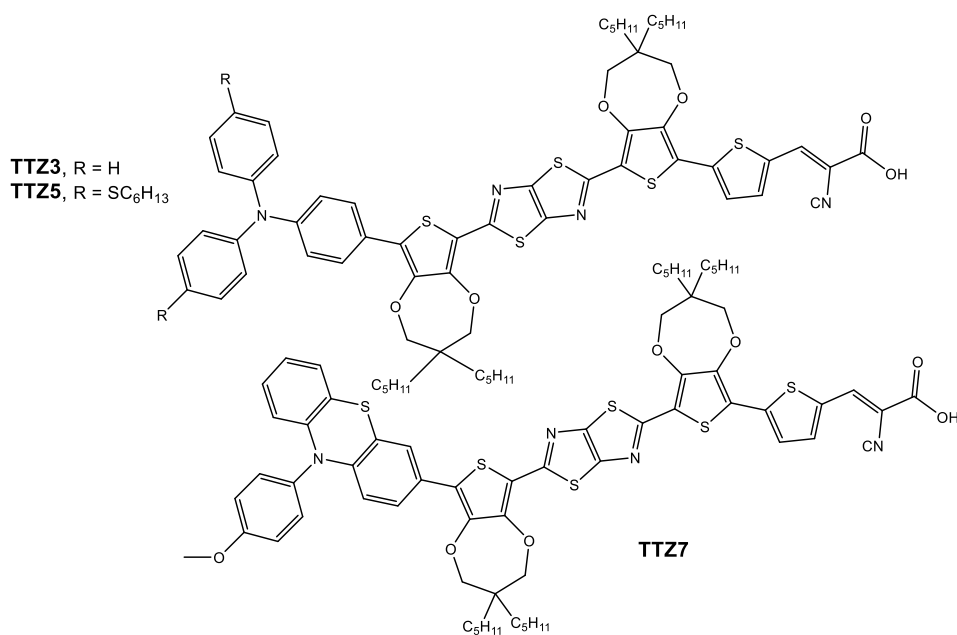


Figure 3.7. Chemical structure of the set of organic sensitizers employed in this research work.

When illuminated, the photo-induced electrons transport starting from the electron donor moiety, through the π -conjugated bridge till the electron acceptor moiety occurs, and electrons are thus injected in the TiO₂ network. Is important to underline that the π -linker is the key to influence both the HOMO and the LUMO [22]. The spacer influences the absorption of the dye which depends on the length, degree of conjugation and intrinsic

electron withdrawing or donating ability of the linker. Thus, the HOMO-LUMO gap of the sensitizers does depend on the HOMO of the donor and the LUMO of the acceptor but, on the same time, the linker unit affects, for what just stated, the gap of the whole molecules as well.

3.3.2.3. Anchoring of the dye on the oxide surface

There are generally different kinds of adsorption modes of the sensitizer molecules onto the oxide layer surface, namely covalent bonding, electrostatic interactions, hydrogen bonding, hydrophobic interactions, van der Waals forces, and physical entrapment inside pore or cavities [7]. The adsorption modes of dyes on semiconductor surfaces are very important for the whole device efficiency. The link of sensitizer needs, in fact, to be stable. It is therefore easy to understand why most of dyes have an anchoring group that can covalently react with the hydroxyl groups of the semiconductor oxide. Most often a carboxylic acid is used because of its easy synthesis and relative stability. It is the case of both the Ru(II) metal-organic dyes and the three fully organic dyes (TTZ3, TTZ5, TTZ7) employed in this work. This also explain why the ultrathin pure overcoating of TiO₂ is applied on top of the mesoporous layer. In this way, an enhanced number of -OH moieties is ensured.

The carboxylic acid group can coordinate to the TiO₂ surface in three ways [28], which are depicted in *figure 3.8*.

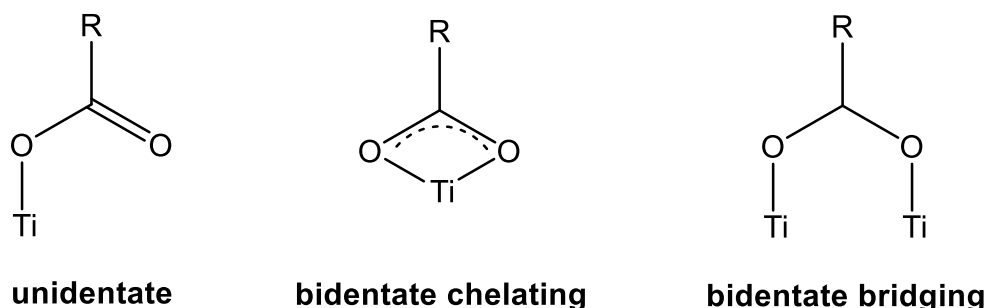


Figure 3.8. Different binding modes for carboxylic acid anchoring group on TiO₂ surface.

3.3.3. *Electrolyte*

Electrolyte is another key component in DSSCs. It is responsible for the inner charge carrier transport between electrodes, providing pure ionic conductivity, and for the continuous regeneration of the dye and itself.

Electrolytes have great influence on long-term stability of the cells and on the light-to-electric efficiency because they influence the main photovoltaic parameters which are involved in determining η , *i.e.* J_{sc} , FF, and V_{oc} [10].

Several aspects are essential for the electrolytes used in DSSCs:

- (i) They must be able to transport the charge carriers between photoanode and CE in order to rapidly regenerate the dye after electrons injection.
- (ii) They must guarantee a fast diffusion of charge carriers, *i.e.* high conductivity, and a good interfacial contact between electrodes.
- (iii) They must have long-term chemical, thermal, optical, electrochemical stability without causing desorption or degradation of the adsorbed dye.
- (iv) They should not exhibit a significant absorption in the range of adsorption of the dye which would lead to a reduced amount of light available for dye excitation.

A fundamental element of the electrolytes is the redox couple which, as stated before, is essential for the regeneration of the dye (reduction of S^+ to S and formation of the OX form of the redox couple) and for completing the electrochemical cycle of a DSSC, diffusing to the CE where it is reduced. In terms of energy level, to increase the photovoltage of the DSSC, it is critical to use a redox couple that has energy as close as possible to the S^+/S energy level of the dye but with sufficient driving force to regenerate the dye quantitatively.

That being said, the iodide/triiodide redox couple has a suitable redox potential and provides rapid dye regeneration and slow electron recombination. For these reasons and for its good solubility, high conductivity and favourable penetration in the TiO_2 porous structure, this couple has been the preferred redox mediator since the beginning of DSSCs development [7][10]. The iodide-base redox shuttle possesses, however, a

number of unfavourable characteristics [29] among which the absorption of good portion of visible light (300-450 nm) by the I_3^- , and its relative corrosion properties toward several material composing cells. For these reasons several alternative redox couple have been proposed in the last two decades to replace the iodine-based one, even if it still allows to obtain the best performances [7][10]. Among these cobalt complexes are particularly promising mediator alternatives for several reasons [30]. They are generally less coloured and therefore compete less with the dye in visible light absorption. Moreover, they are not corrosive to metal cathodes and non-volatile and they generally show more positive redox potential than I/I_3^- , therefore they are particularly interesting for maximizing the V_{OC} of DSSCs as show by *Figure 3.9*.

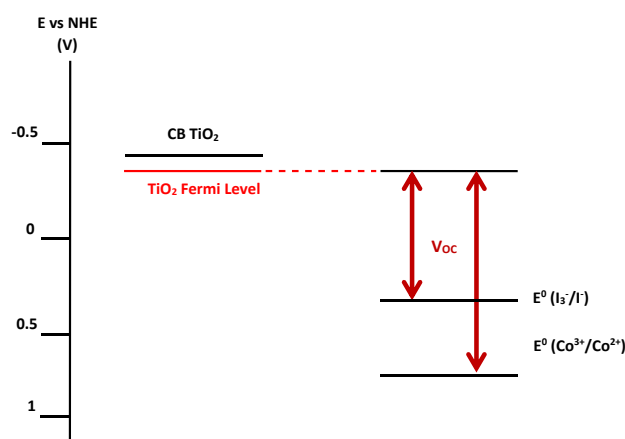


Figure 3.9. Schematic representation of the relative energy states and the implication on the cell V_{OC} for I_3^-/I^- and $[Co(bpy)_3]^{3+/2+}(PF_6)_{2/3}$.

On the basis of their physical state electrolytes are broadly classified in three main categories: liquid electrolyte, quasi-solid electrolyte and solid-state electrolyte [7][10]. Only the first two cases will be analysed because part of the thesis work.

3.3.3.1. Liquid redox electrolytes

The main aspects that liquid-state electrolyte need to satisfy are the chemical stability, the low viscosity in order to ensure an easy diffusion of species, and they should be a good solvent for the redox couple and for the various additives without causing at the same time the dissolution of the adsorbed dye or the material whose the semiconductor is composed. In addition to that, it should be compatible with sealing material in order to

avoid losses by evaporation or leakage [7]. The two options which simultaneously fulfil most of the above criteria are based on fairly polar organic solvent - such as organic carbonate or mixture of nitriles (ACN, MPN etc.), due to their higher boiling point - and ionic liquids. The latter have been studied because of the needed for organic solvents with long-term stability and low volatility. Being salts in a liquid state, ionic liquids can be considered as liquid electrolytes composed entirely of ions. They possess unique features such as chemical and thermal stability, tuneable viscosity, broad electrochemical potential window and, of course, high ionic conductivity [10].

3.3.3.2. *Quasi-solid electrolytes*

Under this name they are usually classified both gel and polymer electrolytes which can be obtained from liquid electrolyte by means of a gelling or polymerizing agent. This reduces some intrinsic practical issues related to the use of liquid systems such as leakage, volatilization of the solvent, and in particular, ineffective sealing of cells, which is mandatory for long-term application.

In this kind of electrolytes, the redox mediator is included in the semisolid system which can be considered as a supramolecular nanoaggregate arrangement characterized by a remarkable ionic conductivity. From the way they are obtained, charge transport does not occur through diffusion of molecules in quasi-solid state but by hopping of charge. For the reduced mobility of the redox component within the system, these electrolytes usually show conversion efficiency slightly lower than the host liquid redox electrolyte [7][10].

3.3.4. *Counter Electrode*

The counter electrode represents the last important component of a DSSC. The most employed system is composed by deposition of a thin catalytic layer of platinum onto a conductive glass substrate. Without Pt, conductive ITO or FTO, would be very poor counter electrodes with a very high charge transfer resistance ($>10^6 \Omega\text{cm}^2$) in a standard iodide/triiodide electrolyte [31]. The presence of Pt leads to a value of about $1 \Omega\text{cm}^2$ [7]. The high cost of Pt, however, has directed the research towards new catalytic systems since the beginning. In this direction good results have been obtained with carbon-based materials from simple mixture of graphite and carbon black to more complex carbon

nanotubes [7]. Alternatives to these systems are conductive polymers such as PEDOT (poly(3,4-ethylenedioxythiophene)) or CoS deposited onto flexible substrate like (ITO/PEN)[7].

References

- [1] H. Tributsch, "Reaction of Excited Chlorophyll Molecules at Electrodes and in Photosynthesis", *Photochem. Photobiol.*, 16, pp. 261-269, 1972.
- [2] H. Tsubumara, M. Matsumura, Y. Nomura, T. Amamiya "Dye Sensitized Zinc Oxide: aqueous electrolyte : platinum photocell", *Nature*, 261, pp. 402-403, 1976.
- [3] R. Memming, "Electron transfer process with excited molecules at semiconductor electrodes", *Prog. Surf. Sci.*, 17, pp. 7-74, 1984.
- [4] J. Desilvestro, M. Grätzel, L. Kavan, J. Moser, "Highly efficient sensitization of titanium dioxide", *J. Am. Chem. Soc.*, 107, pp. 2988-2990, 1985.
- [5] B. O'Regan, M. Grätzel, "A Low-Cost, High-Efficiency Solar Cell Based on Dye Sensitized Colloidal TiO₂ Films", *Nature*, 353, pp. 737-740, 1991.
- [6] D. Wei, G. Amaratunga, "Photoelectrochemical Cell and Its Applications in Optoelectronics", *Int. J. Electrochem. Sci.*, 2, pp. 897-912, 2007.
- [7] A. Hagfeldt, G. Boschloo, L. Sun, L. Kloo, H. Pettersson, "Dye-sensitized solar cells," *Chem. Rev.*, 110 pp. 6595-6663, 2010.
- [8] J. Gong, K. Sumathy, Q. Qiao, Z. Zhou, "Review on dye-sensitized solar cells (DSSCs): Advance techniques and research trends", *Renew. Sust. Energ. Rev.*, 68, pp. 234-246, 2017.
- [9] A. Hagfeldt, M. Grätzel, "Light-induced Redox Reaction in Nanocrystalline Systems", *Chem. Rev.*, 95, pp. 49-68, 1995.
- [10] J. Wu, Z. Lan, J. Lin, M. Huang, Y. Huang, L. Fan, G. Luo, "Electrolytes in Dye-Sensitized Solar Cells", *Chem. Rev.*, 115, pp. 2136-2173, 2015.
- [11] D. Cahen, G. Hodes, M. Grätzel, J. F. Guillemoles, I. Riess, "Nature of photovoltaic action in dye-sensitized solar cells", *J. Phys. Chem. B*, 104 (9), pp. 2053-2059, 2000.

- [12] M. Grätzel, "Solar Energy Conversion by Dye-Sensitized Photovoltaic Cells", *Inorg. Chem.*, 44, pp. 6841-6851, 2005.
- [13] M. Grätzel, "Photoelectrochemical Cells", *Nature*, 414, pp. 338-344, 2001.
- [14] Y. Xiao, J. Wu, G. Yue, G. Xie, J. Lin, M. Huang "The preparation of titania nanotubes and its application in flexible dye-sensitized solar cells ", *Electrochim. Acta*, 55, pp. 4573-4578, 2010.
- [15] N. Bwana, "Comparison of the performances of dye-sensitized solar cells based on different TiO₂ electrode nanostructures", *J. Nanoparts. Res.*, 11, pp.1917-1923, 2009.
- [16] K. D. Benkstein, N. Kopidakis, J. van de Lagemaat, A. J. Frank, "Influence of the Percolation Network Geometry on Electron Transport in Dye-Sensitized Titanium Dioxide Solar Cells", *J. Phys. Chem. B*, 107, (31), pp. 7759-7767, 2003.
- [17] D. Qian, Y. Li, q. Zhang, Q. Shi, G. Wang, "Anatase TiO₂ sols derived from peroxotitanium acid and to form transparent TiO₂ compact film for dye-sensitized solar cells", *J. Alloys Compd.*, 509, pp. 10121-10126, 2001.
- [18] R. Vittal, K.-C. Ho, "Zinc Oxide based dye-sensitized solar cells: A review", *Renew. Sust. Energ. Rev.*, 70, pp. 920-936, 2017
- [19] M. U. Rahman, M. Wei, F. Xie, M. Khan, "Efficient Dye-Sensitized Solar Cells Composed of Nanostructural ZnO Doped with Ti", *Catalysts*, 9, 273:1-11, 2019.
- [20] G. Boschloo, "Improving the Performance of Dye-Sensitized Solar Cells", *Front. Chem.*, 7 (77), 2019.
- [21] S. N. F. Zainudin, H. Abdullah, M. Markom, "Electrochemical Studies of tin oxide based-dye-sensitized solar cells (DSSC): a review", *J Mater Sci: Mater Electron*, 30, pp 5342-5356, 2019.
- [22] C.-P. Lee, C-Ting Li, K-C. Ho, "Use of organic materials in dye-sensitized solar cells", *Mater. Today*, 20, pp. 267-283, 2017.
- [23] L.-L. Li, E. W.-G. Diau, "Porphyrin-sensitized solar cells" *Chem. Soc. Rev.*, 42, pp. 291-304, 2013.

- [24] S. Kazim, M. K. Nazeeruddin, M. Grätzel, s. Ahmad, “Perovskite as light harvester: a game changer in photovoltaics”, *Angew. Chem., Int. Ed.*, 53, pp. 2812-2825, 2014.
- [25] A. Dessì, M. Calamante, A. Mordini, M. Peruzzini, A. Sincropi, R. Basosi, F. Fabrizi de Biani, M. Taddei, D. Colonna, A. di Carlo, G. Reginato, L. Zani, “Thiazolo[5,4-d]thiazole-based organic sensitizers with strong visible light absorption for transparent, efficient and stable dye-sensitized solar cells,” *RSC Adv.*, vol. 5, no. 41, pp. 32657–32668, 2015.
- [26] A. Dessì *et al.*, “Organic dyes with intense light absorption especially suitable for application in thin-layer dye-sensitized solar cells,” *Chem. Commun.*, vol. 50, no. 90, pp. 13952–13955, 2014.
- [27] Y. -S. Yen, H.-Chou, Y.-C. Chen, C.-Y. Hsu, J. T. Lin, “Recent Developments in molecule-based organic materials for dye-sensitized solar cells”, *J. Mater. Chem.*, 22, pp. 8734-8747, 2012.
- [28] Z. S. Wanf, K. Hara, Y. Dan-Oh, C. Kasada, A. Shinpo, S. Suga, H. Arakawa, H. Sugihara, “Photophysical and (Photo)electrochemical Properties of a Coumarin Dye” *J. Phys. Chem. B.*,109, pp. 3907-3914, 2005.
- [29] J. Cong, X. Yang, L. Kloo, L.Sun, “Iodine/Iodide-Free Redox Shuttles for Liquid Electrolyte-Based Dye-Sensitized Solar Cells”, *Energy Environ. Sci*, 5, pp. 9180-9194, 2012.
- [30] L. Garibabu, R. Bolligarla, M. Panigrahi, “Recent Advances of Cobalt(II/III) Redox Couples for Dye-Sensitized Solar Cell Applications”, *Chem. Rec*, 15, pp. 760-788, 2015.
- [31] A. Hauch, A. Georg, “Diffusion in the electrolyte and charge-transfer reaction at the platinum electrode in dye-sensitized solar cells”, *Electrochim. Acta*, 46, pp. 3457-3466, 2001.

Chapter 4. Fibre-Shaped Dye-sensitized Solar Cells

4.1. Introduction to Fibre-Shaped Dye-Sensitized Solar Cells

As reported in *Chapter 3*, an advantage of dye-sensitized solar cells strictly correlated to their structure is the possibility to be fabricated with flexible and stretchable substrates making them flexible, deformable and light weighted. Before 2001 DSSCs were fabricated in a planar configuration to meet demands for home, energy or industrial supply. It was in fact after a decade from the breakthrough work of Grätzel and O'regan [1] that the conception of fibre-shaped dye-sensitized solar cells (FDSSCs) called “solar cells in fibre form” took place. The structure consisted in a stainless steel covered with a layer of dye-adsorbed TiO₂ particles and a transparent conductive polymer, as counter electrode, wrapped outside in a coaxial set-up [2] (*Figure 4.1*). However, because of the low conductivity of the polymer electrode, only several microamperes were detected. Nevertheless, the proposed conception paved the way for the application of FDSSCs pertaining to wearable electronic devices and inspiring the research world to the development of efficient component fibre electrodes.

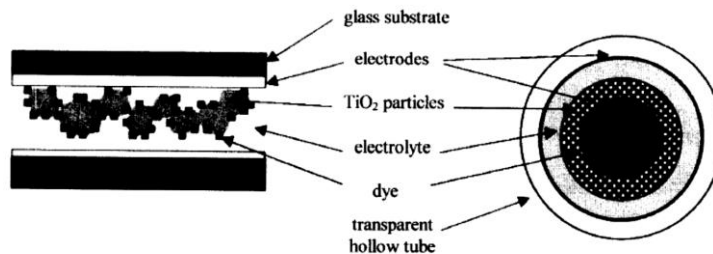


Figure 4.1. Arrangement of a flat solar cell (left) used for testing components and the FDSSC (right) first present in literature [2].

Nowadays, portable electronics have been attracting increasing attention. They are suitable for message, communication, signal transport, health monitoring, medical care, *etc* [3]. Because of this great importance given to wearable and portable electronics, such as Google glasses, iWatches, and smart phones, there is the necessity to deepen the wearable concept and meet future individual needs incorporating flexible optoelectronic devices into clothing, backpacks, and other belongings, for the so-called spreading of

smart products, namely “electronic textiles”, or “e-textiles”[4]. In this view, fibre-shaped dye-sensitized solar cell, exploiting solar-to-electric conversion and being fabricated on fibre substrates, can represent suitable units in e-textile as wearable renewable power sources for self-powered smart systems. Their ability of working in diffuse light conditions, which allows them to attain good performances also with low light intensity, makes them great candidates for this purpose.

4.2. *FDSSC structures*

Even though the functioning of DSSCs in fibre-shaped is exactly the same as for planar devices, unlike common DSSCs which are fabricated only in the sandwich-like architecture, fibre-shaped DSSCs allow the assembly of the devices in various arrangements. All these architectures share their ability of harvesting solar radiation in 3D space, giving more freedom with respect to planar devices [4]. In this section, the main configurations for FDSSCs present in literature along with some examples to be cited are reported.

4.2.1. *Twisting structured FDSSCs*

After the first tentative idea in 2001, which extended the typical sandwich structure of a planar DSSC to FDSSCs, and which require the use of an external transparent polymer sheath as counter electrode to allow light to pass through, in 2008 a flexible wire-like DSSC was reported in literature, which was based on a double twisted metal fibres as electrodes (*Figure 4.2*)[5].

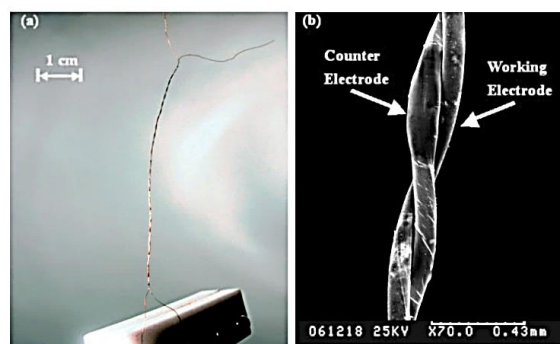


Figure 4.2. Optical photo (a) and SEM image (b) of the double twisted FDSSC using Pt wire as counter electrode and stainless-steel fibre coating with a layer of dye-sensitized porous TiO₂ [5].

In a double-twisted configuration, the two electrodes are twisted together and placed in a sealing apparatus such as a plastic tube. This design, which featured a linear shape TCO-free structure, was easy to fabricate and attracted wide attention because of the possibility of using opaque simple fibre-shape conductive material as electrodes (both photoanode and CE) such as high conductive metal wire or carbon-base fibres. Moreover, because of the symmetrical twisting, cell illumination state remains the same in any direction normalized to the twisting axis [5]. However, the main drawback of such structure is represented by the twisting process itself. During the twisting process, in fact, high local pressure is easily produced between electrodes due to stress concentration on certain parts. In these local parts, the carriers back-transfer rate increases, which results in the reduction of voltage and current.

Later on, a singly twisted FDSSC was developed (*Figure 4.3*) [6], where the counter electrode, still a Pt wire, was wound around the fibre photoanode made of dye-sensitized layer of TiO_2 coating a Ti wire, and packed in a capillary achieving efficiency up to 7%.

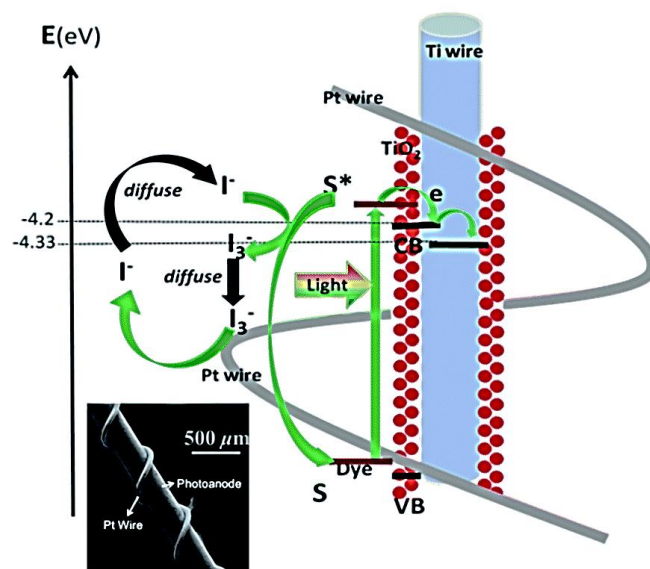


Figure 4.3. Schematic representation with working principle and SEM image of the singly twisted FDSSC developed in [6] where the Pt counter electrode is wound around the fibre photoanode [4].

As in double-twisted architecture, this set-up was demonstrated 3D light harvesting capacity due to its cylindrical-like and symmetrical structure, which meant that diffuse light from all directions, even at backside, could be capture.

4.2.2. Coaxial structured FDSSCs

Coaxial FDSSCs deriving from an evolution of the first fabricated fibre-shaped DSSC [2], present one electrode which externally coats or wraps another electrode as a multi-layered core-sheath structure. This architecture is inspired from the common DSSC in planar shape. If we unzip such a cell along its axis, a planar sandwich-typed dye-sensitized solar cell would be presented.

Contrarily to the twisted set-up, coaxial FDSSC emerged considering that, upon deformation, the two electrodes twisted together readily slip out. In twisted architecture, the counter electrode is not densely intertwined around the working electrode, because some dye molecules would be shielded from light by the opaque fibers. As a result, the diffusion of triiodide ions to the counter electrode is delayed by the increased distance, and the electrons accumulated at the counter electrode are not timely captured by triiodide ions [7]. Coaxial FDSSCs are exempt from that concern because the counter electrode is thoroughly and intimately contacted with electrolyte, enhancing the redox reaction at the electrode. An example of a coaxial FDSSC is reported in *Figure 4.4* [8], where a free-standing CNT film is wrapped around a TiO₂-modified Ti wire, recording an η of 1.65%.

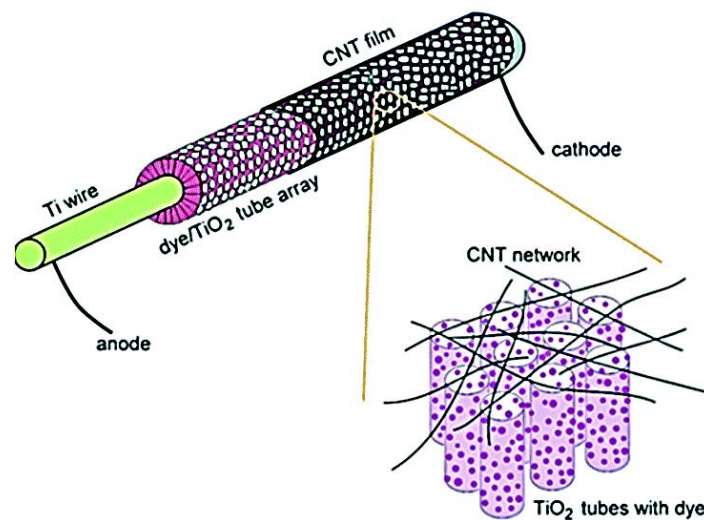


Figure 4.4. Flexible single-wire FDSSC obtained by wrapping carbon nanotube film around Ti wire-supported TiO₂ tube arrays as the transparent electrode [8]

In this example the thickness of the used nanotube film was 20-40 nm making it 80-85% transparent in the visible range.

4.2.3. Parallel structured FDSSCs

The last architecture that needs to be accounted, which has been adopted in this thesis, is the one that can be considered a direct translation of a planar DSSC into a fibre, as shown in *figure 4.5*, but using a plastic tube as storage unit instead of the two glass substrates.

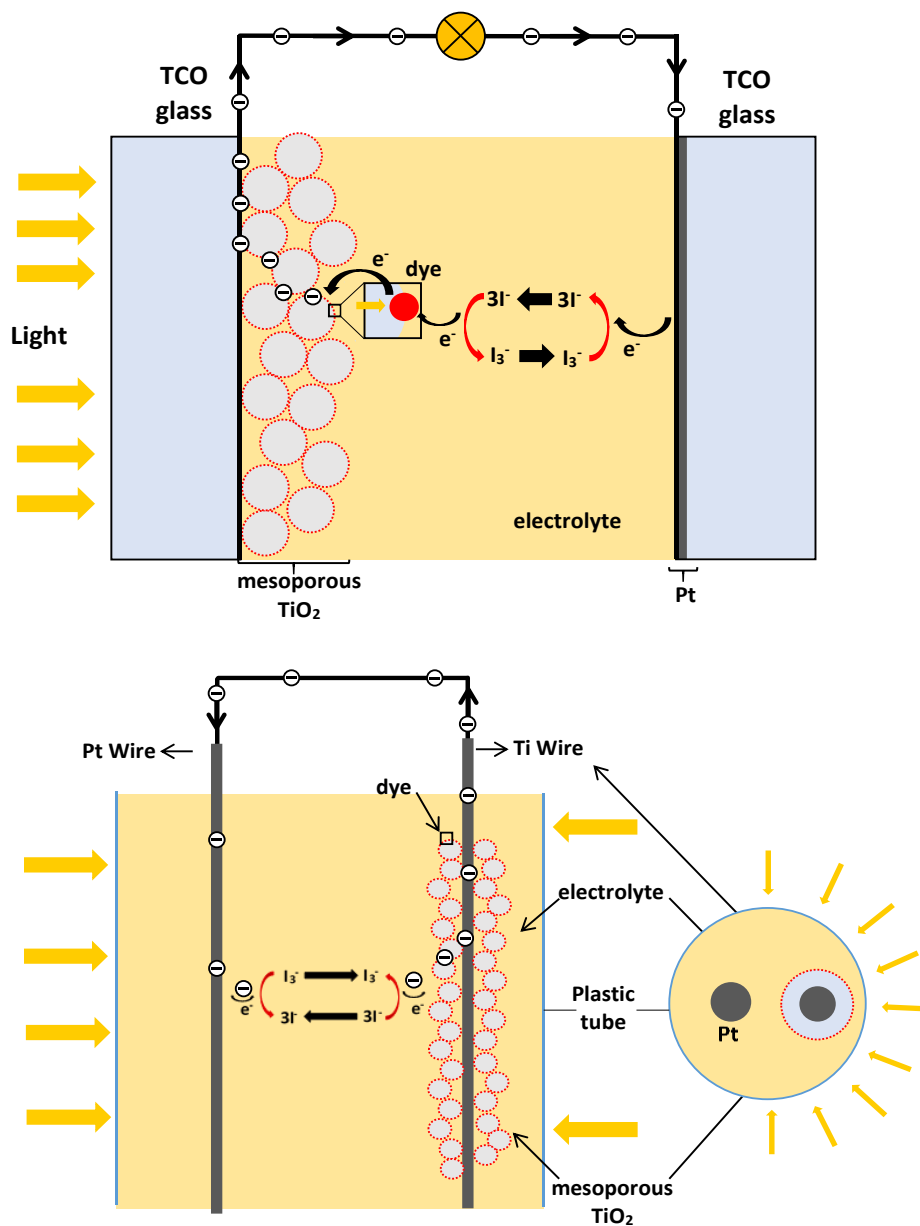


Figure 4.5. Analogy between a planar DSSC and the parallel configuration of the FDSS used in the experimental part of this thesis.

In parallel FDSSCs, in fact, the two wire-shaped electrodes face each other and are separated by a film of electrolyte. An example is the FDSSC reported in *Figure 4.6* [9].

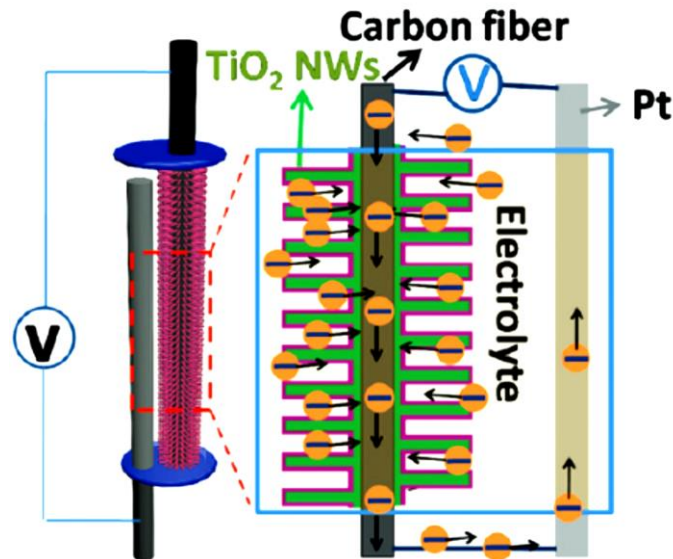


Figure 4.6. Schematic representation of the parallel configuration of the CF/TiO₂ NR array-based tube-shaped 3D FDSSC [9].

In this example a bunched Rutile TiO₂ nanorod (NR) arrays grown on carbon fibre (CF) was used as photoanode with Pt wire as counter electrode obtaining a η of 1.28 %.

4.3. FDSSCs performances

Since their discovery seventeen years ago, fibre-shaped dye-sensitized solar cells have evolved dramatically. From efficiency inferior to 0.5% is now possible to achieve light-to-electric conversion efficiency higher than 9%, up to 10 % thanks to complex architecture and advanced materials (*e.g.* hydrophobic aligned carbon nanotube core-based electrode) [4][13]. From the point of view of energy conversion efficiency, the best performance reachable with DSSCs in fibre form is still lower on respect of the planar dye-sensitized solar cells, whose best efficiency of 22.1% has been obtained with advanced perovskite cells [15]. With respect to other type of solar cells in fibre shaped

however, as shown in *Figure 4.7* [3], the performances of FDSSCs are in line with the best fibre-shaped PV cells.

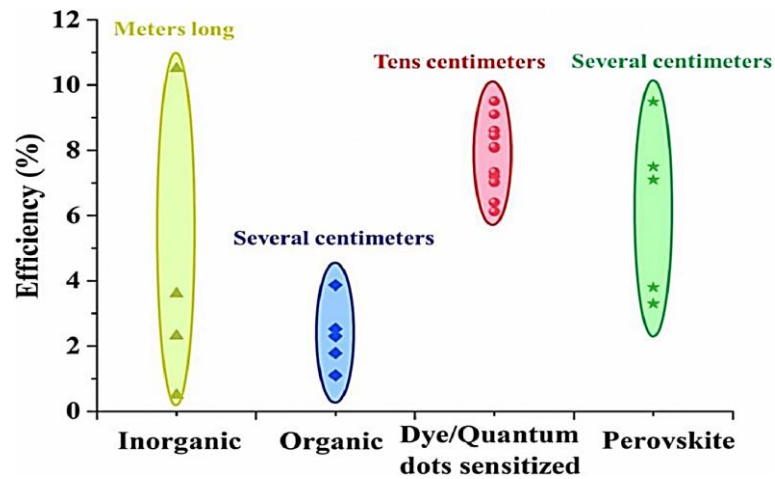


Figure 4.7. Efficiency and size distribution of different photovoltaic fibers (2018) [3].

As it appears from the image, length is an important factor when efficiency of fibre solar cells is taken into account. During the production process of the fibre, defects, layer fractures and film perforation can occur. These problems become more pronounced in longer devices, and this is the reason why device size needs to be emphasized in energy conversion efficiency comparisons.

4.4. Properties deriving from fibre shape

Evolved from the sandwich-type structure, the 3D structure proper of fibre-shaped dye-sensitized solar cells endows these devices with special features in light harvesting and charge transport, namely, for starting, the possibility of harvesting light in 3D space with respect to the only frontal collection of photons proper of planar DSSC. Experiments have shown constant performances with different incident angles [5-6] and therefore a simple diffusion plate such as rough substrates, white paper or a mirror collocated under the FDSSC can improve light harvesting and lead to higher power output via light scattering and reflection (*Figure 4.8*) [4],[6].

In addition, for fibre devices, the contact between the electrolyte and the sealing material is at two ends of the tubular structure whereby the electrodes are inserted, and thus, smaller than in planar devices, reducing the leakage rate when liquid electrolytes are used.

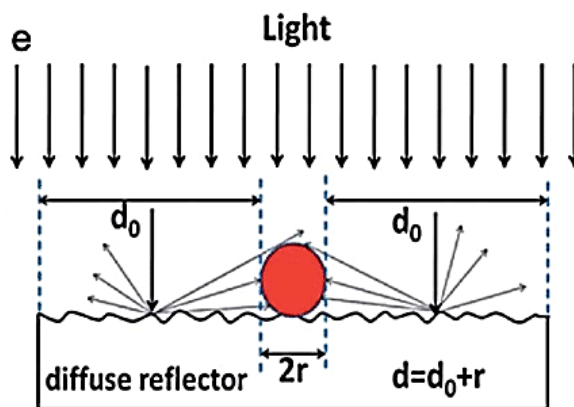


Figure 4.8. Schematic refiguration of the diffuse reflection illumination mode [6].

4.5. Substrates for FDSSCs

Substrates provide support to the whole device and they need to show mechanical strength, conductivity and high specific surface area. Considering that the application of such devices is correlated to their flexibility, the aspect ratio needs to be considered: smaller diameter and larger length would be ideal candidates for practical application [4]. For the same reason their weight should be as low as possible, and along with it, the cost. So far, the main substrates applied to FDSSCs have been metal fibres, carbon-based fibres, polymer fibres, and optical fibers.

4.5.1. Metal fibres

Metals fibre are the most commonly used due to their good conductivity, mechanical properties, long-range flexibility and high-temperature tolerance. Among them, titanium, stainless steel, tungsten, aluminium, nickel and zinc have been used. Most of the reported FDSSCs and in general the most efficient devices (7-9 %) are however fabricated with Ti-based photoanodes [4].

4.5.2. Carbon-based fibres

Carbon-based fibers are suitable substrates for FDSSCs counter electrodes because of their flexibility, low weight, high surface area, good conductivity, anti-corrosion property, and high mechanical properties. Some examples that have been used in FDSSCs are carbon fibres, which are composed by micron-size single fibre and which are commercially available, and carbon nanotubes (CNTs) made into continuous fibres, which possess even higher specific surface area [4]

Benefiting from the convenience of physical and/or chemical modifications, which bring more concepts for device design, carbon-based counter electrodes that have been used with satisfactory results are core-shell CNT/reduced graphene oxide (RGO) nanoribbon, CNT/RGO composite and RGO fibers [16].

A big challenge for FDSSCs is the fabrication of all carbon-based devices which employed carbon-based fibers as substrates for both electrodes. Some examples are present in literature (efficiency of 1.9 %) [17].

4.5.3. Polymer fibres

Polymer fibers are flexible, lightweight, low-cost and commercially available but not naturally conductive, so the main challenge in the use of such type of substrates in FDSSCs is to prepare conductive fibers. So far the main polymeric fibers that have been adopted showing interesting results are PEDOT:PSS (as counter electrode), PET, PP, PBT, and polyamide as photoanode substrates. Being polymers widely used for cloths, polymer fibre-based energy devices may play a role in wearable electronics [4].

4.5.4. Optical fibres

Optical fibers are used because of their internal light reflection which expanded the opportunities for solar energy conversion. By integrating them with a cylindrical counter electrode an impressive efficiency of up to 6% has been reached. In this case, TiO₂ nanowire arrays were grown on the optical fibre using liquid phase deposition method

and platinum was coated on the wall of the stainless-steel capillary using electroless deposition [18].

Given the special light harvesting characteristic induced by the modified optical fibers, the direction of the light reflected to the sensitized layer and photoelectron guided to the current-collecting electrode is similar to the case of traditional planar DSSCs, while ITO is involved as the transparent conductive layer. Moreover, the counter electrode can contribute to additional light reflection especially in closed structures. Theoretical investigations have shown in fact, that DSSCs wrapped around an optical fibre can achieve as promising performance as standard geometry [18].

References

- [1] B. O'Regan, M. Grätzel, "A Low-Cost, High-Efficiency Solar Cell Based on Dye Sensitized Colloidal TiO₂ Films", *Nature*, 353, pp. 737-740, 1991.
- [2] B. Baps, M. Eber-Koyuncu, M. Koyuncu, "Ceramic based solar cells in fiber form", *Key Eng. Mater.*, 206, pp. 937-940, 2001.
- [3] M. Peng, B. Dong, D. Zou, "Three dimensional photovoltaic fibers for wearable energy harvesting and conversion", *J. Energy Chem.*, 27, pp. 611-621.
- [4] M. Peng, D. Zou, "Flexible fiber/wire-shaped solar cells in progress: properties, materials, and design", *J. Mater. Chem, A.*, 3, pp. 20435-20458, 2015.
- [5] X. Fan, Z. Z. Chu, F. Z. Wang, C. Zhang, L. Chen, Y. W. Tang and D. C. Zou, "Wire-Shaped Flexible Dye-Sensitized Solar Cells", *Adv. Mater.*, 20, pp. 592–595, 2008.
- [6] Y. P. Fu, Z. B. Lv, S. C. Hou, H. W. Wu, D. Wang, C. Zhang, Z. Z. Chu, X. Cai, X. Fan, Z. L. Wang and D. C. Zou, "Conjunction of fiber solar cells with groovy micro-reflectors as highly efficient energy harvesters Energy", *Environ. Sci.*, 4, pp. 3379–3383. 2011
- [7] H. Peng, "Fiber-Shaped Dye-Sensitized Solar Cell" in *Fiber-Shaped Energy Harvesting and Storage Devices, Nanostructure Science and Technology (Springer)*, pp. 39-76, 2015.
- [8] S. Zhang, C. Y. Ji, Z. Q. Bian, R. H. Liu, X. Y. Xia, D. Q. Yun, L. H. Zhang, C. H. Huang and A. Y. Cao, "Single-wire dye-sensitized solar cells wrapped by carbon nanotube film electrodes", *Nano Lett.*, 11, pp. 3383–3387, 2011.
- [9] W. Guo, C. Xu, X. Wang, S. Wang, C. Pan, C. Lin, Z. L. Wang, "Rectangular Bunched Rutile TiO₂ Nanorod Arrays Grown on Carbon Fiber for Dye-Sensitized Solar Cells", *J. Am. Chem. Soc.*, 134, pp. 4437-4441, 2012.

- [10] J. Yan, M. Jasim, T. J. Dickens, D. E. Daramola, O. I. Okoli, “3D Wire-Shaped Dye-Sensitized Solar Cells in Solid State Using Carbon Nanotube Yarns with Hybrid Photovoltaic Structure”, *Adv. Mater. Interfaces*, 1,1400075-140081, 2014.
- [11] W. Guo, C. Xu, G. Zhu, C. Pan, C. Lin, Z. L. Wang, “Optical-fiber/TiO₂-nanowire-arrays hybrid structures with tubular counterelectrode for dye-sensitized solar cell”, *Nano Energy*, 1, pp. 176-182, 2012.
- [12] G. Kapil, S. S. Pandey, Y. Ogomi, T. Ma, S. Hayase, “Titanium wire engineering and its effect on the performance of coil type cylindrical dye sensitized solar cells”, *Org. Electr.*, pp. 3399-3405, 2014.
- [13] X. Fu, H. Sun, S. Xie, J. Zhang, Z. Pan, M. Liao, L. Xu, Z. Li, B. Wang, X. Sun, H. Peng, “A fiber-shaped solar cell showing a record power conversion efficiency of 10%”, *J. Mater. Chem. A.*, 6, 45-51, 2018.
- [14] G. Liu, M. Peng, W. Song, H. Wang, D. Zou, “An 8.07% efficient fiber dye-sensitized solar cell based on a TiO₂ micron-core array and multilayer structure photoanode”, *Nano Energy*, 11, pp. 341-347, 2015.
- [15] W.S. Yang, B.-W. Park, E.H. Jung, N.J. Jeon, Y.C. Kim, D. U. Lee, S.S. Shin, J. Seo, E. K. Kim, J. H. Noh, S. I. Seok, “Iodide management in formamidinium-lead-halide-based perovskite layers for efficient solar cells”, *Science*, 356, pp. 1376-1379, 356.
- [16] S. Pan, Z. Yang, P. Chen, X. Fang, G. Guan, Z. Zhang, J. Deng, H. Peng, “Carbon nanostructured Fibers As counter electrodes in Wire-shaped Dye-Sensitized Solar Cells” *J. Phys. Chem. C*, 118, pp. 16419–16425, 2014.
- [17] X. Cai, S. Hou, H. Wu, Z. Lv, Y. Fu, D. Wang, C. Zhang, H. Kafafy, Z. Chu, D. Zou, “All-carbon electrode-based fiber-shaped dye-sensitized solar cells”, *Phys. Chem. Chem. Phys.*, 14, pp. 125-130, 2012.
- [18] W. Guo, C. Xu, G. Zhu, C. Pan, C. Lin, Z. L. Wang, “Optical-fiber/TiO₂-nanowire-arrays hybrid structures with tubular counterelectrode for dye-sensitized solar cell”, *Nano Energy*, 1, pp. 176–182. 2012.

Chapter 5. Experimental Section

5.1. *Introduction*

The fabrication of an effective dye sensitized solar cell system involves several steps that are crucial to realize an high efficient device. In this thesis, optimized FDSSCs have been developed by studying and fine tuning the various components of the cell architecture, in particular dye molecule, photoanode oxide layer thickness, electrolytic system, cell length and electrodes substrates.

Different characterization techniques have been employed to better understand and improve the numerous elements and aspects concerning FDSSCs performances:

- Scanning Electron Microscopy
- Cyclic Voltammetry
- UV-Vis Spectroscopy
- Current-Voltage Measurements
- Electrochemical Impedance Spectroscopy

The last two analysis implied the use of a solar simulation for the testing of the devices in operating conditions.

5.2. *Photoanodes*

5.2.1. *Titanium-based Photoanodes*

Commercially available titanium wire (diam. 0.25 mm, 99.7 % trace metals basis, Sigma-Aldrich) were used as conductive substrates.

5.2.1.1. *Cleaning process of Ti-wire substrates*

After being cut, substrates were sonicated 5 min respectively in isopropanol, acetone, and ethanol in order to remove any trace of impurities from the surface which could affect the integrity of the blocking layer [1].

5.2.1.2. TiO_2 blocking layer

The fabrication of the compact TiO_2 layer able to act as blocking layer was obtained by simple oxidation of titanium wires via annealing in air at 450 °C [2]. After the cleaning process the samples were thus placed in a muffle furnace and subjected to the heating program indicated in *Table 5.1* (*Figure 5.1*), starting from room temperature.

Table 5.1. Annealing profile of Ti wires used in the formation of the TiO_2 blocking layer.

Temperature [°C]	Residence time [min]	Temperature Rise Rate [°C/min]
325	5	120
375	5	120
450	30	120

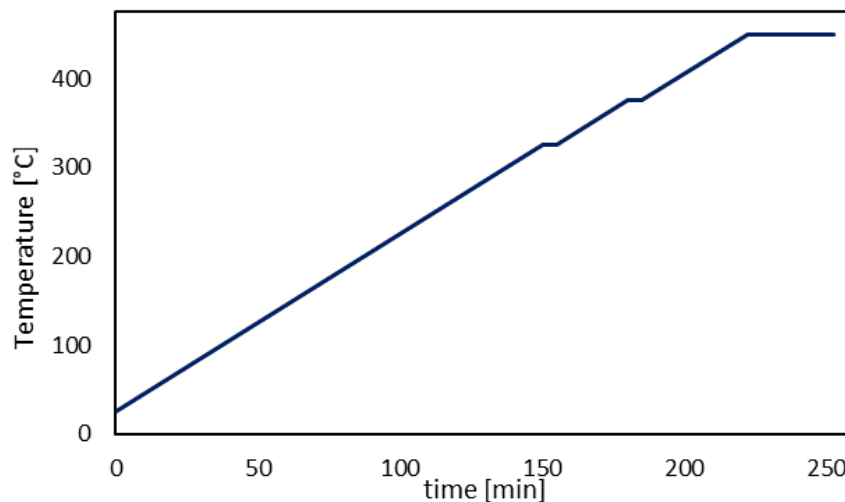


Figure 5.1. Refiguration of the heating program applied.

After the treatment, silver-shining Ti wires turned to a yellow colour (*Figure 5.2*), indicating the formation of the dense thin TiO_2 film. As suggested by literature [3], the yellow colour is originated by anatase lattice imperfections such as impurities deriving from titanium substrates or oxygen vacancies resulting from the annealing process.



Figure 5.2. Ti wire before (a) and after (b) the heat treatment employed for the formation of the TiO₂ blocking layer.

5.2.1.3. Deposition of the TiO₂ absorption layer by dip-coating

The TiO₂ mesoporous light absorption layer was obtained using a 1:1 wt% mixture of terpeneol (Sigma Aldrich) and a commercially available TiO₂ paste (Dyesol - DSL-18NR-T, average nanoparticles size: 20 nm) as ink for the dip-coating process, according to a previous process optimization. Each wire was coated for 3,5 cm or 10 cm of their length, at a constant speed of immersion/withdrawing of 3,75 m/s by using a semiautomatic dip-coater (Figure 5.3).

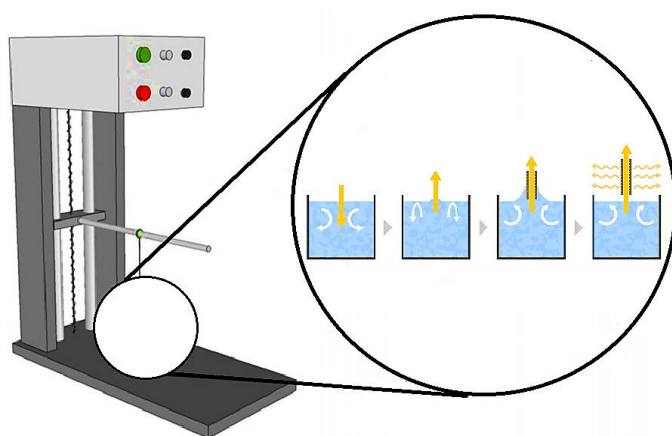


Figure 5.3. Schematic representation of the dip-coating process employed for the deposition of the mesoporous TiO₂ absorption layer.

Samples were then placed in an IR oven (20 min at 80°C, heating rate: 5°C/min) to obtain a uniform heating and consolidate the deposited Titania. The process was repeated as many times as necessary in order to obtain the desired thickness (*i.e.* number of deposition desired). Finally, the films were sintered in air in a muffle furnace to remove organic compound and create electrical connection between the nanoparticles following the heating program previously reported (*Table 5.1 – Figure 5.1*).

5.2.1.4. Deposition of the pure TiO₂ ultrathin overcoating

As reported in *chapter 3*, the ultrathin compact layer of TiO₂ can be obtain by hydrolysis of a TiCl₄ solution [4] of concentration of 40-50 mmol/L. The titania layer is the result of a chemical bath deposition, and the following reaction:



5.2.1.4.1. Preparation of the TiCl₄ solution

At first a concentrated stock solution of aqueous 2.0 mol/L TiCl₄ from pure TiCl₄ (≥ 99%, Fluka Analytical) was made using precooled milli-q water and an ice bath. TiCl₄ reacts, in fact, with water in an exothermic reaction, heating up the solution while making and oxidizing, even at room temperature, into TiO₂. Each preparation was carried out without using any form of metallic labware that could potentially lead to a contamination of the solution with a consequently modification of the electronic properties of the deposited TiO₂ compact layer [5]. 6 mL of precursor were added to 27,4 mL of water in two separate aliquots. First pure TiCl₄ was added drop by drop to 17,4 mL of solvent kept under vigorous stirring in an ice bath, while the remaining 10 mL of water were added at the end of the process. This procedure allowed to keep under control the temperature of the solution. Stock solutions were stored in PE bottles at 4°C to avoid any form of decomposition. Fresh diluted solution of 48 mmol/L were prepared before each TiCl₄ treatment by adding 1 mL of the stock solution to 40 mL of milli-q water.

5.2.1.4.2. $TiCl_4$ treatment

The chemical bath deposition was performed by dipping the substrates in the solution at 70°C for 30 min in a close container to avoid the evaporation of water and the consequent change in concentration. After the treatment, each fibre was washed with absolute anhydrous EtOH (Carlo Erba Reagents) to remove any trace of the solution, dried and annealed following the same heat treatment previously performed (*Table 5.1 – Figure 5.1*).

5.2.2. Kevlar-PPy coated-based photoanodes

Kevlar conductive fibres by means of a coating of PPy prepared by chemical reactions (provided by CNR-STIIMA) were tested as carbon-based substrate for photoanodes. These Kevlar fibers are based on 7.6% PPy and linear resistance equal to 0.57 K Ω /cm. When Kevlar-PPy coated fibres were used, no blocking layer was applied. The TiO₂ mesoporous layers was obtained by dip-coating following the same procedure reported in *section 5.2.1.3*, but with a different consolidation of the layer at the end of the procedure. The annealing process was indeed performed, because of the carbonaceous composition of the substrate, in an IR oven at lower temperature (3 hours, 180 °C, temperature rise rate: 120 °C/h). The same heating program was performed after the deposition of the ultrathin pure TiO₂ *via* chemical bath deposition, which followed the same standard procedure adopted for Ti-wire based photoanodes (*section 5.2.1.4*).

5.3. Sensitization of photoanodes

0.2 mM dye solutions to be adsorbed on the photoanodes TiO₂ films were prepared in absolute anhydrous EtOH (Carlo Erba Reagents) for the Ru-based sensitizers **N719** (Solaronix), and **N749** (Sigma Aldrich) and in THF ($\geq 99.9\%$, Sigma Aldrich) for organic sensitizers **TTZ3**, **TTZ5**, and **TTZ7** (synthesized by CNR-ICCOM [6]) and stored at 4°C, away from light, till their use. The fibres were thus immersed in dye solutions at room temperature for 20 h to allow the adsorption of the dye molecules onto the TiO₂ surface.

5.4. Electrolytes

Different electrolytes have been used during this research work.

5.4.1. Liquid electrolytes

I⁻/I₃⁻ based electrolyte which has been used it is commercially available electrolyte EL-HPE (Dyesol Ltd, Australia). A liquid electrolyte based on the redox couple Co²⁺/Co³⁺ has been prepared in ACN (Sigma-Aldrich) as reported in *Table 5.2*, using [Co(bpy)₃](PF₆)₂ and [Co(bpy)₃](PF₆)₃ purchased from Dyenamo AB (Sweden), TBT (Sigma-Aldrich), and LiClO₄ (Sigma-Aldrich).

Table 5.2. Concentrations of the different reactants composing the ACN solution used as liquid electrolyte for cells testing.

	Concentration [mol/L]
[Co(bpy) ₃](PF ₆) ₂	0.22
[Co(bpy) ₃](PF ₆) ₃	0.05
TBT	0.20
LiClO ₄	0.10

5.4.2. Gel-state electrolyte

Gel system electrolyte have been obtained from liquid electrolytes using a PMMA-based polymeric gelation through a room temperature process [7] and a SiO₂ nanoparticles based-gelation [8]. In the first case acetone (99.5 %, Sigma-Aldrich, USA) was used as the solvent for the gelation of PMMA (average MW 120000 g/mol, Sigma-Aldrich, USA). Polyethylene glycol (PEG 200, Merk, Germany) (0.35g) was mixed to the solvent (10 mL) to improve the plasticity of the gel, PMMA (0.25 g) was then added and the solution was stirred at room temperature until it was completely homogeneous. Ethylene carbonate (EC, 98%, Sigma-Aldrich, USA) (0.4 g) was finally added to improve the ionic conductivity of the system. The final composition of the dry gel was PMMA 25 wt%, PEG 200 35% wt and EC 40% wt. The gel electrolyte was prepared by adding the liquid electrolyte solution (80 % wt) directly the gelling one (20 % wt). The as-obtained solution could be applied with a glass pasteur pipette, as for the liquid ones, due to its

low viscosity. Regarding the SiO₂ method, Fumed Silica nanoparticles (5 %wt and 3% wt) with 7 nm primary particle size Sigma-Aldrich were mixed under sonication with liquid electrolyte to produce a stable gel.

5.5. Counter electrodes

5.5.1. Pt counter electrodes

Pt counter electrodes were fabricated by cutting in difference length, on the basis of the cell assembled, Pt wires (diam. 0.2 mm, Agar Scientific). The fibres thus obtained were subjected to the same cleaning process applied for Ti-wire (*section 5.2.1.1*).

5.5.2. Kevlar-PPy coated based counter electrodes

The Kevlar conductive fibres were used as counter electrodes with Ti-wire based photoanodes as working electrode.

5.6. Cells assembly

Parallel electrodes configuration cells have been assembled as shown in *Figure 5.4*. After photoanodes and counter electrodes fabrication, they were inserted in a transparent plastic tube (BOLA, Germany, diam. 0.5 mm x 1.6 mm) of the desired length (3.50 cm or 10.0 cm) and then fixed to the flexible mylar substrate, use as a support, by the application of a conductive silver glue (Agar Scientific) in order to establish the electric contact needed for the subsequent characterizations at the solar simulator.

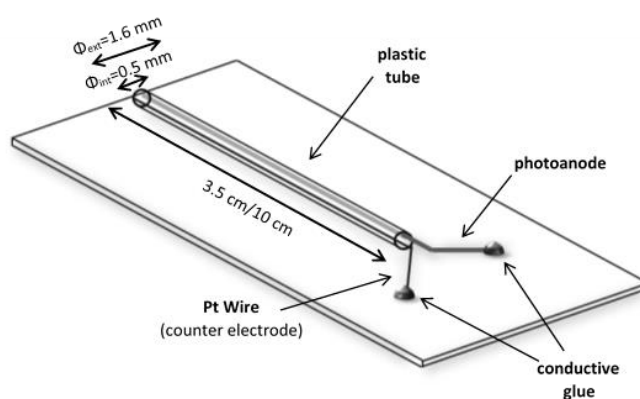


Figure 5.4. Schematic refiguration of the assembled cell used in this research work.

The electrolyte was finally introduced before each cell testing through the initial opening of the plastic tube with the help of glass Pasteur pipette. The active area of the cell was calculated as the area of a rectangle having as a shorter dimension the thickness of the TiO₂ layer multiplied for two, and for longer dimension the length of the cell.

5.7. Components characterization

Each component has been completely characterized before been applied on the final photovoltaic device.

5.7.1. Titanium-wire based photoanodes characterization

The most relevant properties of employed photoanodes were analysed to obtain a complete characterization of these components.

5.7.1.1. Mass determination of TiO₂ coating

The mass of photoanodes with different thickness was obtained by subtraction of Ti-wire substrates masses to the masses of the assembled photoanodes. Three samples were prepared for each TiO₂ thickness (2,3,4,5,6 layers).

After the cleaning process of the Ti wires (see section 5.2.1), samples were dried in a muffle furnace at 100°C for 30 min and then placed in a desiccator under vacuum to cool down, preventing, in this way, the adsorption of water molecules. The actual mass of each substrate before the application of the TiO₂ coating was then determined using an analytical balance (0.1 mg). The process was repeated after the deposition of TiO₂ coating and TiCl₄ treatment determining the mass of the final photoanodes.

5.7.1.2. Thickness determination of TiO₂ coating

Coating thickness was determined for a representative sample for each number of deposited layers (2-6) by Field-Emission scanning electronic microscopy (FE-SEM, SIGMA: Zeiss, Germany) analysing the cross section of each samples.

5.7.1.3. Electrochemical Characterization of TiO₂ coating

High speed (1 V/s) cyclic voltammetry curves of photoanodes with different TiO₂ layers thickness were collected in H₂SO₄ 0.1 M, between +0.3 V and -0.8 V in a three electrode configuration: fibre (immersion length 2.0 cm), SCE and Pt wire with a AUTOLAB PGSTAT302N-FRA32M electrochemical working station (Metrohm) and using NOVA 2.0 (Software).

5.7.1.4. Spectrophotometric determination of the amount of adsorbed dye

In the first part of the project a comparison between the amount of dye loaded on the photoanode surfaces, expressed as moles of dye per mass of TiO₂, was evaluated because strictly related to the photocurrent producible. The determination was made through spectrophotometric analysis - *via* calibration curves - of the solution obtained from desorbing the dye on photoanodes (2 depositions). No blocking layer was applied because irrelevant for the purpose (*Figure 5.5*).

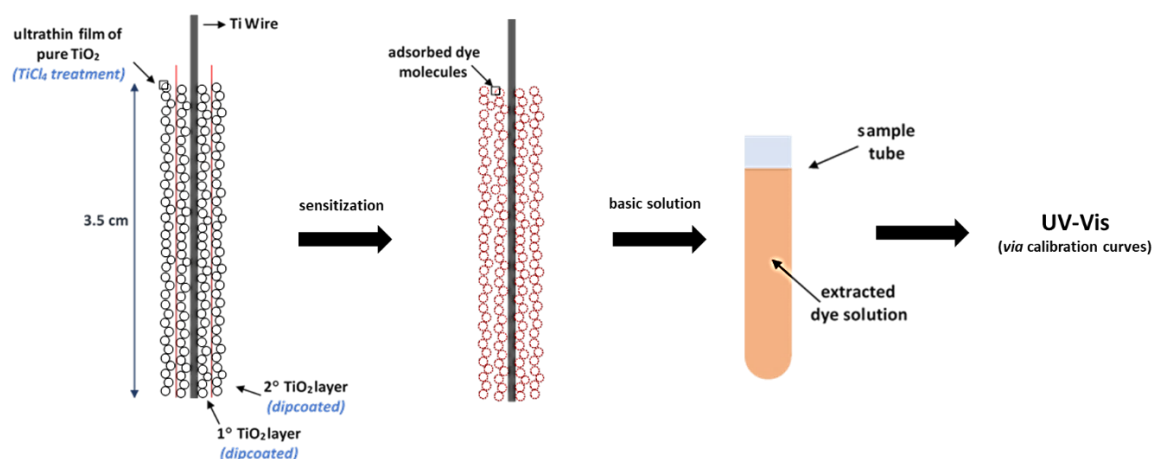


Figure 5.5. Schematic representation of the Spectrophotometric determination of the amount of adsorbed dye. Photoanode before sensitization (left), photoanode after sensitization (middle), solution of desorbed dye obtained after basic hydrolysis (right).

5.7.1.4.1. Calibration Curves

In order to obtain meaningful analytical data, different concentration solutions, were prepared in absolute EtOH for Ru-based dyes and in THF for fully-organic dyes and their UV-Vis spectra registered in the 350 - 800 nm region with a *Perkin Elmer Lambda35* Spectrometer. *Table 5.3.* reports the specific concentrations used for each dye.

Table 5.3. Concentration of the EtOH-based solution for Ru sensitizers (N719, N749), and of the THF:MeOH (1:1 % vol)-based solution for organic dyes (TTZ3, TTZ5, TTZ7) employed for the determination of the calibration curves.

solution	Concentration [10^{-3} mol/L]				
	N719	N749	TTZ3	TTZ5	TTZ7
2	0.200	0.200	10.0	10.0	19.9
3	0.180	0.180	9.00	9.00	17.9
4	0.160	0.160	8.00	8.00	15.9
5	0.140	0.140	7.00	7.00	13.9
6	0.120	0.120	6.00	6.00	11.9
7	0.100	0.100	5.00	5.00	9.90
8	0.0800	0.0800	4.00	4.00	-
9	0.0600	0.0600	-	-	-
10	0.0402	0.0402	-	-	-
11	0.0201	-	-	-	-

5.7.1.4.2. Extraction of the adsorbed dyes

The prepared sensitized fibres were subjected to the desorption method by exposing them to a known volume of a basic solution (basic hydrolysis of the bonds). Specifically, a 0.1 mol/L NaOH solution in EtOH was used for Ru-based dyes, and a 0.1 mol/L KOH solution in MeOH:THF (1:1 % vol) for organic dyes. The fibers were kept immersed until complete discoloration was observed, which was confirmed by checking the absence of absorbance of a new aliquot of basic solution.

5.7.2. *Kevlar-PPy coated-based photoanodes*

FE-SEM analysis of the fibres was initially performed in order to determine fibres diameter and morphology, including the effective presence of the conductive coating. The Same analysis was repeated after the deposition of the TiO₂ layer to establish the final photoanodes diameter and thus estimate the illuminated area of the cells tested. EDS detector was also employed on the coated fibres to confirm the nature of the deposited film.

5.7.3. *Optical characterization of Electrolytes*

Both the liquid and gel-state electrolytes have been optical characterized in order to determine the absorption of the systems in the range 350-850 nm. The characterization has been carried out in a sealed plastic tube (BOLA, diam 0.5 x 1.6 mm) in order to reproduce the condition of the cell using PVE300 Instrument (Bentham, U.K.).

5.7.4. *Kevlar-PPy coated-based counter electrodes characterization*

The catalytic activity towards I⁻/I₃⁻ redox couple regeneration was investigated through CV with a AUTOLAB PGSTAT302N (Methrohm) using NOVA 2.0 software, in a solution which mimed the commercial electrolyte EL-HPE, using a three-electrode system at a scan rate of 100 mV/s. LiI (Sigma-Aldrich), I₂ (Sigma-Aldrich), LiClO₄ (Sigma-Aldrich) were added to ACN (Sigma-Aldrich) in order to obtain the right concentration (*Table 5.4*).

Table 5.4. Composition of each species in the ACN solution imitating the EL-HPE electrolyte

	Concentration [10 ⁻³ mol/L]
LiI	10.0
I₂	1.00
LiClO₄	0.10

5.8. *FDSSCs characterization*

Complete FDSSC devices were tested under a solar simulator (SUN 2000, Abet Technologies, USA) calibrated with a standard silicon cell (ReRa Solution, The Netherlands). J-V were acquired by Keithley 2440 5A sourcemeter. EIS spectra were collected under illumination at 1000 Wm^{-2} (1 sun) AM 1.5 G illumination in the frequency range of 0.05 – 105 Hz with amplitude of 10mV and open circuit condition with AUTOLAB PGSTAT302N+FRA32M – software NOVA 2.0. Both characterization techniques were carried out under normal conditions (not-stressed devices) and after a mechanical stress was applied, in order to study potential changes in PV performances (*Figure 5.6*).

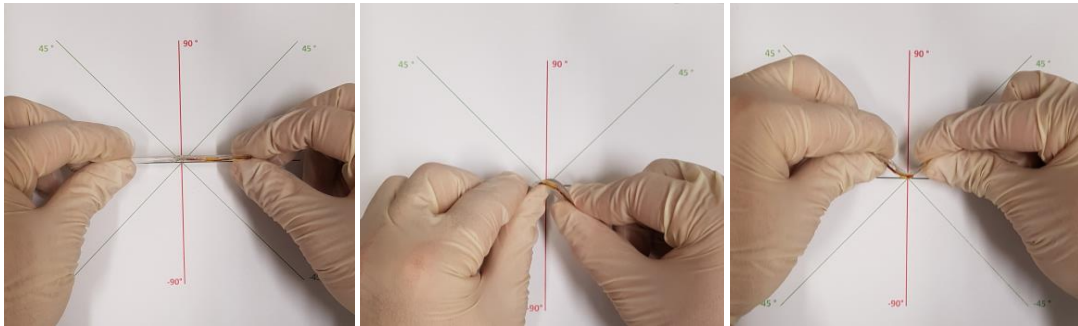


Figure 5.6. Single cycle of mechanical stress applied to each cell. The cycle was repeated 10 times for each device.

5.9. *Characterization techniques*

5.9.1. *Scanning Electron Microscopy*

In this thesis Scanning Electron Microscopy (SEM) was used for the study of the surface morphology of electrodes and for the determination of the TiO_2 thicknesses deposited onto Ti-wire surface by cross sectional SEM analysis, which is a standard method to estimate the thickness of solid state device layers [9].

Thank to the use of a beam of electrons (0.1-30 keV) focused to a diameter spot in the range of approximately 1-100nm [10] on the surface of the specimen and scanned back and forth across the surface, an image of the sample is created. The electron beam interacts with the atoms on the surface of the specimen giving information about surface topography and composition if a Energy Dispersive X-Ray Spectroscopy detector

(EDS) is used. The surface topography is revealed either by the reflected (backscattered) electrons generated or by electrons ejected from the specimen as the incident electrons decelerate secondary electrons. In order to be able to measure, samples need to be electrically conductive, at least at the surface. For this reason the analysed samples have been covered with a thin layer of gold by sputtering deposition.

5.9.2. Cyclic Voltammetry

Cyclic Voltammetry (CV) has been used to characterize the FDSSCs electrodes. In particular photoanodes characterization has been carried out through high speed (1 V/s) cyclic voltammetry in H_2SO_4 0.1 M, between +0.3 V and -0.8 V in a three electrode system: fibre (immersion length 2.0 cm), SCE and Pt wire; CV was performed on Kevlar-based counter electrodes to characterize the catalytic activity of the fibres over the I_3^-/I^- couple in a solution which mimed the commercial electrolyte EL-HPE (section 5.7.4).

Voltammetric techniques are based on the measurement of the current as a function of the applied potential when an electrochemical process takes place. In classic voltammetry the potential provided to the working electrode is varied linearly with time (Linear Scan Voltammetry). On the contrary, in cyclic voltammetry the potential assumes a characteristic triangular shape. A linear potential ramp is indeed applied to the working electrode between time t_0 and t_1 , then it is inverted so that at t_2 the potential is equal to the initial value. This cycle can be repeated several times. At the end a voltammograms, current has been related to the potential of the redox couple in the solution. The current registered is therefore a Faradic current, *i.e.* the current related to the oxidation-reduction of the species which take place on the electrode surface. Faradic current is subjected to the interference of the capacitive charging current generated by charged molecules in motion within the solution which participate to phenomena not related to the redox reaction such as mass transport, migration or convection. These phenomena can be reduced by using a support electrolyte which migrates in place of the redox species and by avoiding the stirring of the solution during the analysis.

Cyclic voltammetry is largely employed because it allows to obtain several information about the analysed species and the related reactions in a simple way. If we indicate as P^A and P^C respectively the anodic peak (oxidation) and the cathodic peak (reduction), the most relevant parameters that can be obtain by the analysis are i_P^A/i_P^C , *i.e.* the ratio

between current peaks, and $E_{PA}-E_{PC}$, which is a measure of the distance of the peaks. If the redox reaction is completely reversible, anodic and cathodic current are the same, meaning that the first fraction is unitary and the second is equal, at 25°C, to 57/n mV (Butler-Volmer equation), for an n electrons process [11]. On the other hand, for an irreversible reaction, anodic and cathodic peaks tend to get larger and more separated till the extreme case when no peak is registered after the oxidation.

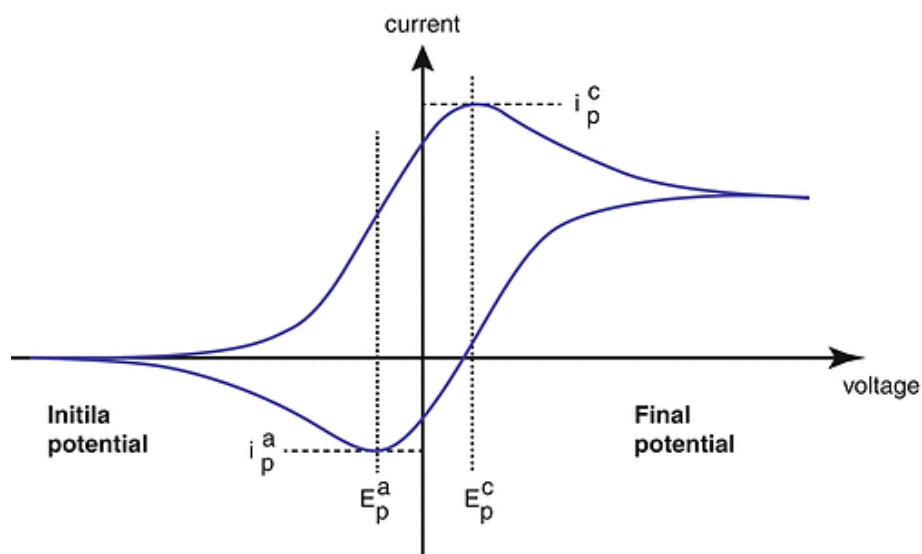


Figure 5.7. Typical cyclic voltammogram where i_p^c and i_p^a show the peak cathodic and anodic current respectively for a reversible reaction.

In CV the scan rate is important and must be indicated. In fact, The Randles-Sevcik equation (for reversible system) shows the relationship between scan rate and peak current (i_p):

$$i_p = 0.4463 n F A C \left(\frac{n F v D}{RT} \right)^{\frac{1}{2}}$$

being “n” the number of electron transferred in the redox reaction, “A” the electrode area (cm^2), “F” the Faraday constant (Cmol^{-1}), “D” the diffusion coefficient (cm^2s^{-1}), “C” the concentration (molL^{-1}), “v” the scan rate (Vs^{-1}), “R” the Gas constant ($\text{J}^\circ\text{C}^{-1}\text{mol}^{-1}$), and “T” the temperature ($^\circ\text{C}$).

5.9.3. *UV-Visible Spectroscopy*

UV-Visible (UV-Vis) spectroscopy have been employed during the research work, to establish the amount of dye adsorbed onto photoanodes surface.

During an UV-Vis analysis a sample is irradiated with an intensity of UV-Vis light (I_0) and the intensity of the light after it has passed through the sample (I) is measured through a detector. The absorbance (A) of the sample is thus obtain, as a function of the wavelength of the light, as described by the following relation:

$$A = \log_{10} \left(\frac{I_0}{I} \right)$$

Absorbance at a certain wavelength (λ) is connected to the concentration of the species which absor light in the sample (C) by the molar attenuation coefficient at the same wavelength ($\epsilon_{(\lambda)}$) and the leght for the light to travel, usually reffered as “optical path” (l), by the Lambert-Beers law [12]:

$$A_{(\lambda)} = C \cdot \epsilon_{(\lambda)} \cdot l$$

Through the construction of calibration curves obtained by registering the absorbance of known concentration solutions is thus possible, measuring the absorbance of an unknown concentration specimen, to determine the concentration of the sample.

5.9.4. *Current-Voltage measurements*

Solar cells are evaluated by power conversion efficiency (η) which is calculated from the current-voltage spectrum of the device. By illuminating the solar cell, scanning the voltage and measuring the current using a potentiostat/sourcemeater, it is possible to plot the current-voltage curve or the density current-voltage curve by knowing the active area of the photoanode. This kind of measure allows to obtain all the photovoltaic parameters which concur to the estabilishment of the efficiency of the device.

The points where the curve intersecates the axes, *i.e.* photovoltage at zero current and photocurrent at zero voltage, are called respectively open-circuit voltage (V_{OC}) and short-circuit current (I_{SC}) or short-circuit density current (J_{SC}) if density current is considered [13].

As it has already been said in *Chapter 2 (section 2.2.1)*, the efficiency of the solar cell is the ratio of maximum solar cell power to the intensity of incoming light, and can be described by the following expression:

$$\eta = \frac{P_{\max}}{P_{\text{in}}} = \frac{\text{FF} \cdot V_{\text{oc}} \cdot I_{\text{sc}}}{1000[\text{W} \cdot \text{m}^{-2}]}$$

where FF is the Fill Factor of the cells.

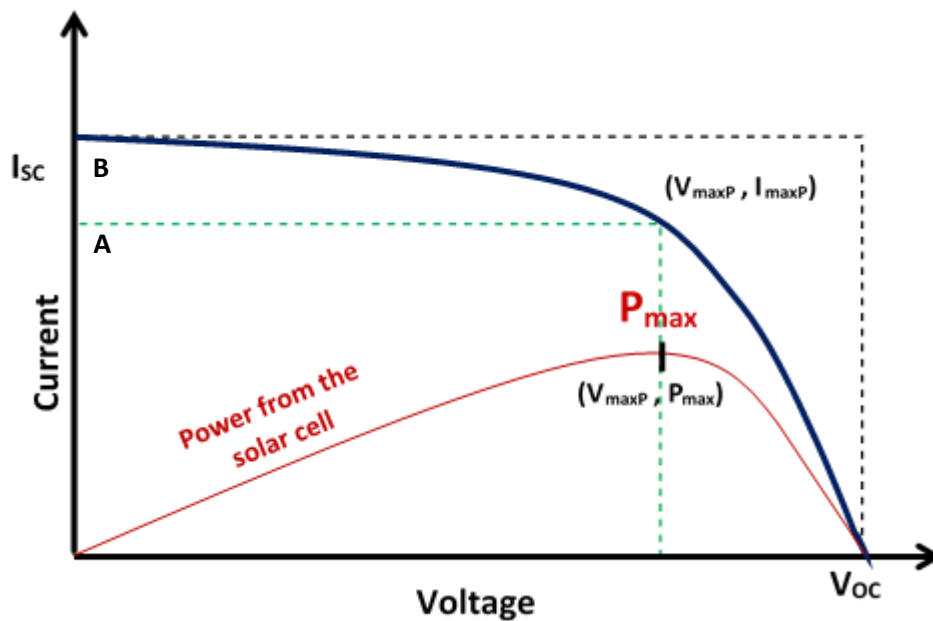


Figure 5.8. Typical I-V curve of a solar cell with the different areas that help defining the FF (A/B).

This parameter is defined as the ratio of the maximum power from the solar cell to the product of V_{oc} and I_{sc} . Referring to *Figure 5.8*:

$$\text{FF} = \frac{P_{\max}}{V_{\text{oc}} \cdot I_{\text{sc}}} = \frac{(I_{\text{maxP}} \cdot V_{\text{maxP}})}{V_{\text{oc}} \cdot I_{\text{sc}}} = \frac{(I_{\text{maxP}} \cdot V_{\text{maxP}})}{V_{\text{oc}} \cdot I_{\text{sc}}} = \frac{\text{Area A}}{\text{Area B}}$$

where J_{\max} and V_{\max} are respectively the current density and the potential at the maximum power. For this reason, the FF is usually referred as the “squareness” of the I-V curve: the greater the area of A (*i.e.* a more square-shaped curve), the greater the FF.

5.9.5. *Electrochemical Impedance Spectroscopy*

Electrochemical Impedance Spectroscopy (EIS) is one of the most frequently used characterization techniques for FDSSCs for the study of charge transfer and transport processes occurring inside the devices [14].

In this method a small sinusoidal voltage modulation (dV , typically ~ 10 mV) is superimposed on the potential that is applied to the device by a potentiostat [13] and the response current is measured at the same frequency. Indicating with $V(\omega, t) = V_0 \sin \omega t$ the small signal sinusoidal voltage with amplitude V_0 and variable frequency f ($f = \omega/2\pi$, where ω is the angular frequency) and $I(\omega, t)$ the current, the impedance $Z(\omega, t)$ related to the system can be calculated through the Ohm’s Law as [14]:

$$Z(\omega, t) = \frac{V(\omega, t)}{I(\omega, t)}$$

For a given ω , the current response could be in-phase or out-of phase with respect to the voltage stimulus, so that its general expression is given by $I(\omega, t) = I_0 \sin(\omega t - \theta)$, where I_0 is the current signal amplitude and θ is the phase angle between voltage and current.

By exploiting the complex number notation, the AC voltage and current signals can be expressed as $V(\omega, t) = V_0 e^{j\omega t}$ and $I(\omega, t) = I_0 e^{j(\omega t - \theta)}$ respectively, where j is the imaginary unit [14]. With these notations, the previous equation can be rewritten as:

$$Z(\omega, t) = \frac{V(\omega, t)}{I(\omega, t)} = \frac{V_0}{I_0} e^{j\theta} = |Z(\omega)| e^{j\theta}$$

where $|Z|$ is the impedance modulus and θ is the impedance phase. This equation can be further modified by applying Euler's relationship, thus obtaining:

$$|Z(\omega, t)| = |Z(\omega, t)|(\cos\theta + j\sin\theta) = Z'(\omega) + jZ''(\omega)$$

where $Z' = |Z|\cos\theta$ and $Z'' = |Z|\sin\theta$ are the real and the imaginary part of the impedance, respectively.

Two different representations are usually exploited for presenting EIS data. The first one reports Z'' as a function of Z' in the complex plane, and it is referred to as Nyquist plot. The Nyquist representation is more compact, even if the frequency dependence is not explicitly evident, and is the one reported in this research work. On the other part, the Bode plots are a pair of graphs reporting $\log|Z|$ and θ as a function of $\log f$.

When measuring a standard FDSSC, half circles will appear in the spectrum. A standard Nyquist plot of a FDSSC is shown in *Figure 5.9*.

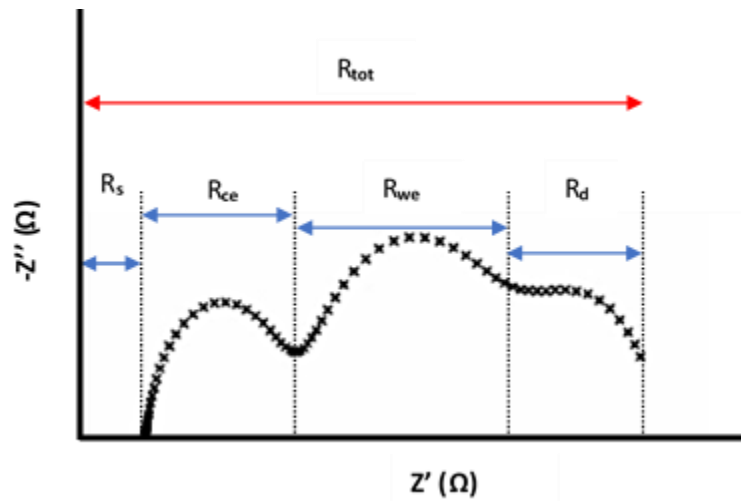


Figure 5.9. Typical Nyquist plot of a FDSSC measured under open circuit condition. The total resistance R_{tot} , is depending on the series resistance R_s , the charge transfer resistance at the counter electrode R_{ce} , the electron transport in the TiO_2 and recombination resistance of electron in the TiO_2 conduction band to the redox couple in the electrolyte R_{we} and the diffusion resistance for the redox couple in the electrolyte, R_D .

A resistance can be associated to each arch which value is approximately given by the diameter of the arch [14]. At high frequency (left part of the plot) the resistance associated to the charge transfer at the counter electrode produces the first half circles, at middle frequencies the electron transport resistance in the TiO_2 layer and the recombination resistance of electron in the mesoporous film are responsible for the second arch and finally in the right part of the plot, *i.e.* at low frequency, the resistance related to the diffusion within the electrolyte gives the third arch.

Equivalent circuits are used to analyse the impedance spectrum and extract the related information about the different components, *i.e.* series resistance, chemical capacitance,

transport resistance, recombination resistance, counter electrode charge transfer resistance and capacitance [13]. They are composed of standard electrical components, such as resistors (R) and capacitors (C) and any virtual electrical component is related to a particular parameter in the device.

References

- [1] Y. P. Fu, Z. B. Lv, S. C. Hou, H. W. Wu, D. Wang, C. Zhang, Z. Z. Chu, X. Cai, X. Fan, Z. L. Wang and D. C. Zou, “Conjunction of fiber solar cells with groovy micro-reflectors as highly efficient energy harvesters Energy”, *Environ. Sci.*, 4, pp. 3379–3383. 2011
- [2] S. Hou, “Fiber Solar Cells. Materials, Processing, and Devices”, *Springer Thesis*, 2017.
- [3] T. Sekiya, K. Ichimura, M. Igarashi, S. Kurita, “Absorption spectra of anatase TiO₂ single crystals heat-treated under oxygen atmosphere”, 61, pp. 1237-1242, 2000.
- [4] A. Hagfeldt, G. Boschloo, L. Sun, L. Kloo, H. Pettersson, “Dye-sensitized solar cells,” *Chem. Rev.*, 110 pp. 6595-6663, 2010.
- [5] S. Ito, T. Murakami, P. Comte, P. Liska, C. Grätzel, M.K. Nazeeruddin, M. Grätzel, “Fabrication of thin film dye sensitized solar cells with solar to electric power conversion efficiency over 10%”, *Thin Solid Film*, 516, pp- 4613-4619, 2008.
- [6] A. Dessì *et al.*, “Thiazolo[5,4-d]thiazole-based organic sensitizers with strong visible light absorption for transparent, efficient and stable dye-sensitized solar cells,” *RSC Adv.*, 5, 41, pp. 32657–32668, 2015.
- [7] R. Bendoni, A.-L. Barthélémy, N. Sangiorgi, A. Sangiorgi, A. Sanson, “Dye-sensitized solar cells based on N719 and cobalt gel electrolyte obtained through a room temperature process”, *J. Photochem. Photobiol. A: Chem.*, 330, pp. 8-14, 2016.
- [8] P. Wang, S. M. Zakeeruddin, P. Comte, I. Exnar, M. Grätzel, “Gelation of Ionic Liquid-Based Electrolytes with Silica Nanoparticles for Quasi-Solid-State Dye-Sensitized Solar Cells”, *J. Am. Chem. Soc.*, 125, pp.1166-1167, 2003.
- [9] H. J. Snaith and L. Schimidt-Mende, “Advances in Liquid-Electrolyte and Solid-State Dye-Sensitized Solar Cells”, *Adv. Mater*, 19, pp. 3187-3200, 2007.

- [10] W. Zhou, R.P. Apkarian, Z. L. Wang, D. Joy, “Fundamentals of Scanning Electron Microscopy”, in *Scanning Microscopy for Nanotechnology*, pp. 1-40, Springer, New York, 2007.
- [11] A. J. Bard, L. R. Faulkner, “*Electrochemical Methods: Fundamentals and Application*”, John Wiley and Sons, Inc, 2001.
- [12] D. S. Hage, J. D. Carr, “Analytical chemistry and quantitative analysis”, Pearson Education, 2011.
- [13] M. Pazoki, U. B. Cappel, E. M. J. Johansson, A. Hagfeldt, G. Boschloo, “Characterization techniques for dye-sensitized solar cells”, *Energy Environ. Sci*, 10, pp. 672-709, 2017.
- [14] A. Sacco, “Electrochemical impedance spectroscopy: Fundamentals and application in dye-sensitized solar cells”, *Renew.Sust. Ener. Rev.*, 79, pp. 814-829, 2017.

Chapter 6. Results and Discussions

6.1. *Physicochemical characterization of TiO₂ photoanodes*

Each newly-developed photoanode material must be completely characterized before being applied on the final photovoltaic device. The determination of some key properties such as film thickness and morphology, electrochemical behaviour and dye uptake must be strictly optimized in order to prepare highly efficient photoanode material. In particular: the mass of the active layer and its thickness are fundamental to calculate the final sunlight conversion efficiency; the electrochemical properties describe the accumulation mechanism of charges inside TiO₂ and the cations present into the electrolyte; finally the amount of dye adsorbed is linked to the photocurrent produced during the device operation.

6.1.1. *Semiconductor mass and thickness*

The thickness and mass of the dip-coated semiconductor layers (photoanode) are directly correlated to the amount of adsorbed sensitizer and therefore represent critical properties that affect the final DSSCs performances.

The average mass of the mesoporous TiO₂ film, obtained by weighting the fibres before and after deposition and sintering of the Titania, is shown in *Figure 6.1* as a function of number of dip-coated layers deposited. To prevent the adsorption of water molecules on the TiO₂ surface, the samples (two fibres for each typology, diam. 0.5, length 4.0 cm deposited length 3.5 cm) were dried in a muffle furnace at 100 °C for 30 min and then cooled down under vacuum in a desiccator before weighting.

As expected, the TiO₂ mass increases linearly ($R^2 = 0,9970$) with the number of deposited layers, testifying the additivity of the dip-coating process. *Figure 6.2* shows cross-sectional SEM micrographs of the coating, which have been employed, as a standard procedure [1], to estimate the thickness of the TiO₂ layers reported in *Table 6.1*.

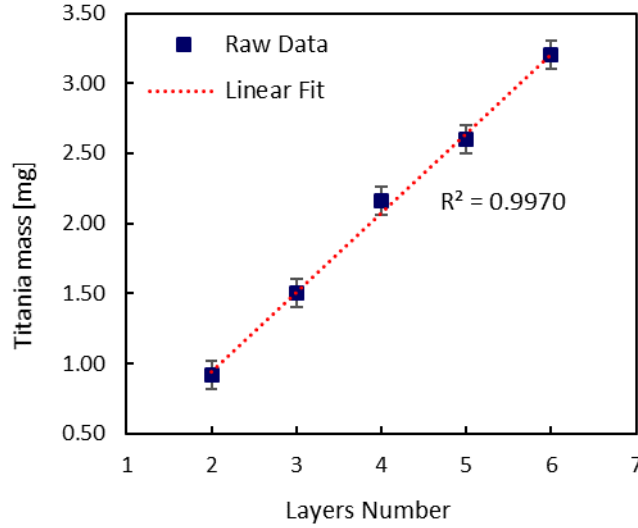


Figure 6.1. Mass of dip-coated TiO₂ film as function of dip-coated layers number.

Table 6.1. Coating mass and thickness values for different layers number.

number of layers	coating mass [mg]	coating thickness [μm]
2	0.92 ± 0.1	5
3	1.50 ± 0.1	8
4	2.16 ± 0.1	10
5	2.60 ± 0.1	13
6	3.20 ± 0.1	19

As shown by plotting the TiO₂ layers thickness as a function of the number of dip-coated layers (*Figure 6.3*), the coating becomes linearly thicker with the increase of deposited layers excepts for the thickest coating (6 depositions). More specifically, considering values in the range 2-5 depositions, a linear correlation between thickness and number of depositions and therefore mass and number of depositions can be identified (red dotted lines); this correlation almost disappears when mass and thickness values related to 6 depositions are considered (blue dotted lines).

Based on the mass linearity with the coating number stated above, this result could be attributed to the dip-coating process itself. When a new layer is added, part of the ink penetrates in the porosity of the previous coating.

With thicker coating the porosity tends to be reduced both in dimension and in percentage. This results in a limited possibility for the ink to intrude in it, and therefore to relatively thicker layers. As explained in the previous chapter, thickness data are necessary to calculate photoanodes active areas needed for the extrapolation of the photovoltaic parameter J_{SC} (Short-Circuit Current Density).

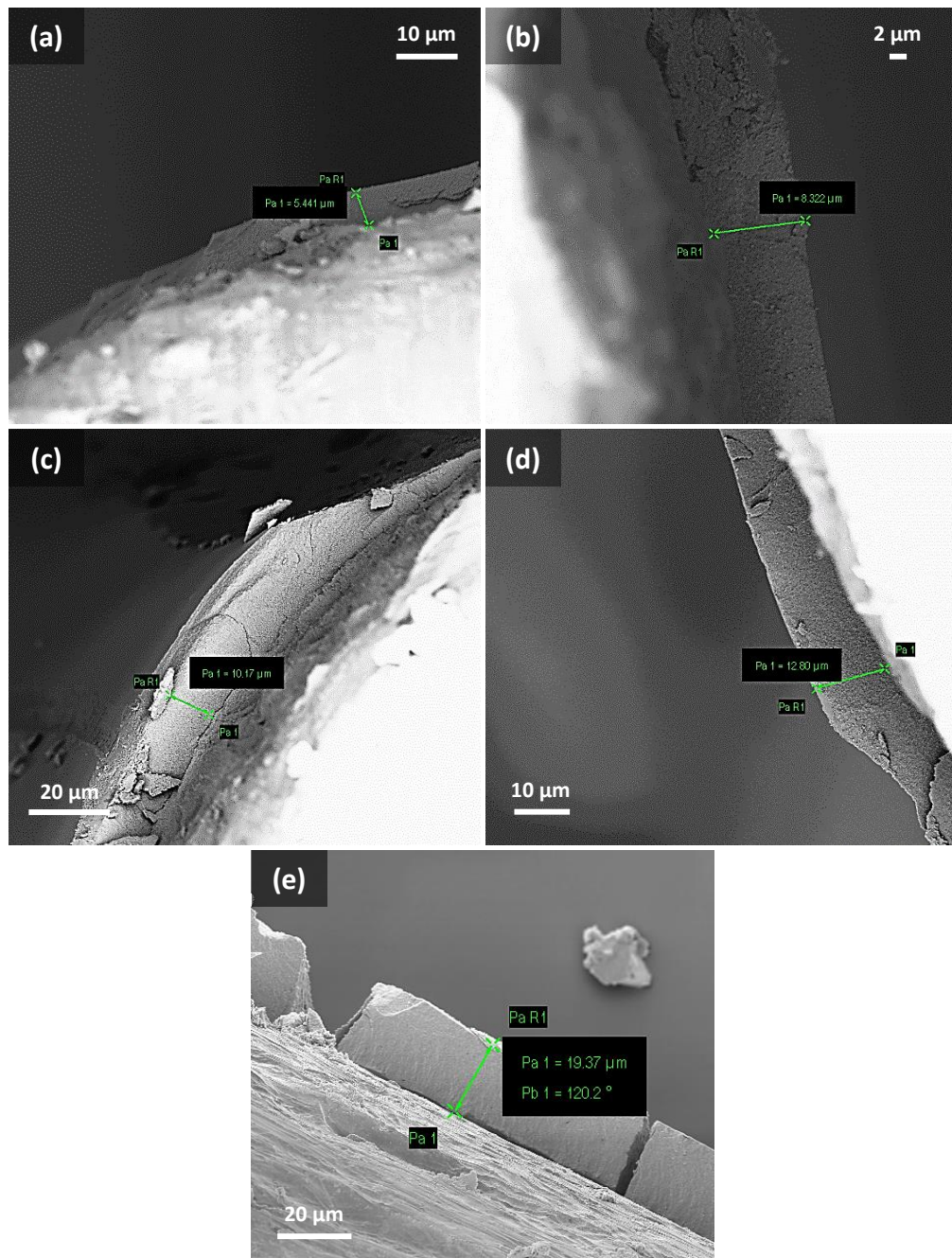


Figure 6.2. Cross section SEM images of 2 layers (a), 3 layers (b), 4 layers (c), 5 layers (d), 6 layers (e) deposition fibres.

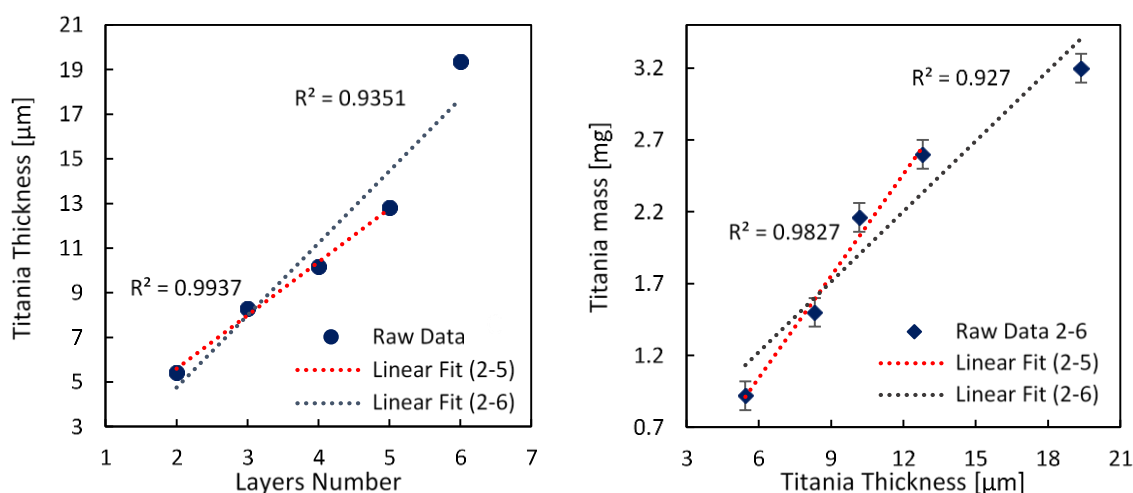
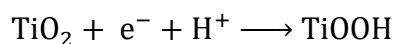


Figure 6.3. Coating thickness as function of number of layers (left) and coating mass as function of coating thickness (right). Two linear regressions are present in each graph (dotted lines). The red ones refer to data in the range of 2-5 depositions, the blue ones are obtained by including the values related to the 6th depositions as well.

6.1.2. Electrochemical characterization

In order to determine the electrochemical properties of the photoanodes, and in particular how the different thickness and amount of TiO₂ affect these properties, cyclic voltammetry (CV) on single fibres was performed. *Figure 6.4* shows high speed (1 V/s) CV curves of photoanodes based on titanium wires with diameter of 0.25 mm covered with different number of TiO₂ layers. The CV analyses have been performed in H₂SO₄ 0.1 M as electrolyte, with potential range between +0.3 V and -0.8 V in a three electrode system: fibre (immersion length 2.0 cm), SCE and Pt wire.

As displayed, around potentials where the TiO₂ is an insulator (0 V), the current shows a plateau. At more negative potentials, the cathodic current exponentially rises and leads to a peak when the direction of the voltammetry is reversed to anodic. It is known that at negative potentials and acid conditions, in the absence of any other redox couple, there is a faradic process of reduction of TiO₂ involving the injection of electrons into its conduction band and the proton transfer from the sulphuric acid [2]:



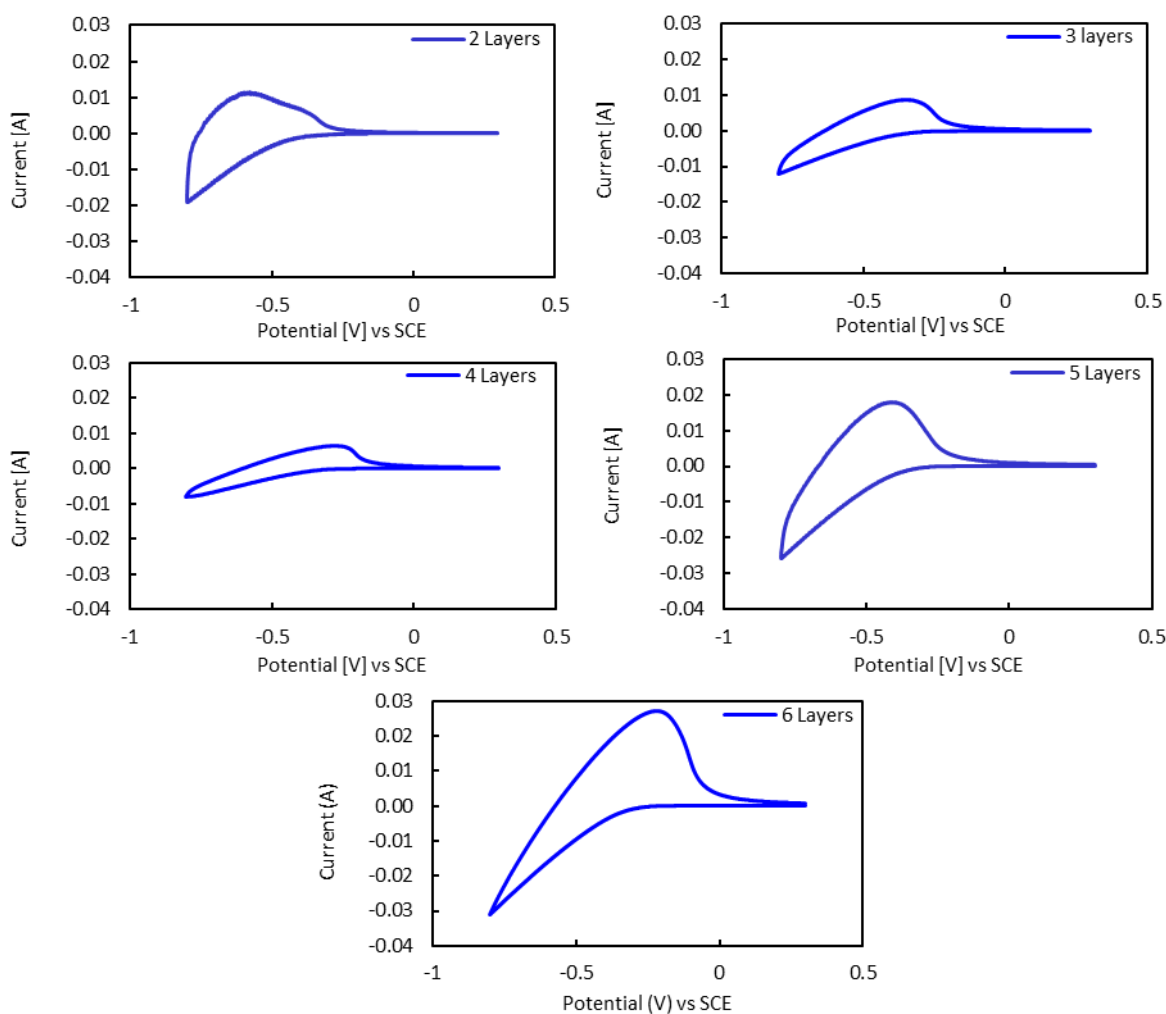


Figure 6.4. Cyclic voltammograms of TiO_2 -covered Ti wires for different coating thickness. The analyses are recorded at scan rate of 1 V/s in 0.1 M H_2SO_4 aqueous solution.

By dividing the integral area of the voltammograms, which represents the voltammetric charge, by the potential window and by the coating mass (see Table 6.1), it was possible to determine the specific capacitance (C_s) of the different TiO_2 layers (Table 6.2)[3].

Table 6.2. Specific capacitance (C_s) obtained from CV for different number of deposited layers.

number of layers	C_s [$\mu\text{F/g}$]
2	0.043
3	0.45
4	0.69
5	1.12
6	1.45

As shown in *Figure 6.5*, the capacitance values are directly correlated with the number of deposited TiO₂ layers.

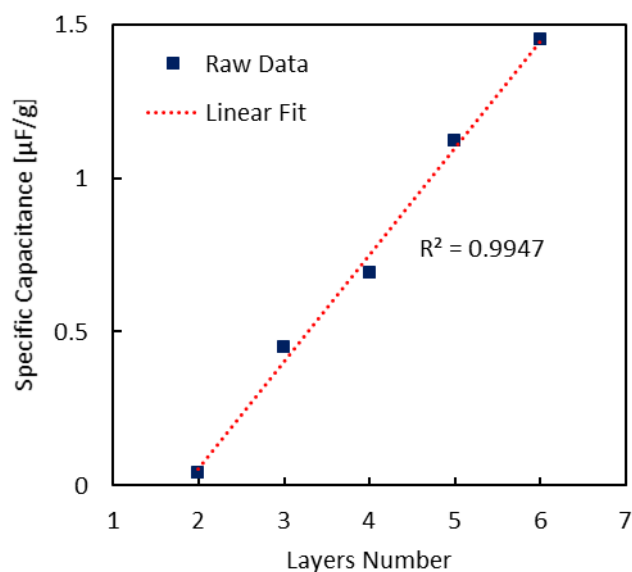


Figure 6.5. Specific capacitance as function of deposited TiO₂ layers number.

As expected, as the amount of TiO₂ on the metal wire substrate increases, so does the specific capacitance, due to the increased amount of active material able to store charges.

6.2. Comparison between commercially available Ru-based dyes and thiazolo[5,4-d] thiazole-based organic sensitizers

As previously explained the purpose of this work was to develop an optimized long Fibre-shaped Dye Sensitized Solar Cell (FDSSC) employing an innovative fully organic sensitizer, which has already shown promising results when applied in planar DSSCs, (power conversion efficiencies up to 7.71 %) [4].

For this reason, in the preliminary part of the project, a comparison of the properties of some of the most commonly used ruthenium metal-organic sensitizers **N749** (“Black Dye”), **N719** and a set of thiazolo[5,4-d] thiazole-based D- π -A organic dyes **TTZ3**, **TTZ5**, **TTZ7** (*Figure 6.6*) was made.

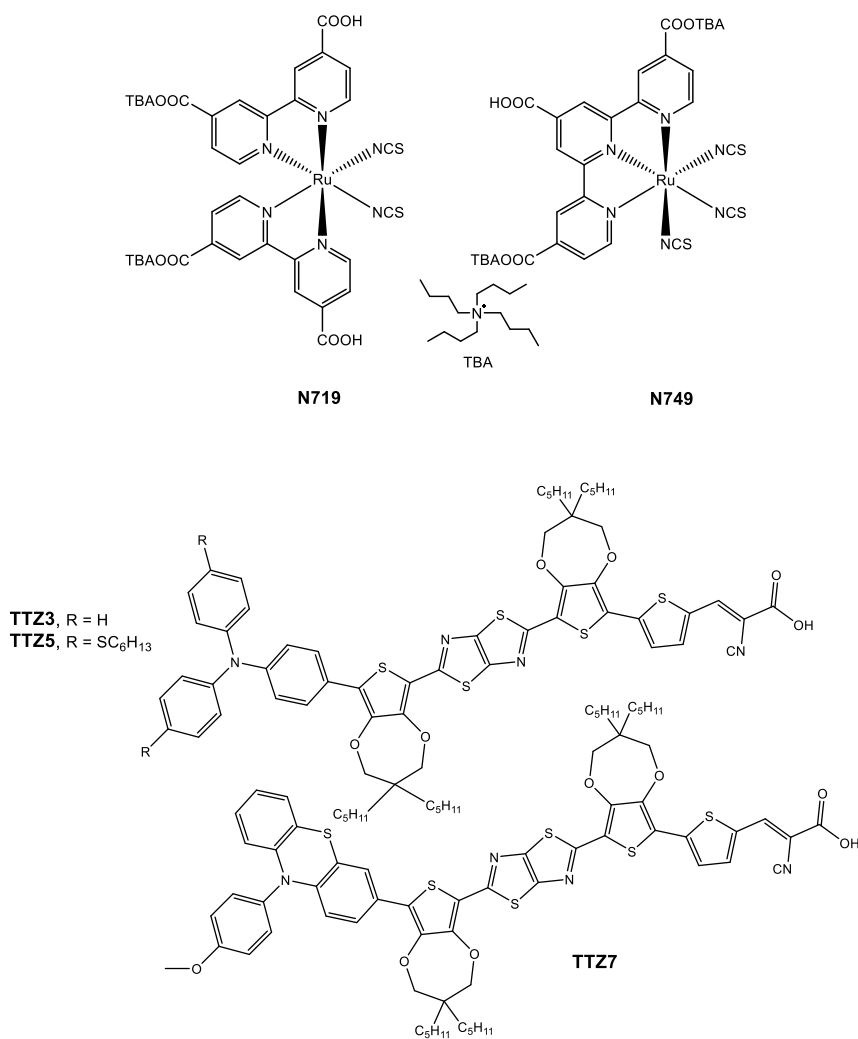


Figure 6.6. Chemical structure of the dyes used in the study

6.2.1. Spectrophotometric determination of the amount of adsorbed dye on TiO₂ surface

The amount of dye loaded on the photoanodes surface is a major aspect to evaluate for the development of highly efficient FDSSCs, because this value is directly correlated to the photocurrent produced by the final device. This parameter, expressed as moles of dye per mass of TiO₂, was evaluated for the set of chosen dyes sensitized on 5 μm-thick TiO₂ photoanodes (deposited length 3.5 cm) *via* calibration curves by desorbing the sensitizers and measuring the absorbance of the obtained solutions. The thickness was chosen as little as possible (minimum number of deposition) to ensure a mechanical resistance of the TiO₂ coating. Thicker photoanodes tend indeed to be more fragile and the consequently detachment of the coating could lead to false results.

6.2.1.1. Calibration curves

The UV-Vis spectra of ruthenium complexes used to extrapolate the calibration curves are displayed in *Figure 6.7*.

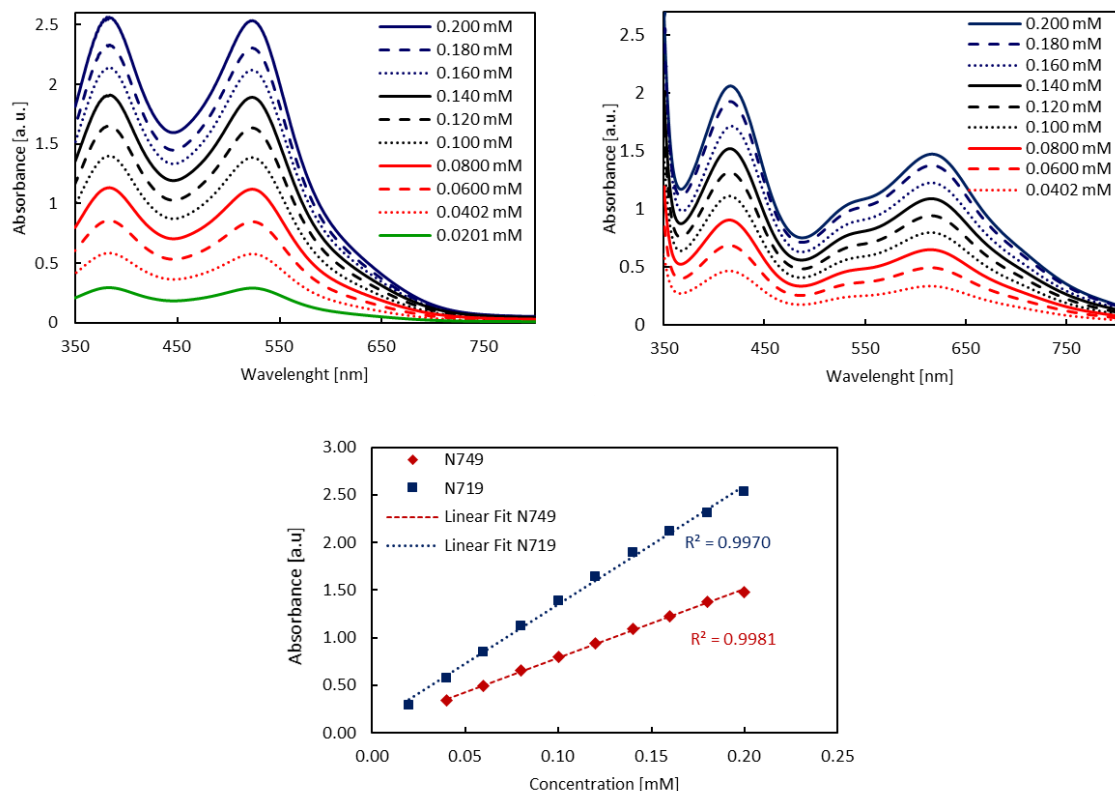


Figure 6.7. UV-Vis spectra at different concentrations of Ru-based dyes N719 (left) and N749 (right) in EtOH and resulting calibration curves.

In line with literature [5], they show the characteristic peaks assigned to the ligand-centred transition $\pi-\pi^*$ at 390 nm for N719 and at 430 nm for N749. The two peaks shifted to the visible range at about 530 - N719 - and 620 nm - N749 - derive, on the contrary, from Metal to Ligand Charge Transfer transitions (MLCT), responsible for the reddish (N719) and black (N749) colours of the dyes.

The class of D- π -A organic dyes, because of their similar structure, shows three UV-Vis spectra very analogous to each other, with broad and intense absorptions in the visible region (*Figure 6.8*) with maxima at about 510 nm, as expected from literature [4], [6]. This peak is correlated to the intramolecular charge transfer (ICT) which occurs between

the donor subunit and the acceptor through the π bridge [7],[8]. The spectra underline the extremely high light-absorption ability (high ϵ values) compared with the Ru-based sensitizers, which could be particularly useful for thin-layers TiO₂ dye sensitized solar cells.

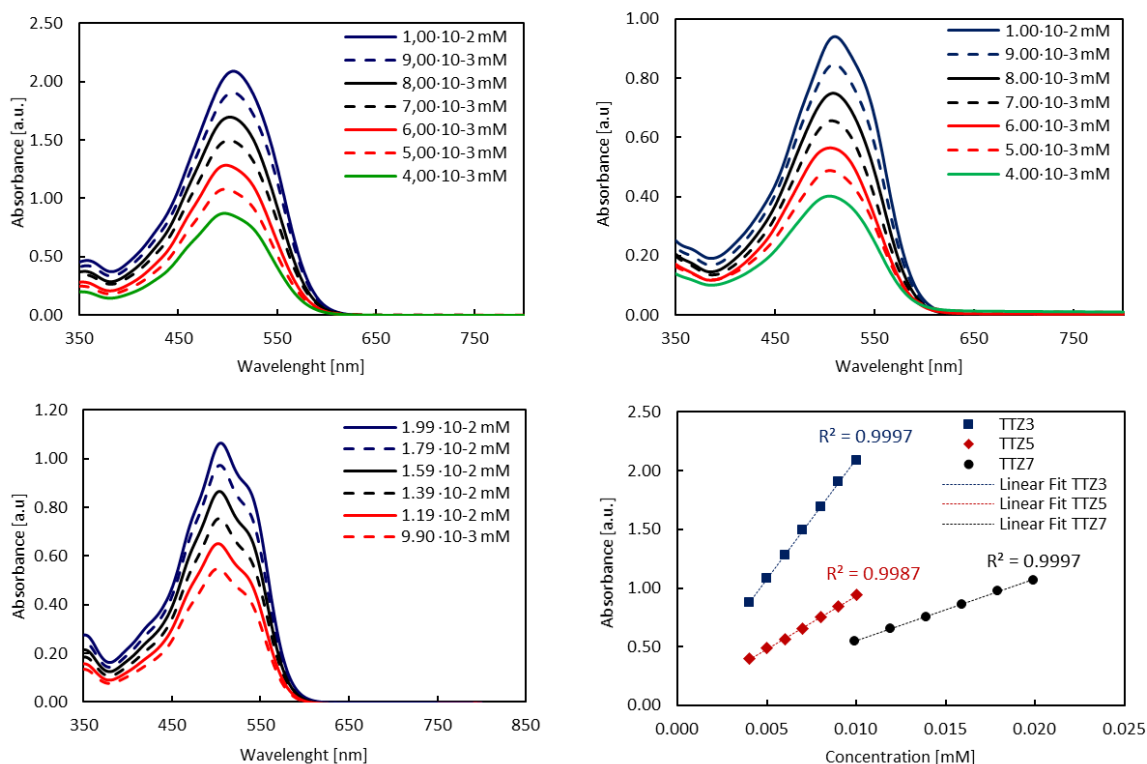


Figure 6.8. UV-Vis spectra at different concentration of TTZ3 (top left), TTZ5 (top right), TTZ7 (bottom left) solution (THF) and resulting calibration curves.

6.2.1.2. Amount of loaded dye

Table 6.3 provides the results of the spectrophotometric determination on the solution desorbed by the Titania layers. Commercial Ru-based dyes and TTZ3 molecules were absorbed in comparable amounts while TTZ5 and especially TTZ7 sensitizers were found to be adsorbed in higher amounts. These results were related to the presence of an higher number of oxygen atoms (ether group) in the structure of TTZ7 molecule that are able to more efficiently interact with the TiO₂ surface (see section 3.3.2.3. *Anchoring of the dye on the oxide surface*).

Table 6.3. Average values of the amount of adsorbed dye on 5 μm -thick TiO_2 . Data were obtained by measuring three samples for each dye.

dye	amount of dye [mmol/g TiO_2]
N719	0.034 \pm 0.02
N749	0.020 \pm 0.08
TTZ3	0.020 \pm 0.01
TTZ5	0.050 \pm 0.04
TTZ7	0.093 \pm 0.04

6.2.2. Photovoltaic Performances

At this point, photovoltaic performances of FDSSCs were assessed for **N719**, the more efficient ruthenium complex often used in literature as reference, and for **TTZ3** and **TTZ5**. The latter shares similar structure with the a triarylamine terminal donor unit and were compared in order to better investigate the effects of the *para*-position electron rich hexil-thio groups, which are expected to give improved electronic properties and thus higher photovoltaic efficiency. The geometry of the final FDSSCs is reported in *Figure 6.9*. In this first preliminary step, devices were kept as simple as possible, as it was reasoned that the efficiency data obtained under such simplified conditions could serve as a useful starting point to assess the potential of the new dyes. No blocking layer was therefore applied on titanium substrates, 5 μm -thick photoanodes were employed, and the redox couple I/I_3^- (EL-HPE electrolyte) was used as high efficient electrolyte since it is the one that usually works best with Ru-Based sensitizers [6].

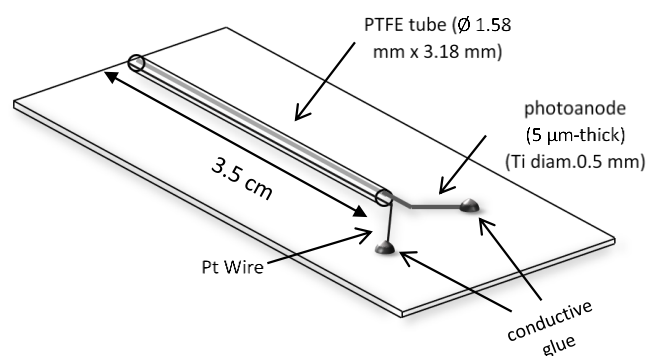


Figure 6.9. Schematic representation of the fibre DSSCs employed for the study.

The figure below illustrates the typical J-V curves obtained by current-voltage measurements, while the relevant photovoltaic extrapolated parameters are presented in *Table 6.4*.

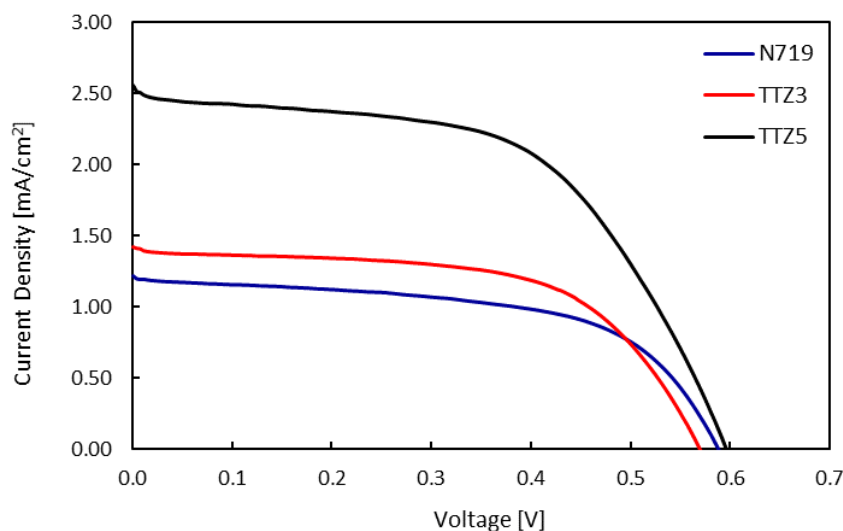


Figure 6.10. J-V of FDSSCs built with dye N719, TTZ3, and TTZ5

Table 6.4. Average values for three devices measured.

dye	J_{sc} [mA/cm²]	V_{oc} [mV]	FF [%]	η [%]
N719	1.3 ± 0.1	570 ± 21	58 ± 1	0.45 ± 0.03
TTZ3	1.5 ± 0.5	592 ± 33	56 ± 8	0.50 ± 0.12
TTZ5	2.1 ± 0.4	585 ± 10	60 ± 4	0.75 ± 0.12

As it can be seen from the table above, the group of organic dyes reported general higher efficiencies than the standard Ru-based **N719** dye, especially because of the high values of current density generated. In particular **TTZ5**, as a consequence of its higher absorption coefficient (81400 M⁻¹cm⁻¹ **TTZ3**, 94100 M⁻¹cm⁻¹ **TTZ5** [4], 16154 M⁻¹cm⁻¹ [1]) and absorption capability, was found to be the best dye for this type of fibre-shaped DSSCs.

6.3. Influence of TiO₂ thickness on the photovoltaic performances of TTZ5 – based fibre DSSCs

After having chosen the dye, the next step for the development of an efficient FDSSC involved the optimization of the thickness of the TiO₂ photoanodes.

The amount of adsorbed dye is strictly correlated to photocurrent generated by the solar cells, therefore the relation between an increased number of layers and the amount of adsorbed TTZ5 was investigated.

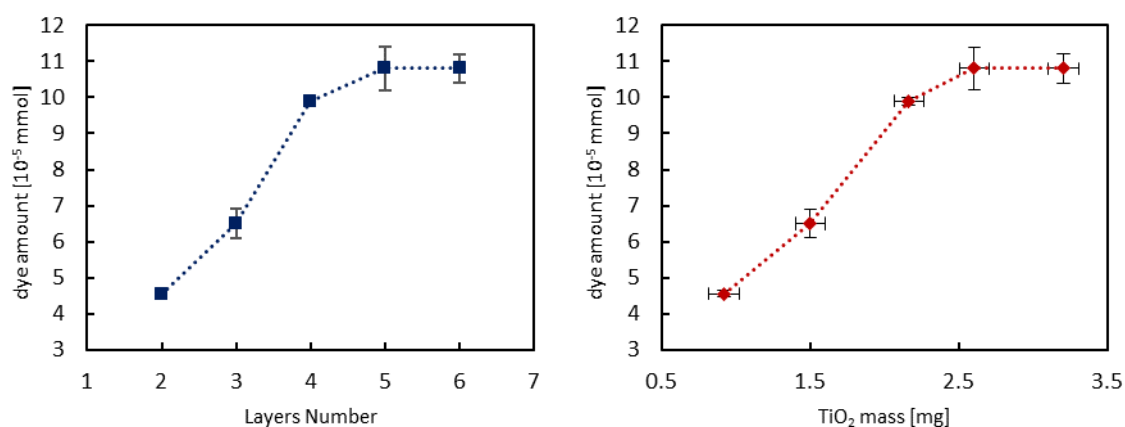


Figure 6.11. Average amount of TTZ5 adsorbed on TiO₂ photoanodes as function of number of depositions (left) and TiO₂ mass (right).

As highlighted in *Figure 6.11*, the millimoles of sensitizers increase, as expected, as the number of depositions and therefore mass of TiO₂ increase. This increment is almost linear between depositions 2 and 4 and then reaches a plateau.

Table 6.5. Average amount of TTZ5 adsorbed on TiO₂ photoanodes for different number of deposition/mass deposited.

number of layers	TiO ₂ mass [mg]	amount of TTZ5 [10^{-5} mmol]
2	0.92 ± 0.1	4.5 ± 0.1
3	1.50 ± 0.1	6.5 ± 0.4
4	2.16 ± 0.1	9.9 ± 0.1
5	2.60 ± 0.1	10.8 ± 0.6
6	3.20 ± 0.1	10.8 ± 0.4

By increasing the number of depositions, the probability of finding a discontinuity in the porosity of the TiO₂ coating increases consequently, preventing dye molecules from reaching inner zones of the coating.

In order to study the influence of the TiO₂ thickness on the final properties of the devices and their mechanical stability (*i.e.* variation of properties under mechanical stress), FDSSCs were prepared and tested under normal conditions (not stressed) and after that 10 cycles of the mechanical stress reported in *Figure 6.12* were applied. The related J-V curves with different number of TiO₂ depositions are reported in *Figure 6.13*, whose photovoltaic parameters are collected in *Table 6.6* and *Table 6.7*. for not stressed and stressed devices respectively.

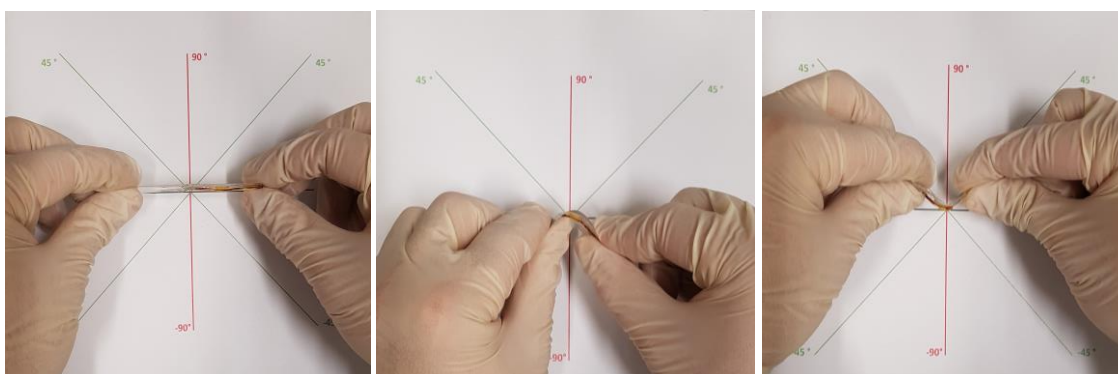


Figure 6.12. Single cycle of mechanical stress applied to each cell. The cycle was repeated 10 times for each device.

Table 6.6. Average photovoltaic parameters of three devices for different number of TiO₂ deposited. No mechanical stress was applied.

Layers number	J _{sc} [mA/cm ²]	V _{oc} [mV]	FF [%]	η [%]
2	3.8 ± 0.1	641 ± 7	48 ± 5	1.26 ± 0.06
3	4.4 ± 0.2	616 ± 4	49 ± 1	1.33 ± 0.07
4	4.8 ± 0.1	636 ± 8	51 ± 6	1.57 ± 0.15
5	4.5 ± 0.3	623 ± 4	52 ± 1	1.47 ± 0.07
6	2.8 ± 0.3	605 ± 22	58 ± 1	1.02 ± 0.16

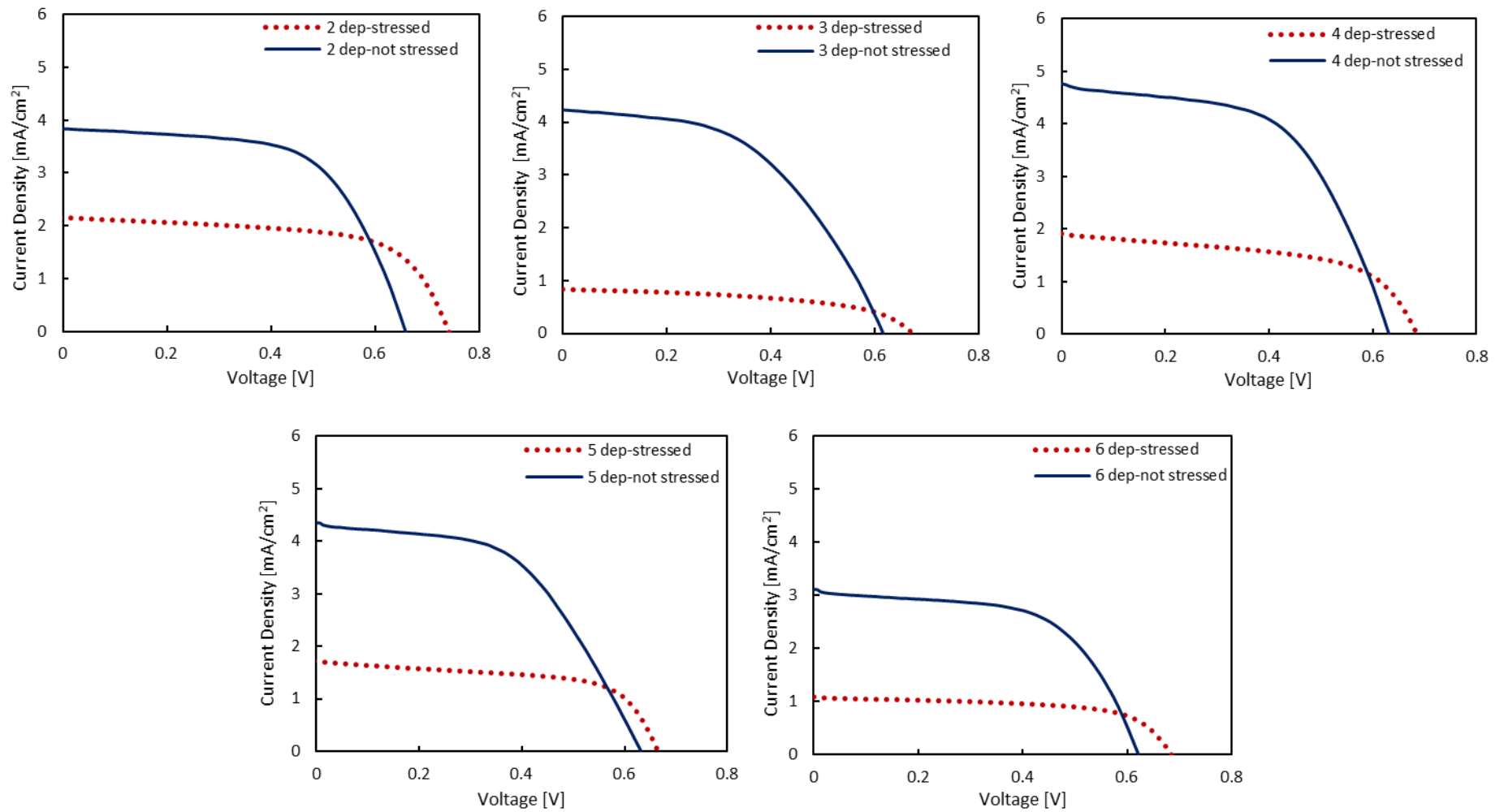


Figure 6.13. *J-V curves of a representative sample for each number of depositions (dep.) registered under normal condition (solid line) and after being stressed (dotted line).*

Table 6.7. Average photovoltaic parameters of three devices for different number of TiO₂ deposited collected after a mechanical stressed was applied.

Layers number	J _{sc} [mA/cm ²]	V _{oc} [mV]	FF [%]	η [%]
2	1.26 ± 0.08	724 ± 23	48 ± 6	0.38 ± 0.11
3	1.3 ± 0.6	672 ± 2	57 ± 8	0.51 ± 0.32
4	2.6 ± 0.9	680 ± 7	56 ± 1	0.73 ± 0.32
5	1.6 ± 0.2	665 ± 39	60 ± 7	0.52 ± 0.28
6	0.9 ± 0.3	666 ± 6	62 ± 5	0.41 ± 0.08

What immediately stands out by looking at the J-V curves for all the different thicknesses, and at the relative PV values reported in the tables above, is the reduction in efficiency related to the decrease in the generated photocurrent after the mechanical stress has been applied.

This is due to damages in the TiO₂ coating of photoanodes deriving from the stress. As a consequence, detachment of part of the oxide layer and thus a decrease in amount of loaded dye and injected electrons, or in general the formation of cracks within the coating which reduce the electronic conductivity necessary to the photogenerated electrons to travel till the conductive substrate (Ti-wire), are produced.

If we consider the trend of PV performances with the change in thickness, it is possible to notice as these results corroborate what seen at the beginning of this section. As previously demonstrated, with an increase number of deposited layers, more dyes molecules were adsorbed on the photoanodes surface, until a maximum amount is reached. However, with the increased thickness, photo-generated electrons require a longer path to reach the conductive substrate, thus there is a higher probability of electrons recombination. This effect is clearly shown in *Figure 6.14* where the short circuit density (J_{sc}) is reported as a function of coating thickness (i.e. number of layers). The results show the presence of an optimal thickness (4 depositions, 10 μm), after which the photo-current produced starts decreasing. Despite the almost constant amount of adsorbed dye after 4 depositions (*Figure 6.11*), the increment of the layers number causes an increased electrons recombination with the electrolyte and thus a decrease in the current density.

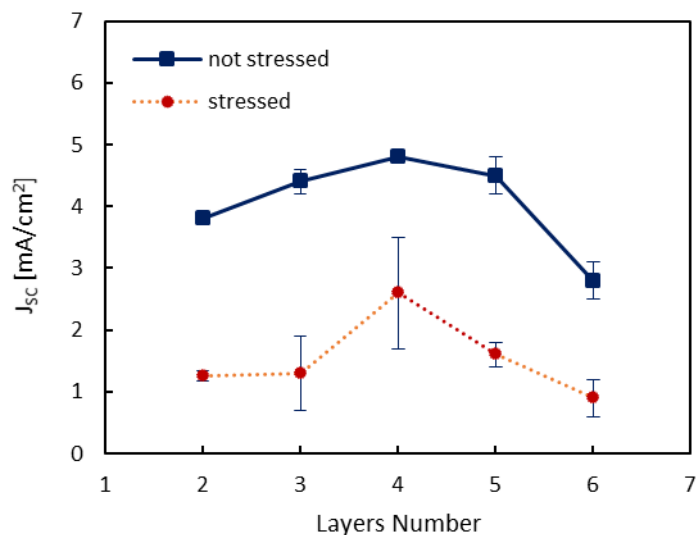


Figure 6.14. Short Circuit current density as function of number of deposited TiO₂ layers.

During their transport through the mesoporous TiO₂ film in fact, electrons are always within only few nanometres distant from the interface between the semiconductor and the electrolyte [8]. This means a higher probability of recombination with electrolyte species with the increase in transport path and therefore Titania thickness.

In order to explain in more details the recombination processes that occur inside high thickness TiO₂-based Fibre-shaped DSSCs, dark current analyses were done on three samples taken as models for different numbers of depositions (*Figure 6.15*).

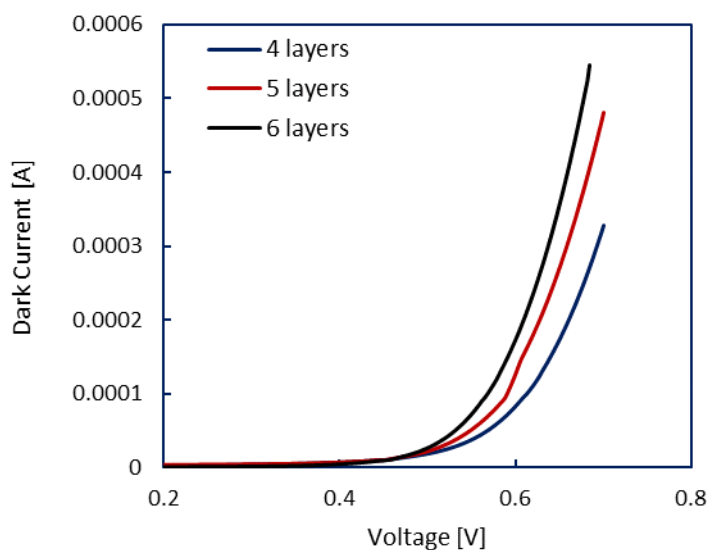


Figure 6.15. Current-Voltage curves registered under dark condition for different number of TiO₂ depositions

Under dark conditions, scanning from zero to positive potentials, the current generated cannot be due to the sensitizers. It is in fact the donor species of the electrolyte (which are more abundant in common electrolyte compared to acceptor species, *i.e.* concentration of I^- compared to I_3^-) responsible for the transfer of electrons to the photoanode [1]. Basically, this current quantifies the electron recombination between the photoanodes and the electrolyte. In particular, dark current increases up to a limiting value is reached, called Dark Saturation Current (I_{dark}^0) or Current Density (J_{dark}^0). As reported in literature [9], when electron transport path increases (*i.e.* increased TiO_2 thickness) the Dark Saturation Current Density will increase consequently.

As shown in *Figure 6.11*, between depositions 4 and 6 the amount of dye is constant (*i.e.* constant value of injection current, J_{inj}), and the recombination process increases (*i.e.* J_{dark} increases), as demonstrated by the I-V curves in *Figure 6.15*. The resultant photo-current density (J_{ph}) decreases as described by the simple relation:

$$J_{\text{ph}} = J_{\text{inj}} - J_{\text{dark}}$$

The dark current analyses confirm therefore, the presence of a high number of recombination process inside the DSSCs based on thick photoanode. The same relative trend in J_{SC} is maintained after the mechanical stress was applied, as previously described. It has to be noted that the high values of the associated standard deviations are a consequence of the intrinsic nature of the fracture mechanism of ceramic materials (*i.e.* brittle fracture) which occurs owing to the presence of defected zones that cannot be the same for all the devices.

Moreover, the deformation was applied manually, as shown in *Figure 6.12*, and for that reason small differences of stress application may had led to slightly different results.

Figure 6.16 presents the average open circuit voltage values as a function of coating thickness. What obtained is similar to what found by Wu *et al.* for a Bi-doped TiO_2 nanofibers-based planar DSSC [10].

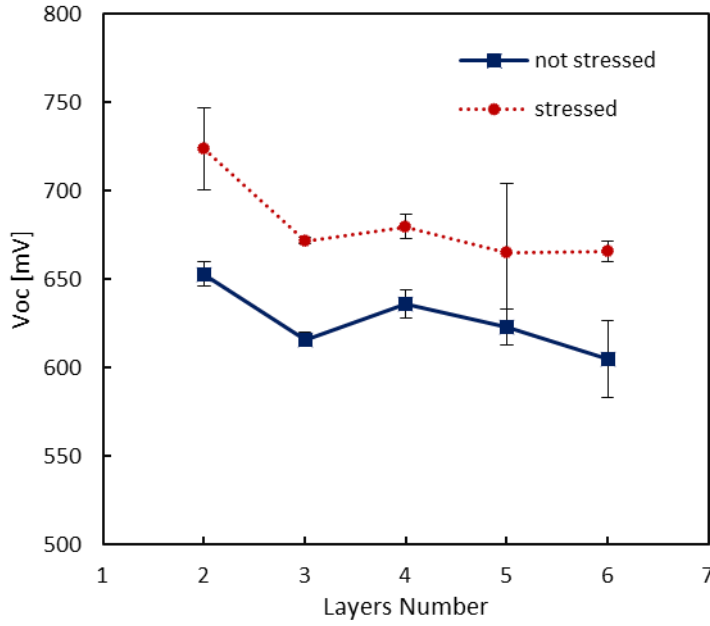


Figure 6.16. Open circuit Voltage for different number of TiO₂ depositions.

There is a clear general trend of decreasing V_{OC} with the increase of coating thickness. This is consistent with literature [11],[9] and, as seen before, it can be explained on the basis of electron recombination and dark saturation density current.

It is generally known that a DSSC behaves like a diode when no light is applied [12],[13]. In this case, the open circuit voltage of the cell can be derived from the Shockley diode equation by setting the net current equal to zero (open circuit condition), and it is described by:

$$V_{OC} = \frac{nkT}{e} \ln \left[\frac{J_{ph}}{J_{dark}^0} \right] + 1$$

where n is the ideal coefficient, k is the Boltzmann constant, T is the temperature, e is the electron charge and J_{ph} and J_{dark}^0 are photocurrent density and dark saturation current density discussed above. The equation shows that V_{OC} is inversely proportional to the dark saturation current density, which increases, with thick TiO₂ coating. This explains the slight decrease in open circuit voltage registered with the increase in thickness. More interesting and unusual is the increase in V_{OC} for every samples after the mechanical stress was applied. The reason for this is not clear and no similar reference have been found in literature. A higher open circuit voltage cannot, this time, be correlated to a

lower probability of electron recombination with the electrolyte (*kinetic explanation*), especially because of the resulting cracking of the coating that causes a close contact between TiO₂ and the oxidized species in the electrolyte. The morphological differences of FDSSCs photoanode before and after mechanical stress are reported in *Figure 6.17*.

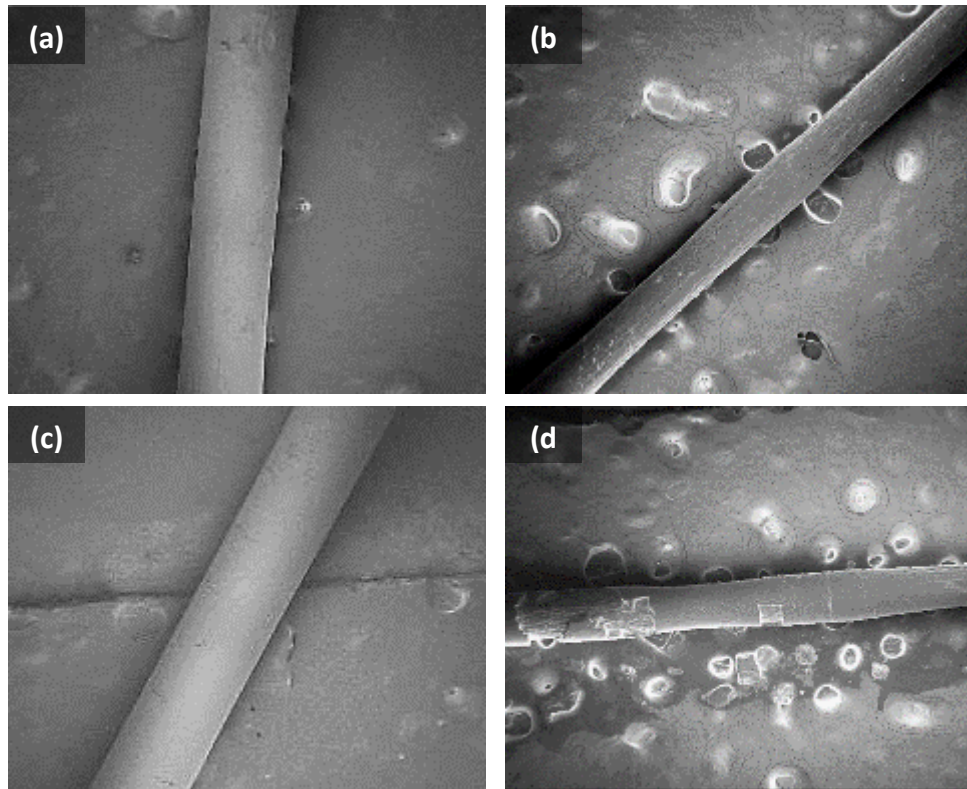


Figure 6.17. SEM images of 2 and 3 layers photoanodes before (a, c) and after (b, d) the applied stress.

A possible explanation may be related to the definition of the V_{oc} itself, *id est*, the potential difference between the Fermi Level of the electrons in the TiO₂ and the redox potential of the electrolyte (*thermodynamic explanation*). Because the electrolyte remains the same, this effect can be linked to a shift of TiO₂ conduction band towards more negative values caused by the mechanical stress applied. Yin *et al.* have demonstrated that TiO₂ in the anatase phase, because of its layered structure with soft direction perpendicular to the layer plane, has a band gap that can be tuned efficiently by applying stress [14]. Moreover, the mechanical deformation applied may have caused a modification in the structure of the sintered TiO₂ nanoparticles with a consequent reduction of particles size due to the coating disaggregation and a consequent increase in

E_g as suggested by literature [15]. Further work needs to be carried out to explain this behaviour.

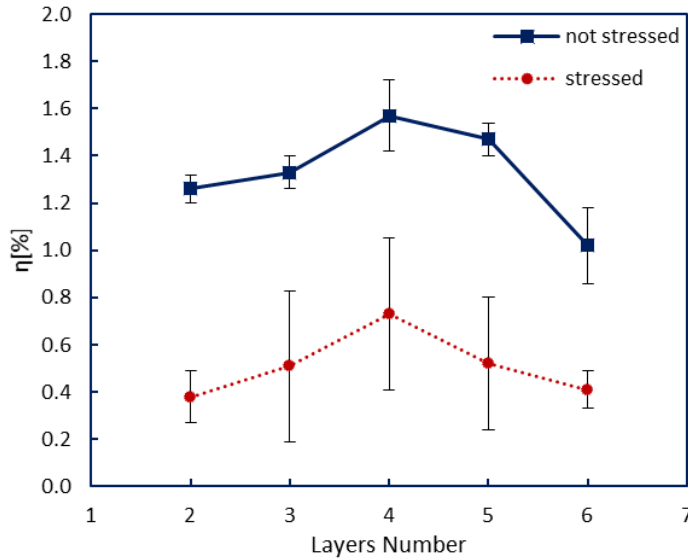


Figure 6.18. Average efficiency values for different number of TiO_2 deposition.

Other than current density, power conversion efficiency (η) is the other photovoltaic parameter strictly dependent on the amount of absorbed dye, and thus on the photocurrent produced. For this reason, the trend observed for the conversion efficiency (Figure 6.18) is comparable with the one obtained for the photocurrent density. The presence of an optimal thickness is observed, which corresponds to the same number of deposition that lead to the highest value of short circuit density, in agreement with other works in literature[10],[16]. The effect of a slightly decrease in V_{OC} with an increase in in TiO_2 thickness, does not influence at the same level the efficiencies of the cells. FF finally, shows no significant correlation with the thickness of mesoporous TiO_2 , in accordance with other works in literature [10]. This may be due to the high number of variables, which concur all together in defining this value (see section 2.2.1.3 and 5.8.4):

$$FF = \frac{P_{max}}{I_{SC} \cdot V_{OC}} = \frac{I_{max} \cdot V_{max}}{I_{SC} \cdot V_{OC}}$$

From this point, considering that all the following results concerning the PV parameters after the applied stress are in line with what have been just described, *i.e.* lower values of J_{SC} and η , and higher values of V_{OC} , J-V curves of stressed devices will be reported without be commented any further.

In order to better investigate the charge transfer dynamics at the basis of the obtained results, electrochemical impedance spectroscopy (EIS) analyses were performed on these systems. Spectra were recorded at open circuit potential (OCP) under 1 sun illumination condition. The resulting Nyquist plots are reported in *Figure 6.19*.

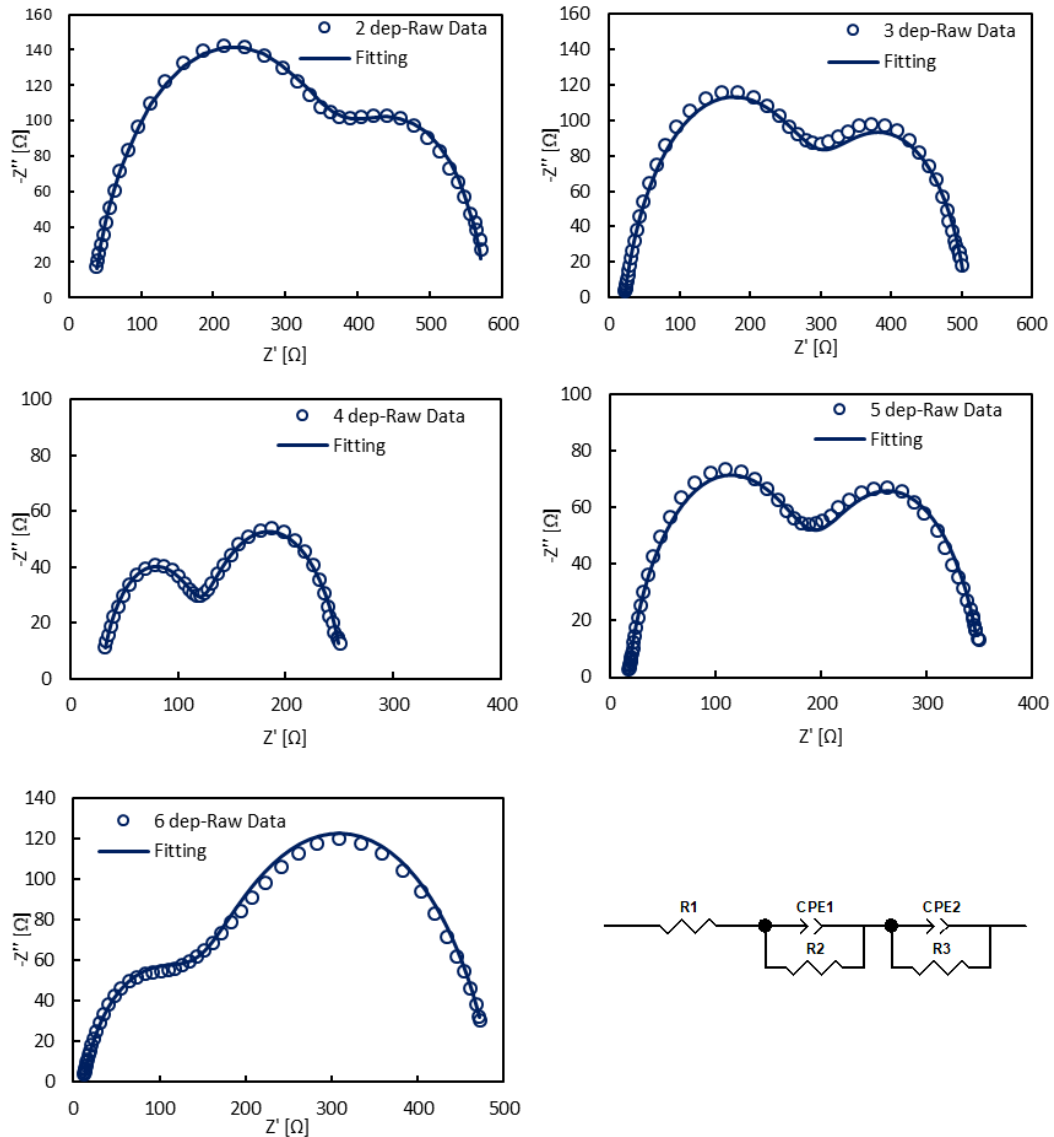


Figure 6.19. Nyquist Plot of one sample for each number of depositions (*dep*) measured at open circuit potential, 1 sun illumination, and equivalent circuit used to fit the spectra.

The data for all cells could be well-fitted by the equivalent circuit model reported in *Figure 6.19* where R_1 stands for the counter electrode resistance, R_2 and CPE_1 , in the first Voigt element (*i.e.* the part of the circuit constituted by the parallel of a resistance – charge transfer resistance – and a capacitor – double layer resistance [17]), represent

parameters electrolyte-related, and finally, R_3 and CPE_2 in the second Voigt element, are related to the photoanode, and thus the parameters taken into account. R_3 is representative of TiO_2 charge transfer resistances, the constant phase element, a generalization of the conventional capacitance used because of the presence of a porous interfaces [17] and the relative capacitance value associated, represents the capacitance of the sensitized layers. These values related to the TiO_2 /dye/electrolyte interface are reported in *Table 6.8*, [18][19].

Table 6.8. Resistance values (R_3) and capacitance values (C_2) associated with the photoanode for different number of depositions.

number of layers	R_3 [Ω]	C_2 [F]
2	203	0.102
3	190	0.119
4	133	0.134
5	158	0.135
6	341	0.055

As it can be seen from the table above, charge transfer resistance values follow the trend of J_{SC} obtained by J-V curves: the resistance of the samples decreases with the increase in the number of depositions between two and four, indicating an enhancement in the conducting behaviour because of a higher amount of adsorbed dye. From that point, the amount of dye does not increase with respect to the mass and thickness of the coating, resulting in a higher resistivity. Also, the capacitance values of the sensitized layers are in good agreement with what have been said, with high C values corresponding to high amount of adsorbed dye, and high η .

From J-V measurements and EIS analyses, we can conclude that the optimal coating thickness for short FDSSCs (3.5 cm), in terms of current density produced and overall efficiency is the one corresponding to four depositions (around 10 μm). However, considering the increase in coating fragility related to thick systems (*Figure 17* and *Figure 20*), despite the highest efficiencies obtained for these systems, they do not represent a valid option for flexible DSFFs.

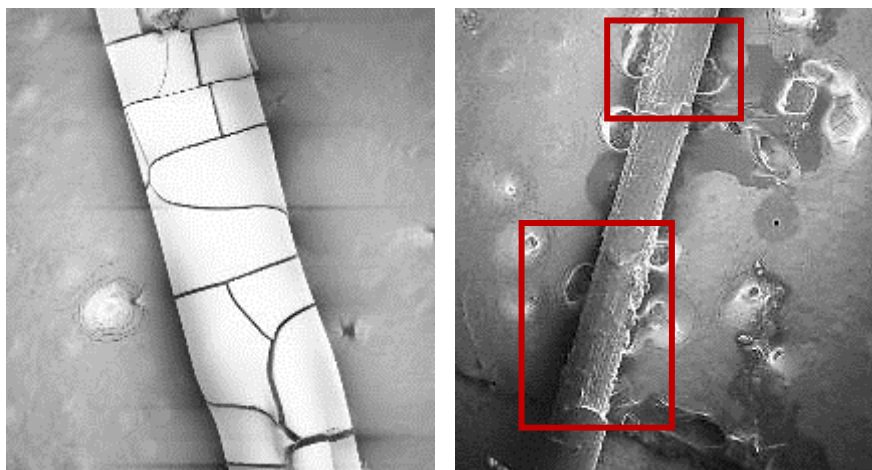


Figure 6.20. SEM frontal image of 5 depositions photoanodes before (left) and after (right) the applied stress. It is visible how the mechanical deformation caused a partial destruction of the coating with clearly missing coating pieces (circled in red).

Considering the general trend to move the new technologies towards thin layers devices, the two depositions-based DSSCs that show efficiency not far from what shown by the 4 layers ones, represent a potential alternative for highly-stable flexible device.

6.4. Influence of the electrolyte on the photovoltaic performances of TTZ5 – based fibre DSSCs

Having optimized the photoanodes thickness the following part of the work was focused on the determination of the electrolytic system which could allow the best photovoltaic performances. The electrolyte is in fact, the other crucial component in a DSSC system, being responsible for the inner charge carrier transport between electrodes, for the continuous regeneration of the dye, and for the determination of the open circuit voltage, which in turn, has a great influence in defining the efficiency of the cells [20].

6.4.1. Comparison between I/I_3^- and $[Co(bpy)_3]^{3+/2+}$ – based electrolytes

The classic electrolytes composed by the redox couple I/I_3^- was compared to the electrolyte based on polypyridine cobalt complexes that is less aggressive, and with high redox potential which should lead to a higher V_{OC} and fast dye regeneration (Figure 6.21).

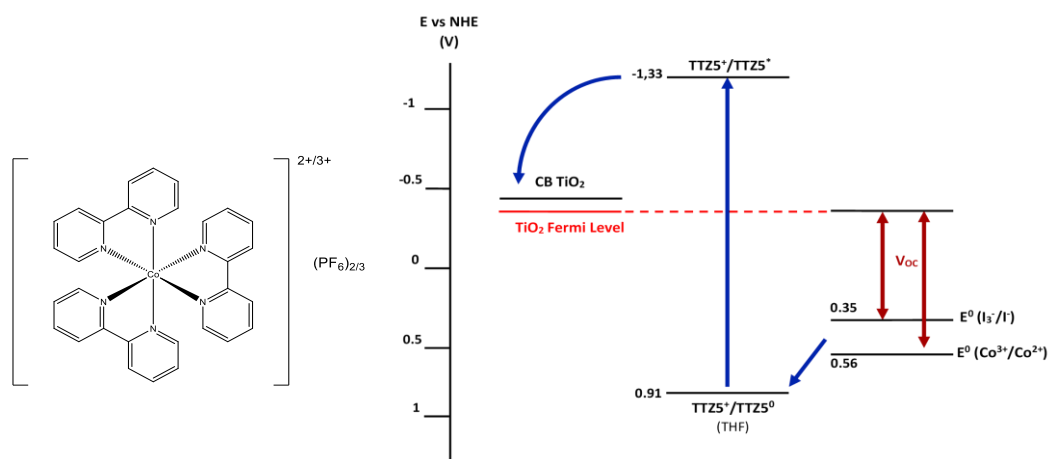


Figure 6.21. Chemical structure of $[\text{Co}(\text{bpy})_3]^{3+/2+}(\text{PF}_6)_{2/3}$ and schematic representation of the energetic diagram of the studied system.

Fibre-shaped DSSCs based on 2 depositions TiO_2 photoanode were prepared and tested. *Figure 6.22* shows the J-V curves obtained for the different redox-couple systems, whose relative photovoltaic parameters are reported in *Table 6.9* and *Table 6.10*.

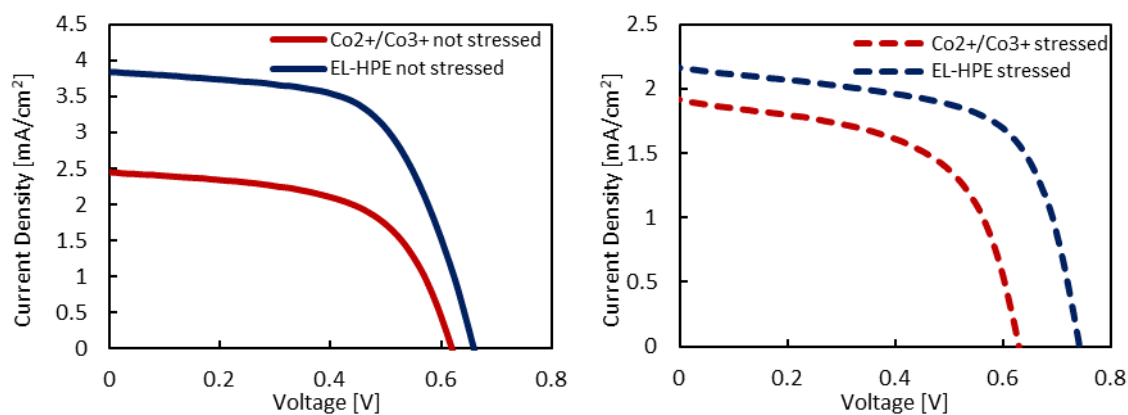


Figure 6.22. J-V curves of TiO_2 -TTZ5 based fibre-shaped DSSCs with different liquid electrolytes.

Table 6.9. Photovoltaic parameters of FDSSCs using EL-HPE (I_3^-/I^- redox couple) as electrolyte.

	J_{SC} [mA/cm^2]	V_{OC} [mV]	FF [%]	η [%]
not stressed	3.8 ± 0.1	641 ± 7	48 ± 5	1.26 ± 0.06
stressed	1.26 ± 0.08	724 ± 23	48 ± 6	0.38 ± 0.11

Table 6.10. Photovoltaic parameters of FDSSCs using $[\text{Co}(\text{bpy})_3]^{3+/2+}$ – based electrolyte.

	J_{SC} [mA/cm^2]	V_{OC} [mV]	FF [%]	η [%]
not stressed	2.23 ± 0.32	606 ± 18	56 ± 3	0.80 ± 0.14
stressed	1.72 ± 0.32	609 ± 27	57 ± 1	0.60 ± 0.14

Considering this FDSSCs set up, the redox couple I^-/I_3^- still results the best option in terms of all the principal photovoltaic parameters. Lower values of current density could be related to the absorption of the cobalt-based electrolyte at the same wavelength of the TTZ5, as shown in *Figure 6.23*, which lead to a reduced amount of light available for dye excitation and therefore to decreased photoinduced current.

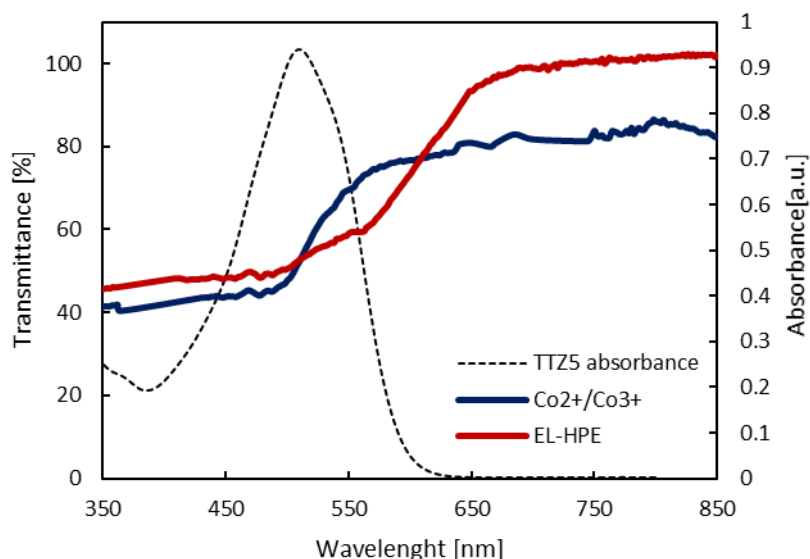


Figure 6.23. UV-Vis spectra of the systems electrolyte-PTFE tube for both liquid electrolytes (solid line) and TTZ5 in THF (dotted line).

Moreover, generally inferior performance of Co(III)/Co(II) redox shuttles with some dyes compared to the ones obtained with I^-/I_3^- were attributed, in literature [21], to an inhibited effect of Co^{2+} caused by ions pairs formed between Co^{3+} and negative charged sensitizer molecules, with a consequence retarded regeneration.

It was also suggested that ion-pair formation may increase the probability of intercepting TiO_2 electrons and consequently decrease the charge collection efficiency and limit the measured photocurrent and voltage [22]. This could be the reason of the lower open

circuit voltage registered for our system, despite the more positive redox potential of $[\text{Co}(\text{bpy})_3]^{3+/2+}$.

Another plausible explanation could be the steric encumbrance of TTZ5, which may lead to a difficult approach of the bulky $[\text{Co}(\text{bpy})_3]^{2+}$ to the inner photoanode sensitized macropores compared to the much smaller I^- and thus to a less efficient dye regeneration.

6.4.2. Quasi-solid TTZ5/ $(\text{I}^-/\text{I}_3^-)$ – based fibre DSSCs

The best electrolytic system previously identified (I^-/I_3^- - EL-HPE) is not suitable for portable applications, for this reason, the second part of the study was focused on the gelation of such electrolyte. Although the efficiencies reachable using quasi-solid state electrolytes are often lower than those obtained with liquid systems, gel electrolytes are viable alternatives because of the higher stability and better sealing [20], especially important for fibre-shaped DSSCs and their wearable purpose. There are different methods often used for preparing quasi-solid electrolytes. For liquid electrolytes the gelation can be performed through the employ of polymer gelators, or through the help of inorganic agents, such as SiO_2 or nanoclay powder. In this work a comparison between PMMA-based gelation (polymeric gelation) and SiO_2 nanoparticles based-gelation was made in order to define the best alternative for the optimized system (*i.e.* 2 and 4 TiO_2 depositions). The optical properties of the different quasi-solid electrolytes are reported in Figure 6.24.

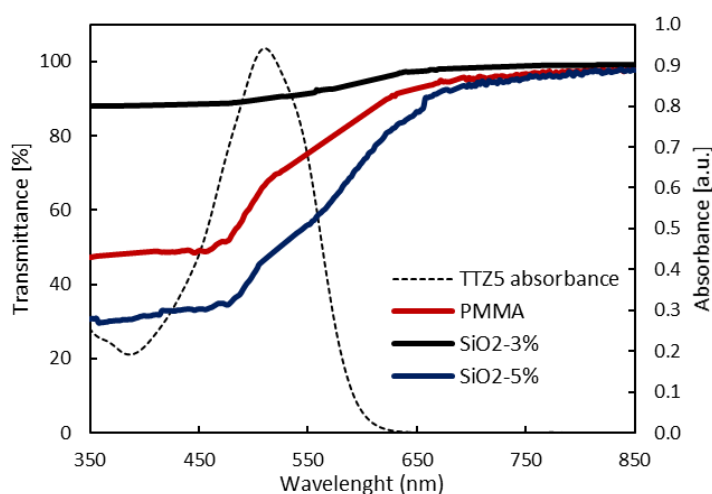


Figure 6.24. UV-Vis spectra of the systems gel-electrolyte-PTFE tube for quasi-solid electrolytes (solid line) and TTZ5 in THF (dotted line).

The transmittance spectra indicate that the inorganic-based gel electrolyte with a lower percentage of silica does not exhibit a significant absorption in the range characteristic of TTZ5, while at higher SiO₂ loading, the inorganic quasi-solid electrolyte shows as expected, a greater absorbance (*i.e.* lower transmittance). The PMMA one behaves similarly to the former. Having characterized the gel-state electrolytes, the devices were produced and tested. Only the PMMA-based DSSCs could be measured due to the impossibility of filling the small diameter PTFE tubes with the inorganic quasi-solid electrolytes. As shown in *Figure 6.25*, the inorganic nanoparticles remained blocked in the initial zone of the tubes, not allowing the subsequent filling of the devices.

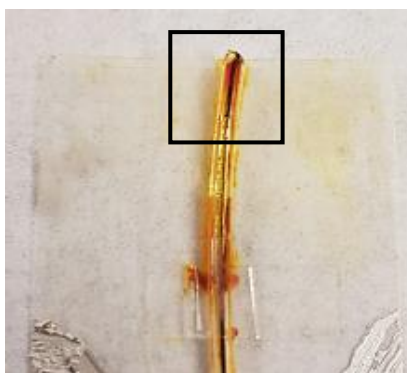


Figure 6.25. SiO₂ nanoparticles stuck at the initial part of the cell preventing the device filling.

No problems were encountered, on the contrary, in the assembly of polymeric electrolyte-based fibre DSSCs, where the gel-state was obtained *in situ*, simplifying the devices filling. PV parameters for PMMA-based quasi-solid fibre DSSCs with 2 and 4 numbers of deposited TiO₂ layers are reported in *Table 6.11* and *Table 6.12*. The J-V curves from which they have been extrapolated are shown in *Figure 6.26*.

Table 6.11. Average photovoltaic parameters for three devices, 2 and 4 TiO₂ depositions, employing liquid electrolyte (EL-HPE.)

		Jsc [mA/cm²]	Voc [mV]	FF [%]	η [%]
2 layers	not stressed	3.80 ± 0.10	641 ± 7	48 ± 5	1.26 ± 0.06
	stressed	1.26 ± 0.08	724 ± 23	48 ± 6	0.38 ± 0.11
4 layers	not stressed	4.8 ± 0.1	636 ± 8	51 ± 6	1.57 ± 0.15
	stressed	2.6 ± 0.9	680 ± 7	56 ± 1	0.73 ± 0.32

Table 6.12. Average photovoltaic parameters for three devices, 2 and 4 TiO₂ depositions, employing PPMA-based gel-state electrolyte (EL-HPE).

		J _{sc} [mA/cm ²]	V _{oc} [mV]	FF [%]	η [%]
2 layers	not stressed	7.2 ± 1.4	690 ± 5	26 ± 1	1.29 ± 0.20
	stressed	1.72 ± 0.32	716 ± 9	38 ± 5	1.26 ± 0.68
4 layers	not stressed	7.31 ± 0.63	672 ± 14	28 ± 2	1.36 ± 0.20
	stressed	3.19 ± 0.40	709 ± 36	42 ± 4	0.95 ± 0.02

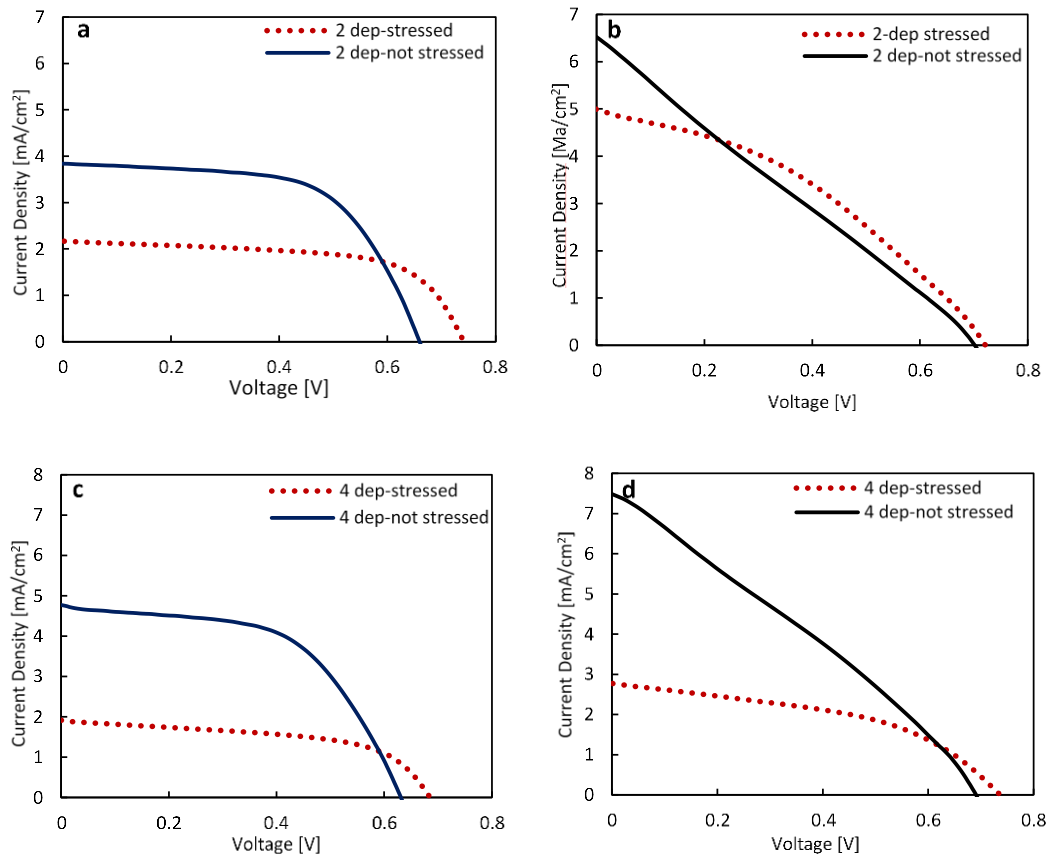


Figure 6.26. J-V curves for 2 and 4 depositions (dep) liquid-based FDSSCs (a,c) and for 2 and 4 depositions gel-state FDSSCs (b,d).

As it can be seen from the relative photovoltaic parameters, quasi-solid devices gave almost double values of J_{SC}, and high open circuit potentials compared to liquid-based devices but much lower fill factors that lead to power conversion efficiencies comparable with liquid electrolyte-based devices.

6.5. Long fibre DSSCs

For practical purpose, it is important to fabricate wearable working devices, able to adapt to a variety of curved surfaces like our bodies [23]. Moreover, it becomes necessary to have higher active areas to balance the generally low efficiency of these devices. To satisfy these demands, long fibre-shaped dye sensitized solar cells need to be assembled. For this reason, 10.0 cm fibre DSSCs were produced and tested with liquid and gel-state electrolytes, to verify the influence of device length on operation and photovoltaic performances of the cells.

6.5.1. Liquid TTZ5/(I⁻/I₃⁻) – based long fibre DSSCs

At first liquid electrolyte-based cells were tested. Photoanodes were fabricated as previously described and based on 2 and 4 layers of TiO₂ in order to verify if the results obtained for short devices could be applied to longer cells (*Figure 6.27*). Table 6.13 shows photovoltaic parameters extrapolated from J-V curves (*Figure 6.28*) for long FDSSCs.



Figure 6.27. Long FDSSC used in this part of the work, for liquid electrolyte.

Table 6.13. Average photovoltaic parameters of three long devices tested with liquid EL-HPE and for different numbers of deposited TiO₂ layers.

		Jsc [mA/cm ²]	Voc [mV]	FF [%]	η [%]
2 layers	not stressed	3.18 ± 0.40	636 ± 17	61 ± 4	1.23 ± 0.04
	stressed	2.30 ± 0.30	669 ± 19	67 ± 4	1.06 ± 0.04
4 layers	not stressed	1.99 ± 0.05	599 ± 10	64 ± 1	0.76 ± 0.01
	stressed	1.11 ± 0.13	607 ± 4	59 ± 6	0.40 ± 0.08

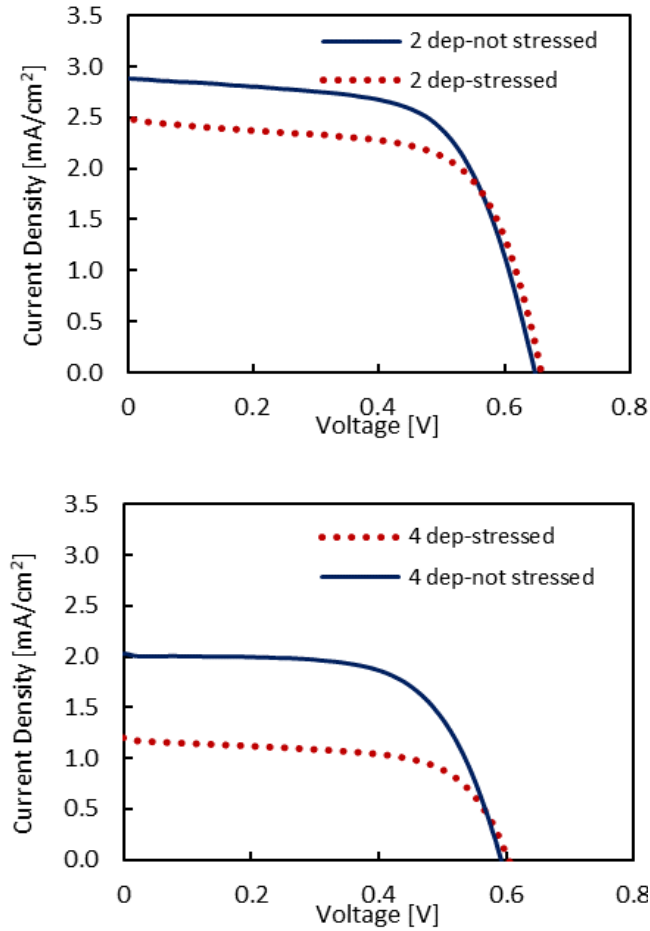


Figure 6.28. J-V curves for 10 cm FDSSCs tested with liquid EL-HPE for 2 and 4 depositions (dep) photoanodes.

The results show that the best average photovoltaic performances were found for photoanodes with a thinner Titania coating (5 μm), in contrast with the results attained for shorter devices. This can be reconducted to the higher probability of having coating defects (*i.e.* fragility of the coating) for long devices with respect to short cells with the same number of deposited TiO_2 layers, and thus less efficient devices. As prove of the coating fragility, photovoltaic performances of stressed devices decrease more for thicker photoanodes than for thin ones.

Interestingly, short circuit current densities and efficiencies obtained for thin layer long devices are comparable with ones obtained for short fibre DSSFs previously tested (J_{sc} 3.8 mAcm^{-2} , η 1.26 %) confirming that what seen for short cells can be translate to long devices in the absence of any factor which may affect the integrity of the devices (*i.e.* coating defects). EIS analyses (*Figure 6.29*) confirmed the results reported above.

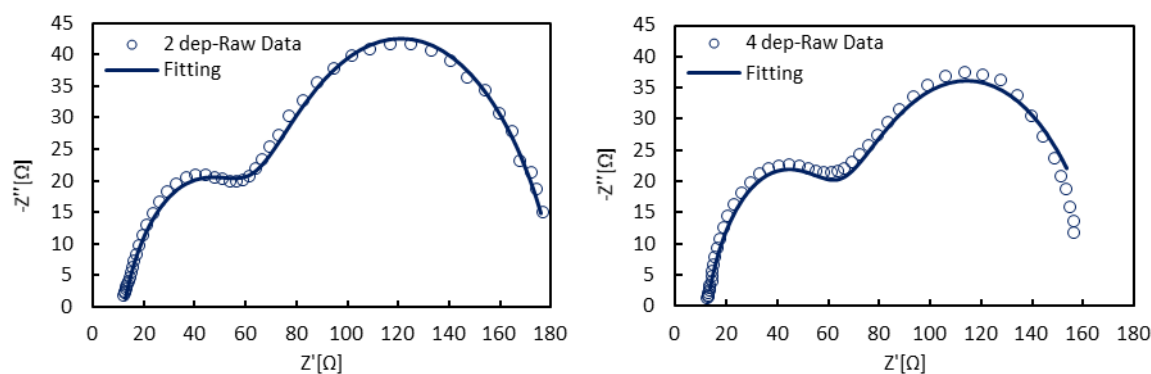


Figure 6.29. Nyquist Plot of one sample (10 cm) for each number of depositions (*dep*).

As it can be seen from *Table 6.14* looking at the Titania coating charge transfer resistances (R_3) and capacitance values (C) associated with the sensitized layers obtained from EIS, thin coating devices showed better electron transfer capacity and power conversion efficiency. The equivalent circuit used to fit the raw data was the same previously applied (*Figure 6.19*).

Table 6.14. Resistance values (R_3) and capacitance values (C_2) associated with 10 cm photoanodes for different number of depositions.

number of layers	R_3 [Ω]	C_2 [F]
2	102	0.230
4	121	0.18

As demonstrated, 2 deposition-based photoanodes represent the optimal choice for long fibre DSSCs, therefore further investigations on 10.0 cm systems were conducted using this optimized photoanodes thickness.

6.5.2. Quasi-solid TTZ5/(I/I₃⁺) – based long fibre DSSCs

Gel state EL-HPE electrolyte (PMMA) was applied to optimized long FDSSCs system (TiO₂ thickness equal to 5 μm – *Figure 6.30*). As shown by J-V measurements (*Figure 6.31*) and by the extrapolated photovoltaic parameters in *Table 6.15*, similarly to what had been obtained for short devices, quasi-solid long fibre DSSCs with the same

photoanode thickness, obtained much higher short circuit current value and higher open circuit potential.



Figure 6.30. Long quasi-solid FDSSCs prepared.

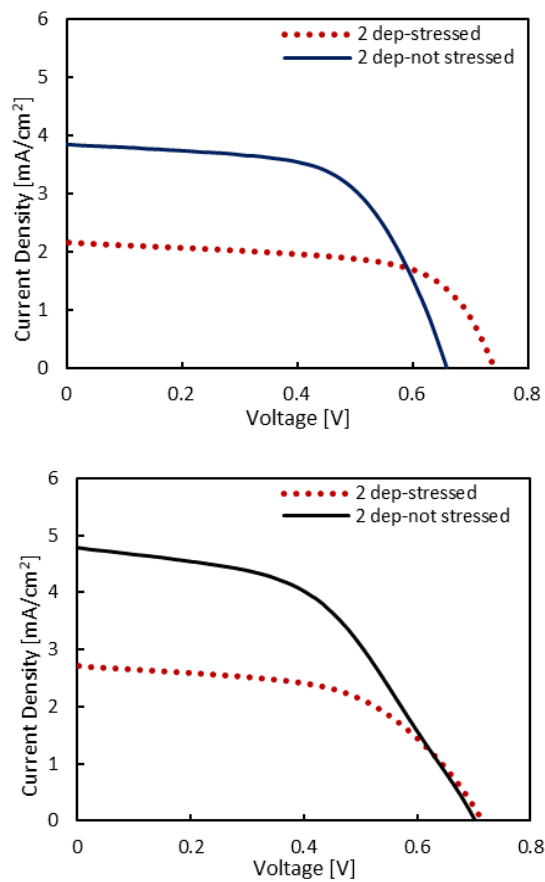


Figure 6.31. J-V curves for 2 depositions (dep) liquid-based (top) and gel-state (bottom) long system DSSCs.

Table 6.15. Average photovoltaic parameters for three long devices, 2 depositions, for liquid and gel state EL-HPE.

		J_{sc} [mA/cm²]	V_{oc} [mV]	FF [%]	η [%]
liquid EL-HPE	not stressed	3.18 ± 0.40	636 ± 17	61 ± 4	1.23 ± 0.04
	stressed	2.30 ± 0.30	669 ± 19	67 ± 4	1.06 ± 0.04
gel EL-HPE	not stressed	4.90 ± 0.64	689 ± 12	50 ± 5	1.67 ± 0.07
	stressed	2.61 ± 0.18	697 ± 20	57 ± 2	1.03 ± 0.06

Moreover, unlike for short devices, fill factor values, although lower than liquid-based FDSSCs ones, could be considered acceptable. For this reason, efficiency associated with quasi-solid devices were even higher than for liquid-state electrolyte. This result is significantly important considering the number of practical benefits, which derive from employing quasi-solid-state electrolytes. More analyses, such for example EIS measurements, could be performed to better investigate the reason for what has been found.

6.6. Towards metal free fibre DSSCs

6.6.1. Pt free TTZ5-based DSSCs

In the development of DSSCs challenging issues are not only to achieve a high η, but also to mould devices in flexible structures, significantly reducing their fabrication costs. From this point of view, platinum is an expensive noble metal, not stable in presence of the highly corrosive I⁻/I₃⁻ electrolyte and is rare on earth, thus making the large-scale application of these cells impractical [24]. Therefore, its substitution with cheaper materials is essential to cost-down the commercialization of solar cells device. Moreover, considering the ultimate goal for these solar cells, which is the integration in clothes to work as power sources for wearable electronics, it is necessary the use of fibres which result comfortable for our body. For these reasons, in this part of the work, three different PPy-coated fibres (Kevlar, viscose and cashmere), made conductive for polypyrrole (PPy) coating, obtained by in situ chemical oxidative polymerisation were used as alternative counter electrodes to fabricate Pt free TTZ5-based fibre dye-sensitized solar

cells. In *Figure 6.32* SEM images of the fibres at different magnification are reported. PPy has been successfully deposited on the fibre surfaces.

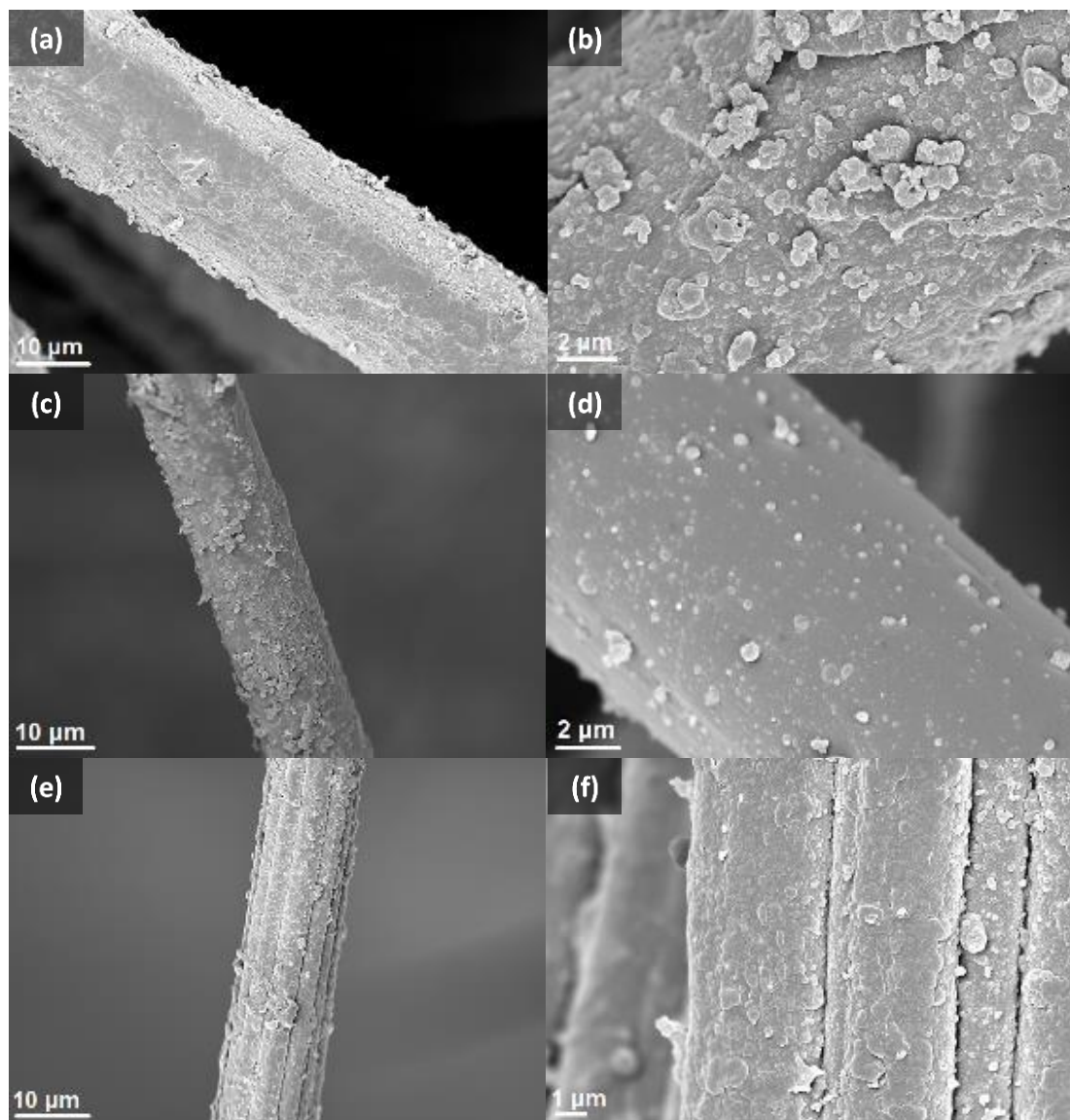


Figure 6.32. SEM images of cashmere (a, b), kevlar (c, d), viscose (e, f) fibres coated with PPy with low and high magnification.

The typical scale of cashmere [25] are, in fact, not visible anymore, and PPy nodules are present on the surface of all the samples as a result of surface deposition of PPy formed in the bulk of the polymerisation bath at prolonged polymerisation time [26].

6.6.1.1. Electrochemical characterization

The counter electrode (CE) plays an important role in collecting electrons from outer circuits and in regenerating the redox couple. Hence, CE materials with high conductivity and electro-catalytic performance towards I^-/I_3^- are desirable [27]. CV was performed to characterize the catalytic activity of the PPy coated fibres over the $I_3^-/3I^-$ electrolyte solution which mimed the commercial electrolyte EL-HPE (10 mM LiI, 1 mM I_2 , 0.1 M $LiClO_4$ in ACN) using a three-electrode system (Figure 6.33).

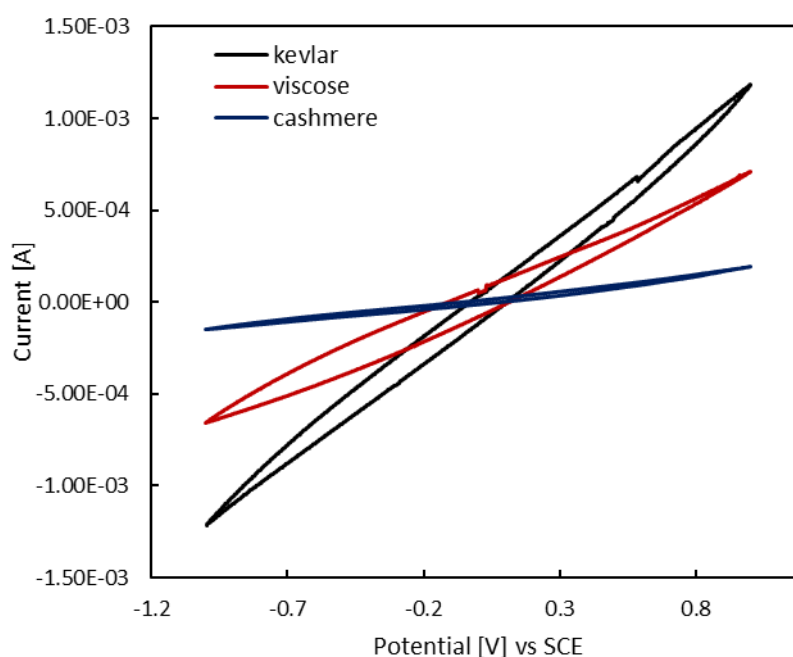
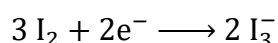
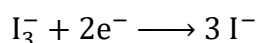


Figure 6.33. Cyclic voltammograms of PPy-coated fibres in a 10 mM LiI, 1mM I_2 , 0.1 M $LiClO_4$ ACN solution registered at a scan rate of 100 mV/s.

As it shown, none of the systems present the pairs of faradic peaks expected, related to the transfer of two electrons shown in the following reactions:



the first of which, the reduction of I_3^- to I^- , is important for the device performances [28] because necessary for the regeneration of the redox couple. This is mainly due to the high

values of linear resistance measured for the polypyrrole-coated fibres (*Table 6.16*), hence to their low conductivity [29].

Table 6.26. Linear resistivity values and accumulation capacitance values of PPy-coated fibres.

fibre	ρ_L [kΩ/cm]	C [mF]
Viscose	4.46	0.10
Cashmere	2.64	0.14
Kevlar	0.57	6.50

It was however possible to extrapolate the double layer capacitance of the PPy coating and electrolyte by extrapolating the electrical charge that flow on the samples. The results are reported in the *Table 6.16*. Based on what obtained by voltammetric analysis, Kevlar was chosen, for its higher electrochemical response, to be used as CE for the Pt free fibre DSSCs.

6.6.1.2. Short length Pt-free fibre DSSC

Standard length devices (3.5 cm) with optimized photoanode thicknesses (2 or 4 depositions) were fabricated following the same procedure previously reported and tested with the two different electrolytes (liquid or gel) using larger diameter PTFE tube (diam. 1.58 mm x 3.18 mm), on respect of what previously employed, to be compatible with the thickness of the counter electrodes fibres.



Figure 6.34. Example of a prepared Short Pt free fibre DSSC.

6.6.1.3. Liquid (I^-/I_3^-)-EL-HPE electrolyte

Figure 6.35 shows J-V curves obtained for (Kevlar cathode/2-4 depositions anodes)-based fibre DSSCs tested with liquid EL-HPE electrolyte. The highly dispersed photovoltaic parameters, as indicated by the associated standard deviations, are probably mainly ascribable to the poor conductive properties of the Kevlar – PPy fibers and consequent cells performances.

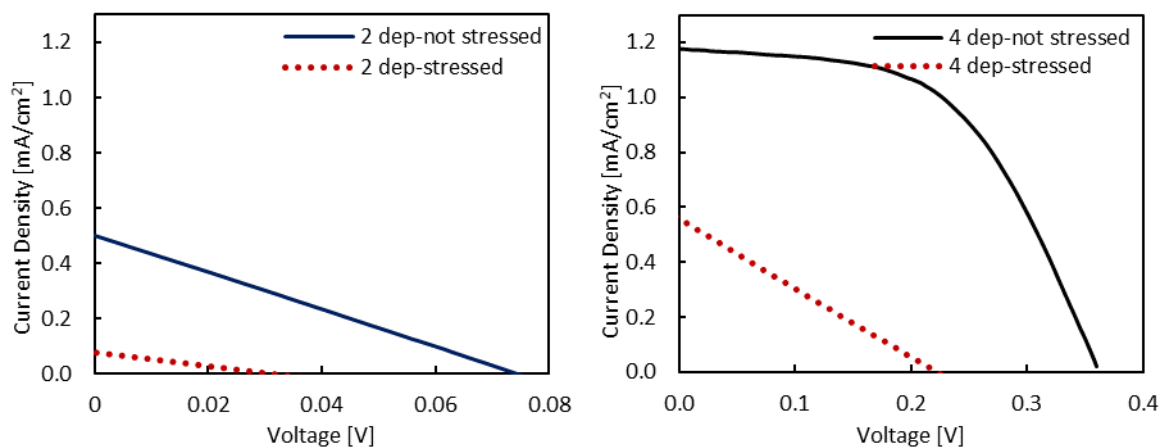


Figure 6.35. J-V curves for 2 and 4 depositions (dep) liquid-based short system fibre DSSCs.

Despite what previously observed for similar systems employing Pt counter electrodes, the obtained results (Table 6.17) clearly demonstrate the much higher efficiency of 4 depositions based photoanodes when PPy-coated Kevlar cathode is used.

The low current densities registered, and the correlated power conversion efficiencies, may be reconducted to the poor conductivity of the fibres and thus to their limited capability of recollecting the photoelectrons generated and of regenerating the electrolyte.

As a consequence, only with thicker electrodes and higher amount of adsorbed dye and generated currents, the values collected are reasonably adequate for a possible future working device.

Table 6.17. Average photovoltaic parameters for three devices, 2 and 4 depositions, tested with Kevlar-based counter electrode and liquid electrolyte.

		J_{sc} [mA/cm²]	V_{oc} [mV]	FF [%]	η [%]
2 depositions	not stressed	0.68 ± 0.60	146 ± 62	33 ± 12	0.03 ± 0.03
	stressed	0.08 ± 0.01	89 ± 80	21 ± 6	0.00 ± 0.00
4 depositions	not stressed	1.07 ± 0.15	355 ± 47	52 ± 8	0.20 ± 0.04
	stressed	0.36 ± 0.28	160 ± 87	24 ± 1	0.02 ± 0.02

As it shown by *Table 6.17*, FF values for the two kind of devices are significantly different from each other, as reflected by the diverse shape of the correlated the J-V curves. Being the Fill Factor related to the series and shunt resistance within the cell [30][31], as demonstrated by several empiric equation in literature [32], the observed behaviour could be attributed to the different electrolyte thickness within the PTFE tube.

As shown by *Figure 6.36*, Kevlar counter electrode is composed by several different single fibres. For this reason, the fibrous nature of the material, considering the photoanode thickness as the only principal different aspect among the devices, may play an important role in determining the space and the homogeneity of the electrolyte layer, *i.e.* the effective distance between the TiO₂ layer and the counter electrode surface.

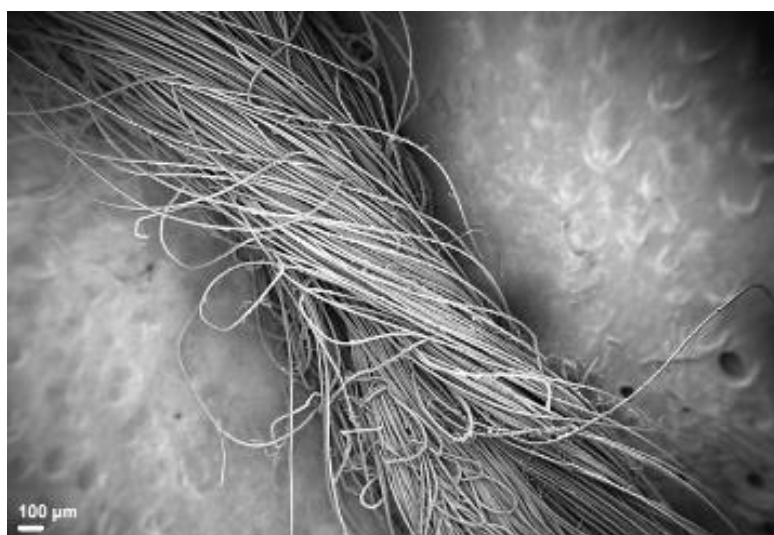


Figure 6.36. SEM image at low magnification of a Kevlar counter electrode.

For the same reason, from a practical point of view, the utilization of Kevlar-based counter electrodes caused several problems with devices filling. Air bubbles were formed during the insertion of the liquid electrolyte during cell assembly, which were difficult to remove.

EIS spectra obtained on the samples are shown in *Figure 6.37*.

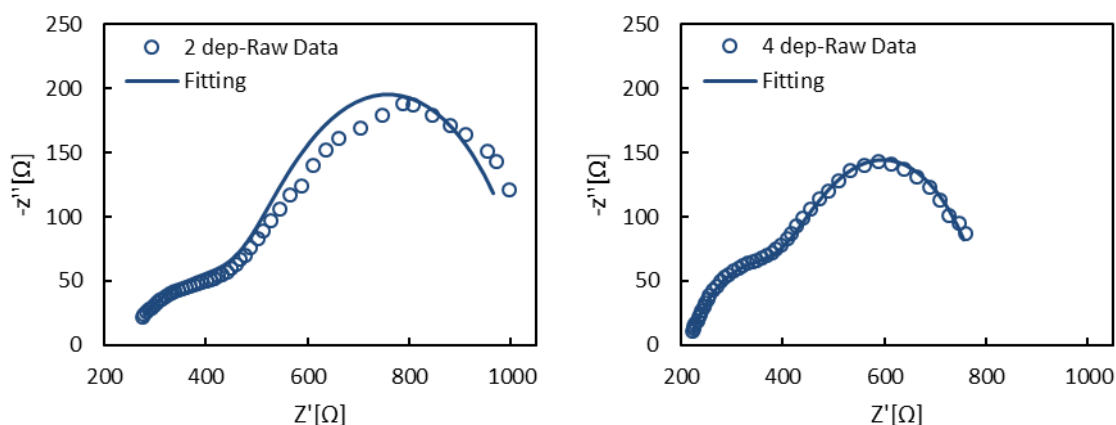


Figure 6.37. Nyquist Plots of a representative sample for 2 depositions (right), and 4 depositions (left) Kevlar-based counter electrode devices.

As it can be observed from the extrapolated values (obtained by the equivalent circuit reported in *Figure 6.19*) reported in *Table 6.18*, there is a significant difference in the R_3 values (related to Titania coating charge transfer resistances) when compared to the correspondent values registered for short devices employing platinum counter electrodes (*Table 6.8*, section 6.3).

Table 6.18. Resistance values associated with the Kevlar-based counter electrodes (R_1), and photoanodes (R_3) for 3.5 cm, EL-HPE electrolyte devices.

number of layers	R_1 [Ω]	R_3 [Ω]
2	238	524
4	213	390

The considerably higher photoanode resistances corroborate the much lower photocurrent values attained from J-V measurements stated above (*Table 6.17*). Moreover, as already reported for Pt-based devices, the decreased resistance with the

increase in the layer thickness is a result of the higher amount of associated adsorbed dye, which causes an enhancement in the conductive behaviour of the photoanode. Taking into account the total internal electrical resistance produced on fibre DSSCs (R_1 parameter in the equivalent circuit reported in *Figure 6.19*), the Kevlar-based photocathodes turned out to be much worse electrodes than the Pt-based ones, whose correspondent resistivity values observed on the Nyquist plots (*Figure 6.20*, section 6.3) were about 50Ω for all the samples. In addition, the higher values of R_1 support the related low conductivity of Kevlar-based electrodes previously reported (*Table 6.16*, section 6.6.1.1).

6.6.1.4. Gel (I/I_3^-)-EL-HPE electrolyte

Gel-state devices (PMMA based electrolyte), for 2 and 4 TiO_2 deposited layer photoanodes employing Kevlar counter electrodes were fabricated and tested. The use of *quasi-solid* electrolyte, as opposed to liquid-system devices, allowed a better filling of the cells. In order to ensure the evaporation of acetone the stuffing of the devices with the electrolytic precursor solution was repeated multiple times as previously indicated in the experimental section. J-V curves for *quasi-solid* devices are reported in *Figure 6.38*, and the correlated photovoltaic parameters indicated in *Table 6.19*.

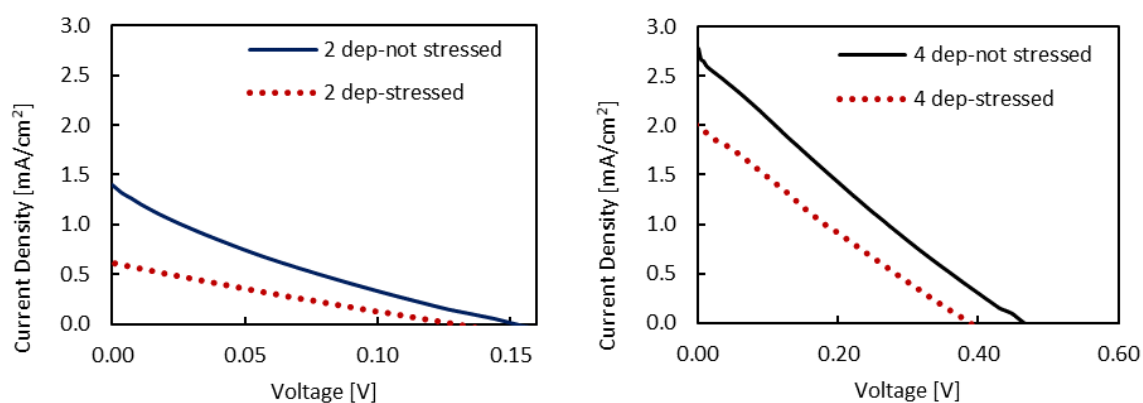


Figure 6.38. J-V curves for 2 and 4 depositions TiO_2 (dep) and Kevlar counter electrodes-gel state electrolyte.

Table 6.19. Average photovoltaic parameters for fibre DSSCs with Kevlar-based counter electrode and gel-state electrolyte

		J_{sc} [mA/cm²]	V_{oc} [mV]	FF [%]	η [%]
2 depositions	not stressed	1.24 ± 0.88	135 ± 25	21 ± 3	0.04 ± 0.02
	stressed	0.56 ± 0.09	125 ± 5	24 ± 1	0.02 ± 0.01
4 depositions	not stressed	2.70 ± 0.66	416 ± 40	21 ± 1	0.20 ± 0.06
	stressed	1.77 ± 0.66	387 ± 65	24 ± 1	0.17 ± 0.08

As already stated for Pt-based devices, PMMA-based *quasi*-solid fibre DSSCs, even in the presence of Kevlar counter electrodes, achieved approximately double values of J_{sc} compared to liquid-based cells. However, the much lower fill factors, probably caused by increased resistive effects in the electrolyte due to the presence of the bulky polymethyl methacrylate molecules, brings to power conversion efficiencies similar to what obtained for the corresponding liquid electrolyte-based devices.

6.6.1.5. Long Pt-free fibre DSSCs

Long devices (10.0 cm) with photoanode thickness suitable for wearable application (2 depositions) were assembled using Kevlar fibres as counter electrode and tested with both liquid and gel-state electrolytes. As for short devices, larger PTFE tube (diam. 1.58 mm x 3.18 mm) was used because of the thicker cathodes.

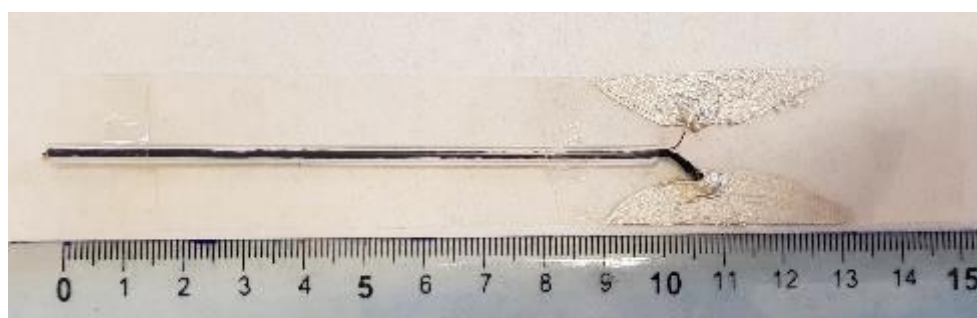


Figure 6.39. Long fibre DSSC counter electrode and 2 deposition-based photoanode.

Table 6.20 shows the relevant average photovoltaic parameters obtained from J-V measurements (Figure 6.40) for both liquid and *quasi*-solid state electrolytes.

Table 6.20. Average photovoltaic parameters (three devices for each category) for long Kevlar counter electrode/2 depositions TiO₂ photoanode-based FDSSCs.

		J_{sc} [mA/cm²]	V_{oc} [mV]	FF [%]	η [%]
liquid EL-HPE	not stressed	1.98 ± 0.30	425 ± 73	23 ± 5	0.20 ± 0.10
	stressed	0.36 ± 0.09	279 ± 35	21 ± 1	0.02 ± 0.01
gel EL-HPE	not stressed	0.600 ± 0.200	292 ± 23	22 ± 1	0.04 ± 0.01
	stressed	0.374 ± 0.051	237 ± 20	22 ± 1	0.02 ± 0.01

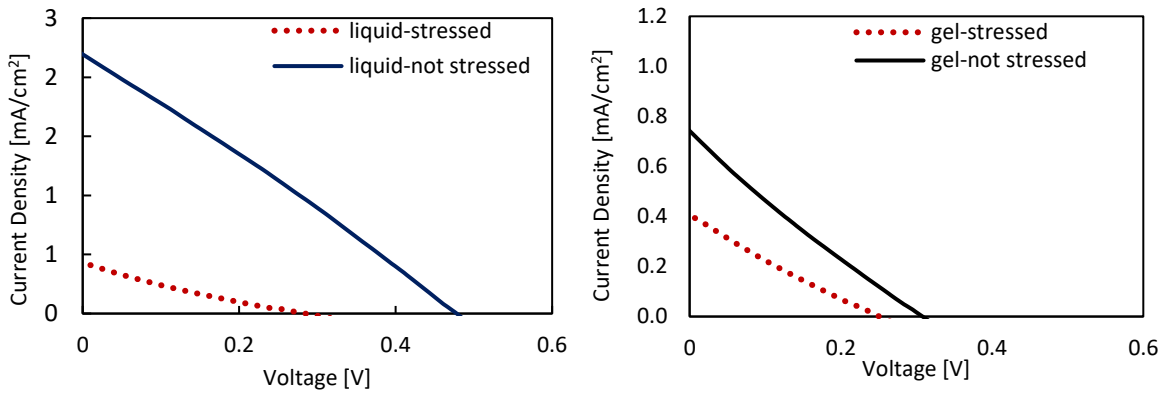


Figure 6.40. J-V curves for 2 TiO₂ depositions (dep)-Kevlar based counter electrodes long devices tested with liquid and gel state electrolyte.

Current density and open circuit values obtained for liquid electrolyte-based devices are consistent with previously tested Pt-based DSSFs: long Kevlar-based devices globally allow higher photovoltaic performances when compared with short ones. In contradiction with earlier findings however, *quasi*-solid Kevlar counter electrode-based long devices showed general worse performances in respect to the corresponding liquid-based cells. The explanation for this rather contradictory result is very likely to be attributed to the formation of void spaces between the two electrodes in response to acetone evaporation caused by the fibrous nature of the counter electrode encountered during cells filling, which were not found for short devices because of their reduced length decreases the probability of developing such flaws. Overall, this result is thus to be considered more related to the fabrication of the devices *per se*, which makes of gel electrolyte a poor choice for long Kevlar counter electrode-based fibre DSSCs. As for the low fill factor values, as previously explained the reason is related to the nature of the Kevlar fibres.

Thus, for liquid base systems, which represented the best options for long Kevlar-based devices, impedance measurements were performed (*Figure 6.41*) and the equivalent circuit reported in *Figure 6.19* was used to fit the experimental data.

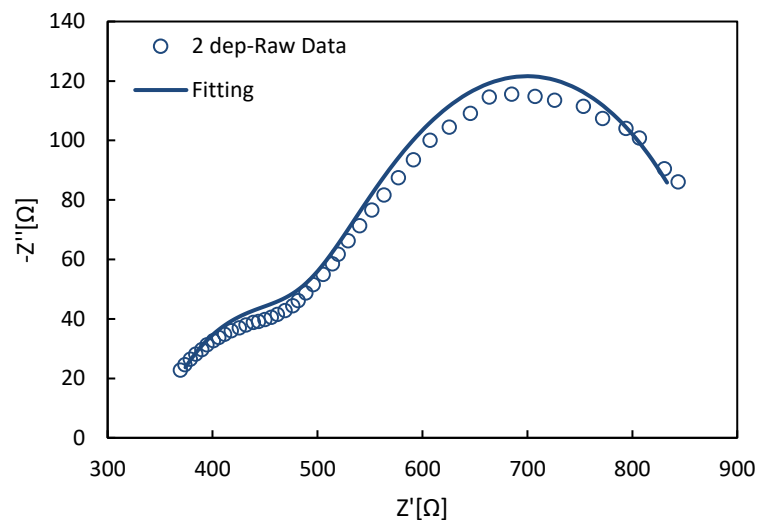


Figure 6.41. Nyquist Plot of a long fibre DSSC based on Kevlar counter electrode and liquid electrolyte.

As shown by the extrapolated values of photoanode (R_3) and counter electrode (R_1) resistivity reported in *Table 6.21*, the TiO_2 charge transfer resistance appeared lower if compared to short devices with the same number of depositions (524Ω); this confirms the photovoltaic results obtained by J-V measurements.

Table 6.21. Comparison between the resistances of short and long fibre DSSCs based on Kevlar counter-electrode.

	R1 [Ω]	R3 [Ω]
3.50 cm	238	524
10.0 cm	343	420

In contrast, the total electrical resistance determined (R_1) for long devices was higher if compared with the one attained for short devices. This may be probably attributed to the poor conductivity of the Kevlar-based photocathode, which hinders the conduction of electrons for longer distances.

6.6.2. Metal free-based photoanodes

As a last part of the project the substitution of Ti wires as photoanodes substrates with non-metallic fibres has been investigated with the aim of a future entirely metal-free electrodes-based fibre DSSCs. For this purpose, PPy-coated Kevlar fibres were employed as photoanode conductive substrates in short devices (3.5 cm) and TiO₂ coating was applied using the same procedure previously optimized on metal wires. In order to demonstrate the real applicability of natural fibers as photoanode substrate and due to the low Kevlar conductivity, 4 Titania depositions were considered. Scanning electron microscope was used to examine the morphology of the TiO₂ coating on the Kevlar fibres (*Figure 6.42*). The TiO₂ layer completely covered the wires proper of the Kevlar fibre. EDS detector confirmed the nature of the film (*Figure 6.43*).

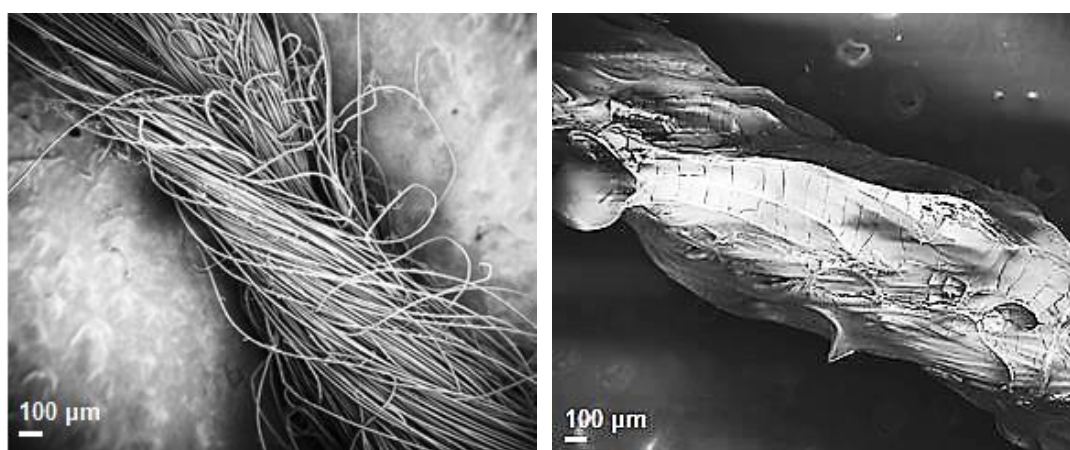


Figure 6.42. SEM images of Kevlar fibers before (left), and after (right) TiO₂ deposition.

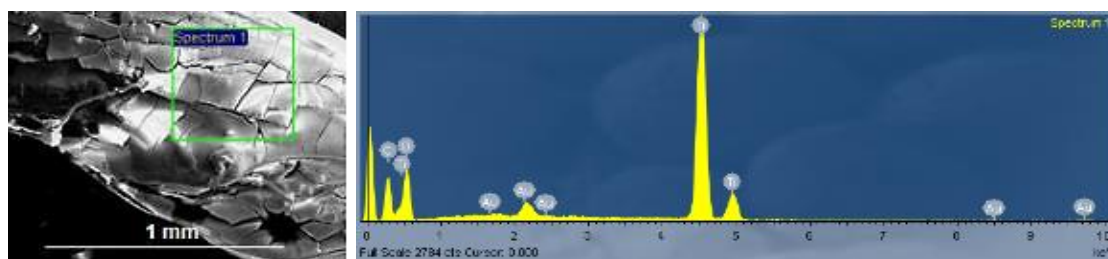


Figure.6.43. EDS analysis of the TiO₂-coated Kevlar fibre used as photoanode.

J-V measurement (*Figure 6.44*) were performed on cells assembled using Pt wire and liquid electrolyte based on I⁻/I₃⁻ as respectively counter electrode and electrolyte in order to explore the sole influence of the conductive substrate on cells performances.

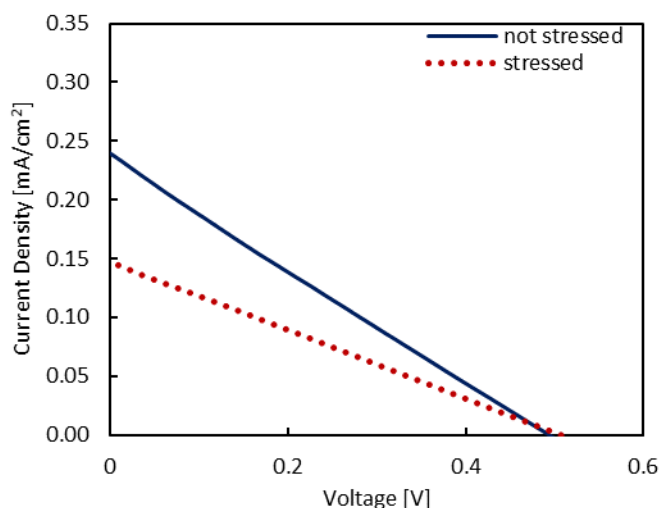


Figure 6.44. J-V curve of a fibre DSSC based on 4 depositions Kevlar based-photoanode/Pt counter electrode short device (3.5 cm) tested with liquid EL-HPE electrolyte.

The table below shows the average photovoltaic parameters obtained from the J-V curves.

Table 6.22. Average photovoltaic parameters of fibre DSSCs based on 4 deposition-Kevlar based photoanodes, Pt counter electrodes with liquid EL-HPE electrolyte.

	J_{sc} [mA/cm²]	V_{oc} [mV]	FF [%]	η [%]
not stressed	0.31 ± 0.11	503 ± 17	24 ± 1	0.04 ± 0.02
stressed	0.071 ± 0.020	502 ± 7	24 ± 1	0.02 ± 0.01

As expected, even when employing the most efficient number of deposition (*i.e.* the highest number of adsorbed dye molecules), the low electric conductivity of the PPy-coated Kevlar fibres caused very low values of current density produced with respect to the same devices employing Ti wires as photoanodes substrates ($J_{sc} 4.8 \pm 0.1 \text{ mA/cm}^2$). Open Circuit voltage values, being mainly related to the difference between the Fermi Level of electrons in the TiO_2 and the redox potential of the electrolyte, can be considered consistent with the former results. As shown by the shape of the J-V curve reported in *Figure 6.44*, fill factor values obtained are lower than the ones attained with Ti wire-based devices because of the low values of photocurrent registered as explicated by the definition of *FF* itself.

As a consequence of J_{SC} and FF values, the obtained results on power conversion efficiencies were significantly small. However, these results demonstrate the possibility to realize a fully metal-free DSSFs if the electrical conductivity of the PPy film on Kevlar fibres is improved.

References

- [1] M. Pazoki, U. B. Cappel, E. M. J. Johansson, A. Hagfeldt, and G. Boschloo, "Characterization techniques for dye-sensitized solar cells," *Energy Environ. Sci.*, 10, 3, pp. 672–709, 2017.
- [2] M. Zúkalová, M. Bousa, Z. Bastl, I. Jirka, and L. Kavan, "Electrochemical Doping of Compact TiO₂ Thin Layers," *J. Phys. Chem. C*, 118, pp. 25970–25977, 2014.
- [3] H. Li, J. Wang, Q. Chu, Z. Wang, F. Zhang, and S. Wang, "Theoretical and experimental specific capacitance of polyaniline in sulfuric acid," *J. Power Sources*, 190, pp. 578–586, 2009.
- [4] A. Dessì, M. Calamante, A. Mordini, M. Peruzzini, A. Sincropi, R. Basosi, F. Fabrizi de Biani, M. Taddei, D. Colonna, A. di Carlo, G. Reginato, L. Zani, "Thiazolo[5,4-d]thiazole-based organic sensitizers with strong visible light absorption for transparent, efficient and stable dye-sensitized solar cells," *RSC Adv.*, 5, pp. 32657–32668, 2015.
- [5] M. K. Mohsen, M. R. Fraih, N. JH, K. H. Lateef, "Spectrophotometric Study of Dyes for Dye Sensitized Solar Cell," *Journal of Global Pharmacy Technology*, 9, pp. 206–212, 2017.
- [6] A. Dessì, M. Calamante, A. Mordini, M. Peruzzini, A. Sincropi, R. Basosi, F. Fabrizi de Biani, M. Taddei, D. Colonna, A. di Carlo, G. Reginato, L. Zani, "Organic dyes with intense light absorption especially suitable for application in thin-layer dye-sensitized solar cells," *Chem. Commun.*, 50, pp. 13952–13955, 2014.
- [7] C. P. Lee, C. T. Li, and K. C. Ho, "Use of organic materials in dye-sensitized solar cells," *Mater. Today*, 20, pp. 267–283, 2017.
- [8] A. Hagfeldt, G. Boschloo, L. Sun, L. Klöö, H. Pettersson, "Dye-sensitized solar cells," *Chem. Rev.*, 110, pp. 6595–6663, 2010.
- [9] H. Park, J. Choi, J. P. Choi, and W. B. Kim, "Enhancing the electrical properties of dye-sensitized solar cells by carbon-free titanium gel via a non-hydrolytic method," *J. Photochem. Photobiol. A Chem.*, 351, pp. 139–144, 2018.

- [10] M. C. Wu, W. C. Chen, T. H. Lin, K. C. Hsiao, K. M. Lee, and C. G. Wu, "Enhanced open-circuit voltage of dye-sensitized solar cells using Bi-doped TiO₂ nanofibers as working electrode and scattering layer," *Sol. Energy*, 135, pp. 22–28, 2016.
- [11] M. Berginc, U. O. Krašovec, and M. Topič, "Evaluation of the recombination processes in DSSC by measuring the open circuit voltage over a wide illumination intensity range," *Phys. Status Solidi Appl. Mater. Sci.*, 210, pp. 1750–1757, 2013.
- [12] K. Ebrahim, "Dye Sensitized Solar Cells - Working Principles, Challenges and Opportunities," *Sol. Cells - Dye. Devices*, 2011.
- [13] T.A. Gessert, T.J. Coutts, "Requirements of Electrical Contacts to Photovoltaic Solar Cells," *Symposium B-Advance metallizations in Microelectronic*, 184, pp. 237–248, 1990.
- [14] W. J. Yin, S. Chen, J. H. Yang, X. G. Gong, Y. Yan, and S. H. Wei, "Effective band gap narrowing of anatase TiO₂ by strain along a soft crystal direction," *Appl. Phys. Lett.*, 96, 2010.
- [15] B. S. Avinash, V. S. Chaturmukka, H.S. Jayanna, C. S. Naveen, M. P. Rajeeva, B.M. Harish, S. Suresh, A. R. Lamani, "Effect of particle size on band gap and DC electrical conductivity of TiO₂ nanomaterial," *AIP Conf. Proc.*, 1728, 02426: pp.1-4, 2016.
- [16] V. Baglio, M. Girolamo, V. Antonucci, and A. S. Aricò, "Influence of TiO₂ film thickness on the electrochemical behaviour of dye-sensitized solar cells," *Int. J. Electrochem. Sci.*, 6, pp. 3375–3384, 2011.
- [17] A. Sacco, "Electrochemical impedance spectroscopy: Fundamentals and application in dye-sensitized solar cells," *Renew. Sustain. Energy Rev.*, 79, pp. 814–829, 2017.
- [18] Q. Wang, J. E. Moser, and M. Grätzel, "Electrochemical impedance spectroscopic analysis of dye-sensitized solar cells," *J. Phys. Chem. B*, 109, pp. 14945–14953, 2005.
- [19] F. Fabregat-Santiago, J. Bisquert, G. Garcia-Belmonte, G. Boschloo, and A. Hagfeldt, "Influence of electrolyte in transport and recombination in dye-

- sensitized solar cells studied by impedance spectroscopy,” *Sol. Energy Mater. Sol. Cells*, 87, pp. 117–131, 2005.
- [20] J. Wu, Z. Lan, J. Lin, M. Huang, Y. Huang, L. Fan, G. Luo, “Electrolytes in dye-sensitized solar cells,” *Chem. Rev.*, vol. 115, pp. 2136–2173, 2015.
- [21] JH Yum, E. Baranoff, F. Kessler, T. Moehl, S. Ahmad, T. Bessho, A. Marchioro, E. Ghadiri, J-E. Moser, C. Yi, M. K. Nazeeruddin, and M. Grätzel, “A cobalt complex redox shuttle for dye-sensitized solar cells with high open -circuit potentials,” *Nat. Commun.*, 3:361, pp. 1-8, 2012
- [22] H. Nusbauer, S. M. Zakeeruddin, J. E. Moser, and M. Grätzel, “An alternative efficient redox couple for the dye-sensitized solar cell system,” *Chem. - A Eur. J.*, 9, pp. 3756–3763, 2003.
- [23] X. Fu, H. Sun, S. Xie, J. Zhang, Z. Pan, M. Liao, L. Xu, Z. Li, B. Wang, H. Sun, . Peng, “A fiber-shaped solar cell showing a record power conversion efficiency of 10%,” *J. Mater. Chem. A*, 6, pp. 45–51, 2017.
- [24] Y. Fu, H. Wu, S. Ye, X. Cai, X. Yu, S. Hou, H. Kafafy, D. Zou, “Integrated power fiber for energy conversion and storage,” *Energy Environ. Sci.*, 6, pp. 805–812, 2013.
- [25] R. B. A., Ed., *Handbook of Properties of Textile and Technical Fibres*, Second Ed. Woodhead Publishing-Elsevier, 2018.
- [26] A. Varesano, L. Dall’Acqua, and C. Tonin, “A study on the electrical conductivity decay of polypyrrole coated wool textiles,” *Polym. Degrad. Stab.*, 89, pp. 125–132, 2005.
- [27] S. Hou, X. Cai, Y. Fu, X. Lv, D. Wang, H. Wu, C. Zhang, Z. Chu, D. Zou., “Transparent conductive oxide-less, flexible, and highly efficient dye-sensitized solar cells with commercialized carbon fiber as the counter electrode,” *J. Mater. Chem.*, 21, pp. 13776–13779, 2011.
- [28] P. Jha, P. Veerender, S.P. Koiry, C. Sridevi, A. K. Chauhan, K. P. Muthe, S. C. Gadkari, “Growth of aligned polypyrrole acicular nanorods and their application as Pt-free semitransparent counter electrode in dye-sensitized solar cell,” *Polym. Adv. Technol.*, 29, pp. 401–406, 2018.

- [29] S. Pan, Z. Yang, P. Chen, X. Fang, G. Guan, Z. Zhang, J. Deng, H. Peng, “Carbon nanostructured fibers as counter electrodes in wire-shaped dye-sensitized solar cells,” *J. Phys. Chem. C*, 118, pp. 16419–16425, 2014.
- [30] G. Kron, U. Rau, and J. H. Werner, “Influence of the Built-in Voltage on the Fill Factor of Dye-Sensitized Solar Cells,” *J. Phys. Chem. B.*, 107, pp. 13258–13261, 2003.
- [31] V. A. Online, B. Qi, and J. Wang, “Fill factor in organic solar cells,” *Phys. Chem. Chem. Phys.*, 15, pp. 8972–8982, 2013.
- [32] M. A. Green, “Accuracy of Analytical Expression for solar Cell Fill Factors,” *Sol. Cells*, 7, pp. 337–340, 1983.

Chapter 7. Conclusion

At present, Dye-Sensitized Solar Cells can be considered, at the moment, one of the most promising alternatives to the traditional photovoltaic technology when trying to move towards flexible and transparent portable devices. Moreover, their simple manufacturing process, their stability, and low costs of materials make of DSSCs an efficient and easily implement technology for future energy supply. In addition, considering the increasing demand of modern electronics for small, portable and wearable integrated optoelectronic devices, Fibre Dye-Sensitized Solar Cells (FDSSCs) have gained increasing interest as suitable energy provision systems for the development of the next generation of smart products namely “electronic textiles” or “e-textiles”.

In order to push the commercial exploitation of these devices, other than improve their conversion efficiency it is important to use substrates closer to the textile industry (like natural fibres) in order to integrate fibre DSSCs directly in the production process of the garment.

In this thesis several key parameters towards the optimization of FDSSCs based on the employing of TiO_2 as photoanode semiconductor material and of a fully organic sensitizers (TTZ5) as a substitution of the high cost and high toxic Ru-based organometallic compounds normally used, have been analysed.

In the first part of the work, considering the physical and chemical properties of the photoanodes and the obtained photovoltaic performances, the optimal thickness of the TiO_2 coating has been identified for short devices (3.5 cm). Commercially available liquid electrolyte based on I^-/I_3^- (EL-HPE), Pt wire counter electrode and Ti wire as photoanodes conductive material have been initially used in the fabrication of the cells to focus the attention on the role of the photoanode on the device performances. Two different numbers of dip-coated layers were thus determined as optimal, 2 and 4 (corresponding to 5 and 10 μm), and therefore used in the subsequent part of the study.

The influence of different electrolytes on photovoltaic performances was then investigated as a key component of the devices. In particular, I^-/I_3^- and $[\text{Co}(\text{bpy})_3]^{3+/2+}$ redox couples were employed leading to general best performances achieved by the commercial option (I^-/I_3^- based electrolyte). At this point, the gelation of such electrolyte was performed with the aim of obtaining quasi-solid devices particularly interesting for their higher stability (low volatility of the electrolyte), and better sealing properties,

appealing features for fibre DSSCs, and their wearable purpose. PMMA-based gelation (*in-situ* polymeric gelation) and SiO₂ nanoparticles-based gelation were performed, resulting in a non-applicability of the latter method for FDSSCs because of the geometry of the cell itself. Gel-state devices provide, in general similar efficiencies compared to the liquid system ones for both photoanodes optimum thicknesses, demonstrating the possibility of applying this rapid room-temperature procedure to the fibre geometry with satisfying results.

After that, the attention was focused on the length of the devices as a key passage to satisfy the demand of wearable working systems which can adapt to a variety of curved surfaces. A study on the transferability of the results obtained for short devices (3.5 cm) was thus carried out employing 10.0 cm length cells. The investigation demonstrates that, for longer devices, a thinner photoanode leads to better results possibly for the higher probability of having coating defects (*i.e.* more fragile photoanodes) with thicker anodes. *Quasi-solid* 10.0 cm length devices were then assembled and tested for the optimum thickness, showing comparable efficiencies with liquid-based cells in accordance with results for short fibre DSSCs.

In the last part of this thesis, a step towards more flexible devices and reduced fabrication costs was attempted. From this prospective, firstly the substitution of Pt as counter electrode, and secondly of Ti wire as photoanode conductive substrate secondly, were performed. As substitutes, PPy-coated Kevlar fibres were employed. Standard length (3.50 cm) and long devices (10.0 cm) with optimized photoanodes thickness (2 and 4 depositions) were fabricated and tested with both liquid and gel electrolytes showing how, due to the low conductivity of the cathode if compared with Pt, only with thicker photoanodes satisfying results for a possible future working device could be obtained for short cells. Regarding long devices it was found that, in accordance with what seen before, liquid-based long system attained general higher photovoltaic parameters compared to liquid-based short devices. However, in contradiction with earlier findings, quasi-solid Kevlar counter electrode-based long devices attained general worse performances with respect to the corresponding liquid-based cells probably because of issues cell-filling related to be reconducted to the fibrous nature of Kevlar which facilitate the formation of void spaces. At last, Kevlar-based photoanodes were employed on short devices using thicker TiO₂ coating because of the low conductivity of the substrate. However, because of the high resistivity of the fibre low values of efficiencies were obtained.

In conclusion, even though the performance of these systems needs to be improved to result competitive with the most efficient devices, this work has shown how DSSCs based on fully organic sensitizer can be employed in the fibre geometry with quite promising results, both in liquid system and quasi-solid short and long devices. Further work needs to be done to optimize TiO₂ structure in order to obtain hierarchical photoanodes, which could increase the charge collection ability. On the other hand, more conductive materials to substitute the metal components (conductive polymers, carbon nanotubes etc.) need to be used to obtain overall satisfying results in the field of free-metals fibre DSSCs.